# Searching for Physics Beyond the Standard Model: From Neutrinos to the Higgs Bosons

by

**Han Qin**

B.S. in Physics, Wuhan University, 2016

M.S. in Physics, University of Pittsburgh, 2017

Submitted to the Graduate Faculty of

the Dietrich School of Arts and Sciences in partial fulfillment

of the requirements for the degree of

**Doctor of Philosophy**

University of Pittsburgh

2022

UNIVERSITY OF PITTSBURGH

DIETRICH SCHOOL OF ARTS AND SCIENCES

This dissertation was presented

by

Han Qin

It was defended on

April 28, 2022

and approved by

Tao Han, Distinguished Professor, University of Pittsburgh

Ayres Freitas, Associate Professor, University of Pittsburgh

Jeremy Levy, Distinguished Professor, University of Pittsburgh

Vittorio Paolone, Professor, University of Pittsburgh

Riccardo Penco, Assistant Professor, Carnegie Mellon University

Dissertation Director: Tao Han, Distinguished Professor, University of Pittsburgh

Copyright © by Han Qin
2022

**Searching for Physics Beyond the Standard Model:**
**From Neutrinos to the Higgs Bosons**

Han Qin, PhD

University of Pittsburgh, 2022

This thesis consists of several projects of particle physics phenomenology in two major directions: (1) search for new physics effects on Higgs couplings at high energy scales; (2) realization of a UV-complete model of neutrino mass and non-standard interactions, accompanied by its phenomenological signatures at hadron colliders.

In the search of the "Beyond the Standard Model" (BSM) effects on Higgs couplings, we first explore the off-shell Higgs boson ($h$) measurement in the $pp \to h^* \to Z(\ell^+\ell^-)Z(\nu\bar{\nu})$ channel at the high-luminosity (HL) LHC. The new physics sensitivity is parametrized in terms of the Higgs boson width, dimension-6 operators in the effective field theory, and a non-local Higgs-top coupling form factor. In another project along the same direction, we explore the sensitivity to new physics for the coupling of Higgs boson and top quark ($t$) at high energy scales with the process $pp \to t\bar{t}h$ which probes the coupling in both space-like and time-like domains at a high scale, complementary to the off-shell Higgs processes in time-like domain. Both channels present strong sensitivities to the new physics scale and will be studied by the ATLAS and CMS collaborations.

In the aspect of BSM effects on neutrino physics, we study the non-standard interactions of neutrinos with light leptonic scalars ($\phi$) in a global $(B-L)$-conserved ultraviolet (UV)-complete model. The model utilizes Type-II seesaw motivated interactions with an $SU(2)_L$-triplet scalar and an additional singlet scalar. The UV-completion leads to an enriched spectrum and new observable signatures. We examine the low-energy lepton flavor violation constraints, as well as the perturbativity and unitarity constraints on model parameters. Then we lay out a search strategy for unique signatures of the model. We present the mass reach of the doubly-charged scalar at HL-LHC and future 100 TeV hadron collider, we also demonstrate that the mass of $\phi$ can be determined at about 10% accuracy at HL-LHC for the large Yukawa coupling scenario even it escapes as missing momentum from detectors.

## Table of Contents

## List of Tables

## List of Figures

## Preface

This preface is dedicated to acknowledge the numerous help I received toward my PhD degree.

First and foremost, I want to thank my advisor, Professor Tao Han, for his continuous guidance and support. He imparted his knowledge, stimulated my thinking, and most importantly, taught me the qualities of a good man and great scientist, for which I shall remain indebted to him forever. I also thank other professors in my committee Ayres Freitas, Jeremy Levy, Vittorio Paolone and Riccardo Penco, as well as other faculty and staff members in our department, for their help, advice and guidance.

I would like to thank my collaborators: Dorival Gonçalves, Tathagata Ghosh, Yongchao Zhang, Bhaskar Dutta, Bhupal Dev, Tong Li, Sze Ching Iris Leung, Roshan Mammen Abraham and Doojin Kim, for not only the helpful and constructive discussions on physics, but also the fun and joy we had together. I want to express special thanks to my senior fellow students, Xing Wang and Hongkai Liu, who gave me countless help at my beginning time in Pittsburgh.

I met my beloved fiancée, Shuyan Zhai, during my PhD journey, I would rank this as my greatest achievement above all others. Without Shuyan's unfailing support and encouragement especially during this pandemic time, I wouldn't make through this far. I cannot wait to spend the rest of my life with her.

Last but most important, I want to thank my parents for their unconditional love and endless patience, especially my mother who put off pursuing her own PhD after I was born and gave up many career opportunities so that I could get all the love and care. Being their son is simply the luckiest thing ever in my life.

## 1.0 Introduction

Over the centuries, one of the major goals of physics is to understand the most fundamental constituents of nature and their laws of interactions. With the development of quantum field theory and the discoveries benefited from modern collider technology, the Standard Model (SM) of particle physics was established to serve this purpose since 1960s, and most of its predictions have been verified in the following 30 years. Before the completion of Large Hadron Collider (LHC) at CERN, the only missing piece of the SM is the Higgs boson, which is uniquely important, responsible for the mass generation of all elementary particles. It was finally discovered in 2012 by both ATLAS and CMS collaborations [13, 14] shortly after the initial running of the LHC. The milestone discovery of the Higgs boson not only marks the tremendous success of the SM, but also leads a path towards the search of physics Beyond Standard Model (BSM).

The observed Higgs mass is around 125 GeV, which is way below the Planck scale ($\sim 10^{19}$ GeV). The huge gap between the Planck scale and electroweak scale requires unnatural fine-tuning in quantum corrections to the Higgs mass if the SM theory is valid to the Planck scale. To provide a satisfactory mechanism for the large cancellation, theories of BSM are needed to solve this hierarchy problem in a more natural way. In the absence of new particles beyond the SM, precision measurements of the Higgs properties, especially at high energy scales, may be the good approach to probe the new physics effects.

Another puzzle related to the Higgs boson is that the electroweak (EW) symmetry breaking generates the mass of other elementary particles in the SM, but it lacks an explanation of the non-zero mass of neutrinos observed in neutrino oscillation experiments. Many ideas as theoretical extensions of the SM have been proposed to explain the origin of neutrino mass. However, the underlying principle of neutrino mass generation remains unknown and the associated new physics is yet to be discovered.

In this thesis, I study the phenomenological consequences of possible BSM solutions to these puzzles. Hopefully the work would guide the experimental searches and shed light on future explorations.

## 1.1 Framework of Standard Model

The Standard Model of particle physics utilizes the non-Abelian gauged quantum field theory to describe all the fundamental constituents in nature, which are known as elementary particles, and three of the four fundamental interactions (except gravity) among these particles.

In the SM, we use fields to represent the elementary particles, each elementary particle is a quantum of corresponding quantum field. Based on the spins of elementary particles, we can classify them into elementary bosons and elementary fermions. Most elementary bosons are spin-1 gauge vector bosons, they are the force carriers of those fundamental interactions. Fermionic particles interact with each other by exchanging these gauge vector bosons. Higgs boson is the only elementary particle in the SM that has spin-0, it plays a key role in explaining the spontaneous summery breaking of the SM and generating mass of other particles through Higgs mechanism. Elementary fermions with spin-$\frac{1}{2}$ can be further categorized into quarks that carry color charges and participate in strong interaction, and leptons that only experience electroweak interaction. Quarks have three generations, each generation contains a up-type quark and down-type quark. Leptons also have three generations, each generation can be divided into charged lepton which carries one unit of electric charge $e$, and neutrino that is electric neutral thus does not experience electromagnetic force. The left-handed fields of quarks and leptons should be differentiated from their right-handed ones because the weak interaction is chiral. Table 1 and Table 2 summarize the field contents of the SM, and their quantum numbers.

The three interactions explained by the SM are strong interaction, weak interaction and electromagnetic interaction, the gauge groups associated with these interactions are

$$SU(3)_C \times SU(2)_L \times U(1)_Y \tag{1.1}$$

The $SU(3)_C$ is the gauge group of quantum chromodynamics (QCD) which describes the strong interaction, there are 8 gauge bosons $G^i_\mu$ (gluons) and a gauge coupling $g_s$ that controls the strength of strong interaction. QCD is non-chiral and acts on quarks with 3

Table 1: Bosonic contents of Standard Model

| Type | Spin | Fields | Quantum Number $SU(3)_C, SU(2)_L, U(1)_Y$ |
|---|---|---|---|
| Hypercharge Boson | 1 | $B_\mu$ | $(\mathbf{1}, \mathbf{1}, 0)$ |
| Weak Boson | 1 | $W^1_\mu, W^2_\mu, W^3_\mu$ | $(\mathbf{1}, \mathbf{3}, 0)$ |
| Gluons | 1 | $G^a_\mu$, $a = 1...8$ | $(\mathbf{8}, \mathbf{1}, 0)$ |
| Higgs | 0 | $H = \begin{pmatrix} \phi^+ \\ \phi^0 \end{pmatrix}$ | $(\mathbf{1}, \mathbf{2}, \frac{1}{2})$ |

Table 2: Fermionic contents of Standard Model

| Type | Fields | Quantum Number $SU(3)_C, SU(2)_L, U(1)_Y$ |
|---|---|---|
| Quark | $\begin{pmatrix} u_L \\ d_L \end{pmatrix}, \begin{pmatrix} c_L \\ s_L \end{pmatrix}, \begin{pmatrix} t_L \\ b_L \end{pmatrix}$ | $(\mathbf{3}, \mathbf{2}, \frac{1}{6})$ |
| | $u_R$, $c_R$, $t_R$ | $(\mathbf{3}, \mathbf{1}, \frac{2}{3})$ |
| | $d_R$, $s_R$, $b_R$ | $(\mathbf{3}, \mathbf{1}, -\frac{1}{3})$ |
| Lepton | $\begin{pmatrix} \nu_{eL} \\ e_L \end{pmatrix}, \begin{pmatrix} \nu_{\mu L} \\ \mu_L \end{pmatrix}, \begin{pmatrix} \nu_{\tau L} \\ \tau_L \end{pmatrix}$ | $(\mathbf{1}, \mathbf{2}, -\frac{1}{2})$ |
| | $e_R$, $\mu_R$, $\tau_R$ | $(\mathbf{1}, \mathbf{1}, -1)$ |

colors. Since $SU(3)_C$ group is unbroken in the SM, the gluons remain massless while quark mass is generated through the Higgs mechanism.

The electroweak interaction is unified in the SM by $SU(2)_L \times U(1)_Y$ group, $SU(2)_L$ is chiral and only acts on left-handed fermion fields. The $W^i_\mu$ and $B_\mu$ are gauge fields of

electroweak theory in unbroken phase, their coupling strengths are controlled by $g$ and $g'$. After spontaneous symmetry breaking $SU(2)_L \times U(1)_Y \to U(1)_{\rm EM}$, Higgs field developed a vacuum expectation value (vev) in its CP-even neutral component, then the gauge bosons can be projected into their mass eigenstates: $W^{\pm}$, $Z^0$ that mediate the weak force, and $\gamma^0$ that carries the electromagnetic force.

With the field contents and gauge groups of Standard Model, we can write the compact form of the SM Lagrangian as follows

$$\mathscr{L}_{\rm SM} = \mathscr{L}_{\rm gauge} + \mathscr{L}_{\rm fermion} + \mathscr{L}_{\rm Higgs} + \mathscr{L}_{\rm Yukawa}. \tag{1.2}$$

The first two include the kinetic terms of fermions and vector bosons as well as their interactions, writing them explicitly would read

$$\begin{aligned} \mathscr{L}_{\rm gauge} &= -\frac{1}{4} G^i_{\mu\nu} G^{\mu\nu i} - -\frac{1}{4} W^i_{\mu\nu} W^{\mu\nu i} - \frac{1}{4} B_{\mu\nu} B^{\mu\nu} \\ \mathscr{L}_{\rm fermion} &= \sum_{i=1}^{3} \left[ \bar{Q}^i \, i\not{D} Q^i + \bar{u}^i_R \, i\not{D} u^i_R + \bar{d}^i_R \, i\not{D} d^i_R + \bar{L}^i \, i\not{D} L^i + \bar{e}^i_R \, i\not{D} e^i_R \right] \end{aligned} \tag{1.3}$$

where the field strength tensors are defined as:

$$\begin{aligned} G^i_{\mu\nu} &= \partial_\mu G^i_\nu - \partial_\nu G^i_\mu - g_s f_{ijk} G^j_\mu G^k_\nu, \quad i,j,k = 1 \cdots 8 \\ W^i_{\mu\nu} &= \partial_\mu W^i_\nu - \partial_\nu W^i_\mu - g \, \epsilon_{ijk} W^j_\mu W^k_\nu, \quad i,j,k = 1 \cdots 3 \\ B_{\mu\nu} &= \partial_\mu B_\nu - \partial_\nu B_\mu \end{aligned} \tag{1.4}$$

with $L$, $Q$ denote the doublets of leptons and quark, $u_R, d_R, e_R$ denote right-handed up-type quarks, down-type quarks and charged leptons respectively.

Higgs potential is included in the third term and it triggers the spontaneous symmetry breaking. Last term describes the Yukawa interaction between the Higgs and SM fermions, it is responsible for generating fermion mass after Higgs gets the vev. $\mathscr{L}_{\rm Higgs}$ and $\mathscr{L}_{\rm Yukawa}$ will be revisited in details in next sections.

## 1.2 Higgs Mechanism and Hierarchy Problem

The Higgs mechanism[15, 16, 17] is one of the most important ingredients of the SM, it gives rise to particle mass through the spontaneous symmetry breaking (SSB) of $SU(2)_L \times U(1)_Y$. To understand how it works, we need to take a look at the Higgs term of the SM Lagrangian:

$$\mathscr{L}_{\text{Higgs}} = (D_\mu H)^\dagger D^\mu H - V(H) \tag{1.5}$$

$D_\mu H$ is the covariant derivative of Higgs field, with $\tau^a = \frac{\sigma^a}{2}$ as the canonical generator of $SU(2)$ group, it reads

$$D_\mu H = \partial_\mu H - i\, g\, \tau^a W_\mu^a H - \frac{1}{2} i\, g'\, B_\mu H \tag{1.6}$$

$V(H)$ is the Higgs potential that can be expressed as

$$V(H) = \mu^2 |H|^2 + \frac{1}{4}\lambda |H|^4 \tag{1.7}$$

When the quadratic coefficient $\mu^2 > 0$, the potential minimizes at $\langle H \rangle = 0$, the gauge group of the SM remains unbroken. However, when the coefficient $\mu^2 < 0$, there are two extreme points of Higgs potential: $\langle H \rangle = 0$ or $\langle H \rangle = \sqrt{-2\mu^2/\lambda}$. The symmetric solution $\langle H \rangle = 0$ is unstable thus Higgs potential must minimize at $\langle H \rangle = \sqrt{-2\mu^2/\lambda}$, making it break the $SU(2)_L \times U(1)_Y$ symmetry.

By defining the vacuum expectation value (vev) of Higgs field as $\frac{v^2}{2} \equiv \frac{-2\mu^2}{\lambda}$, we can rewrite the Higgs field around the vev:

$$H = \exp\left(2i\,\frac{\pi^a \tau^a}{v}\right) \begin{pmatrix} 0 \\ \frac{v+h}{\sqrt{2}} \end{pmatrix} \tag{1.8}$$

where $\pi^a$ are the Goldstone bosons which will become the longitudinal component of massive weak bosons, they can be set to zero $\pi^a = 0$ under unitary gauge. $h$ is the fluctuation along the radial direction, it acquires a mass term $m_h^2 = \frac{\lambda v^2}{2}$ once we expand the Higgs potential around vev, this is the Higgs boson observed in 2012. The newest measurement of Higgs mass yields $m_h = 125.25 \pm 0.17\,\text{GeV}$ [3].

By plugging the vev in the kinetic term of Higgs Lagrangian, we can get that:

$$|D_\mu H|^2 = g^2 \frac{v^2}{8} \left[ \left(W_\mu^1\right)^2 + \left(W_\mu^2\right)^2 + \left( \frac{g'}{g} B_\mu - W_\mu^3 \right)^2 \right] + h \text{ terms} \tag{1.9}$$

Define $\tan\theta_w = \frac{g'}{g}$ where $\theta_w$ is widely known as Weinberg angle, we can rotate the $B_\mu$ and $W_\mu^3$ to their mass eigenstates:

$$\begin{aligned} Z_\mu &= \cos\theta_w W_\mu^3 - \sin\theta_w B_\mu \\ A_\mu &= \sin\theta_w W_\mu^3 + \cos\theta_w B_\mu \end{aligned} \tag{1.10}$$

Also we can rewrite the $W_\mu^1$ and $W_\mu^2$ as

$$W_\mu^\pm = \frac{W_\mu^1 \mp i\, W_\mu^2}{\sqrt{2}} \tag{1.11}$$

With Eq.(1.10) and (1.11), the quadratic terms in Eq.(1.9) can be expressed as:

$$\mathscr{L}_{\text{SM}} \supset \frac{g^2 v^2}{4} W_\mu^+ W^{-\mu} + \frac{1}{2} \frac{(g^2 + g'^2) v^2}{4} Z_\mu Z^\mu \tag{1.12}$$

The $W^\pm$ is the charged W bosons which were discovered in 1983 [18, 19], and the $Z_\mu$ is the neutral Z boson which was also discovered in 1983[20, 21] a few months later than W discovery. We can read their mass from Eq.(1.12) that $m_W = \frac{g\,v}{2}$ and $m_Z = \frac{v}{2}\sqrt{g^2 + g'^2} = \frac{m_W}{\cos\theta_w}$. The newest measurement of their mass from PDG summary table yields that $m_W = 80.379 \pm 0.012\,\text{GeV}$ and $m_Z = 91.1876 \pm 0.0021\,\text{GeV}$. The $A_\mu$ has no quadratic term in the SM Lagrangian, it remains massless so the its associated gauge group $U(1)_{\text{EM}}$ is still symmetric after SSB. It turns out $A_\mu$ is the photon that mediates the electromagnetic force, and the coupling strength of electromagnetic interaction is also set by Weinberg angle:

$$e = g\,\sin\theta_w = g'\,\cos\theta_w \tag{1.13}$$

To understand the mass generation of the SM fermions, we need to take a look at the Yukawa interaction term. In the SM, this term is written as

$$\mathscr{L}_{\text{Yukawa}} = -Y_{ij}^l\, \bar{L}^i H e_R^j - Y_{ij}^d\, \bar{Q}^i H d_R^j - Y_{ij}^u\, \bar{Q}^i \tilde{H} u_R^j + h.c. \tag{1.14}$$

where $\tilde{H} = i\sigma^2 H$, $L$ and $Q$ are doublets of leptons and quark, $i, j = (1, 2, 3)$ refers to the flavor number. After the Higgs field gets the vev, the Eq.(1.14) will have a mass term

$$\mathscr{L}_{\text{mass}} = -\frac{v}{\sqrt{2}} Y^l_{ij} \bar{e}^i_L e^j_R - -\frac{v}{\sqrt{2}} Y^d_{ij} \bar{d}^i_L d^j_R - \frac{v}{\sqrt{2}} Y^u_{ij} \bar{u}^i_L u^j_R + h.c. \tag{1.15}$$

Generally, $Y_{ij}$ are all $3 \times 3$ matrices, but we can always rotate the flavor basis to mass basis by transforming

$$u^i_{L/R} = U^u_{L/R} \begin{pmatrix} u_{L/R} \\ c_{L/R} \\ t_{L/R} \end{pmatrix}, \; d^i_{L/R} = U^d_{L/R} \begin{pmatrix} d_{L/R} \\ s_{L/R} \\ b_{L/R} \end{pmatrix}, \; e^i_{L/R} = U^l_{L/R} \begin{pmatrix} e_{L/R} \\ \mu_{L/R} \\ \tau_{L/R} \end{pmatrix} \tag{1.16}$$

and thus diagonalize all the $Y_{ij}$ matrices. Then all fermion mass is solely determined by its Yukawa coupling $m_f = \frac{y_f v}{\sqrt{2}}$, where $y_f$ are the eigenvalues of $Y_{ij}$ matrices. Such diagonalization does not influence neutral current interactions (i.e. interactions with Z boson or photon) since they are already diagonal in flavor. However, the charged current interactions involving W boson will be modified because they change the fermion flavor. For quarks in mass basis, such interaction becomes

$$\mathscr{L}_{C.C.} \supset -i\frac{g}{\sqrt{2}} \left[ W^+_\mu \bar{u}^i_L \gamma^\mu V^{ij} d^j_L + W^-_\mu \bar{d}^i_L \gamma^\mu (V^\dagger)^{ij} u^j_L \right] \tag{1.17}$$

where $V = (U^u_L)^\dagger U^d_L$ is known as CKM matrix, it implies quark mixing among the generations in charged weak interaction.

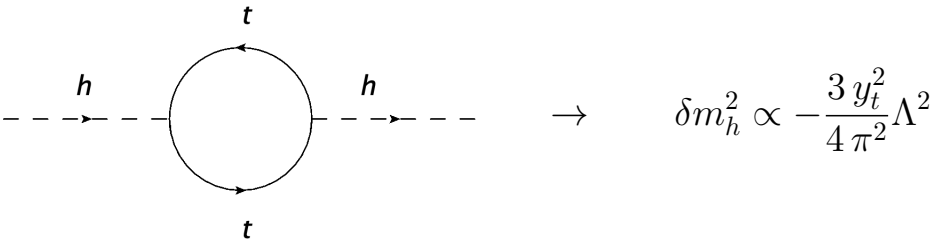


$$\rightarrow \qquad \delta m_h^2 \propto -\frac{3\, y_t^2}{4\, \pi^2} \Lambda^2$$

Figure 1: Top loop correction to Higgs mass

Nowadays the masses of heavy quarks ($c$, $b$, $t$), charged leptons ($e$, $\mu$, $\tau$) and Higgs boson have been measured to great precision, the SM seems working fine. However, there is a big

concern related to the measured Higgs mass $m_h \approx 125\,\text{GeV}$. If we calculate the one loop correction to $m_h$ by top quark loop whose contribution is largest in the SM, shown in Fig.1, we find that the correction $\delta m_h$ is proportional to the square of cut-off scale $\Lambda$. Assume that the SM is only valid up to a certain scale, this $\Lambda$ could be regarded as the next new physics scale. If the $\Lambda$ is around Planck scale $\sim 10^{19}$ GeV, there will be a huge hierarchy between the new physics scale and Electroweak scale, and it's unnatural to separate these two scales while keep the Electroweak scale stable at current value.

Many BSM theories have been come up with to solve the issue. For example, supersymmetric models lift hierarchy problem by introducing new symmetry in addition to those in the SM, so the quadratic divergence could be eliminated by super partners of the SM particles due to the supersymmetry, or the composite Higgs models evade the hierarchy problem by postulating Higgs boson is a condensed bound state rather than an elementary particle, thus the new physics scale could be lowered to $\mathcal{O}(\text{TeV})$. All these theories will have phenomenological consequence on Higgs couplings with other SM particles. The deviations of Higgs coupling from the SM values could be parameterized with an Effective Field Theory (EFT) integrating out the BSM heavy states or empirical formula, and LHC is the best place to search for such deviation. The Chapter 2 and 3 study the Higgs couplings in different channels along this direction to explore the hints of possible BSM physics.

### 1.3 Neutrino Oscillation and BSM Physics Including Neutrino

In the field contents of Standard Model, there is no right-handed neutrino, thus neutrinos stay massless even after the spontaneous symmetry breaking as shown in Eq.(1.15). Unlike the massless photon whose masslessness is protected by gauge symmetry, massless neutrino is only accidental in the SM. Over the decades, persuasive experimental evidence from the observation of neutrino oscillation has shown that neutrinos have a very tiny but non-zero mass contrary to the SM predictions.

It has been noticed back in 1960s that the flux of electron neutrino coming from the sun was significantly smaller than that predicted by standard solar model. Scientists also

noticed that the ratio of flux of muon neutrino to electron neutrino produced by cosmic rays was smaller than predicted value. These early indications drove the experimental searches of neutrino oscillation. Finally the incontrovertible data from Super-Kamiokande[22] and Sudbury Neutrino Observatory[23] confirmed that neutrino could change its flavor during its propagation. The compelling evidence of neutrino oscillation indicates that neutrinos are massive and lepton flavors are mixed just like quark mixing. This is also the first evidence that the SM of particle physics is incomplete, and BSM physics is required to explain the neutrino mass.

In the SM, the neutrino $\nu_e$, $\nu_\mu$, $\nu_\tau$ are defined to be the flavor eigenstates, they accord with three charged leptons $e$, $\mu$, $\tau$ in their production processes via the weak charged current interactions. We need to introduce three mass eigenstates $\nu_1$, $\nu_2$, $\nu_3$ with eigenvalues $m_1$, $m_2$, $m_3$ to explain the phenomenon of neutrino oscillation. Since flavor eigenstates do not align with mass eigenstates, their mixing could be described by a $3 \times 3$ unitary matrix which is known as PMNS matrix:

$$\begin{pmatrix} \nu_e \\ \nu_\mu \\ \nu_\tau \end{pmatrix} = \begin{pmatrix} U_{e1} & U_{e2} & U_{e3} \\ U_{\mu 1} & U_{\mu 2} & U_{\mu 3} \\ U_{\tau 1} & U_{\tau 2} & U_{\tau 3} \end{pmatrix} \begin{pmatrix} \nu_1 \\ \nu_2 \\ \nu_3 \end{pmatrix} \tag{1.18}$$

The PMNS matrix is most commonly parameterized by three mixing angles $\theta_{12}$, $\theta_{23}$, $\theta_{13}$ and a single phase angle called $\delta_{CP}$ related to CP violation. Most recent measurements show that neutrino mass is very small $m_i < 1.1\,\mathrm{eV}$ according to the newest review by Particle Data Group (PDG) [3], and the best fitted values of PMNS matrix parameters could be also found there [3].

If a neutrino with certain flavor $\alpha$ and energy $E$ is produced as the source, its flavor state could be written as a superposition of mass states according to PMNS matrix:

$$\nu_\alpha(0) = \sum_{i=1}^{3} U_{\alpha i}\, \nu_i(0) \tag{1.19}$$

After the neutrino propagating a length $L$ from the source, each mass state could be expressed by solving the equation of motion at the leading order in $m_i^2$

$$\nu_\alpha(L) = \sum_{i=1}^{3} U_{\alpha i} \exp\left[-i\,\frac{m_i^2}{2\,E}\,L\right] \nu_i(0) \tag{1.20}$$

Thus there exist a probability that we could observe another flavor $\beta$ from this neutrino, and the probability is:

$$P(\nu_\alpha \to \nu_\beta) = |\langle \nu_\beta | \nu_\alpha(L) \rangle|^2 = \sum_{i=1}^{3}\sum_{j=1}^{3} U_{\alpha i} U_{\beta j} U_{\alpha j}^* U_{\beta i}^* \exp\left[-i\,\frac{\Delta m_{ij}^2}{2\,E}\,L\right] \tag{1.21}$$

where $\Delta m_{ij}^2 = m_i^2 - m_j^2$.

The origin of neutrino mass remains mysterious, the simplest way to generate neutrino mass is to add the right-handed neutrinos and include the Dirac mass term of neutrino through Yukawa interaction

$$\mathscr{L}_{\nu-\text{Yukawa}} = -Y_\nu\, \bar{L}\tilde{H}\nu_R + h.c. \tag{1.22}$$

then the neutrino mass is simply $m_\nu = y_\nu v/\sqrt{2}$, where $v \approx 246$ GeV is the Higgs vacuum expectation value. A new question, however, will arise if we choose this simplest approach to get the correct neutrino mass: why is neutrino Yukawa coupling $y_\nu$ only $10^{-6}$ of the smallest Yukawa coupling $y_e$ in the SM? Seesaw models have been proposed since then to generate the tiny neutrino mass in a more natural way. The general idea of seesaw models is to introduce new degree of freedom to the SM with a seesaw scale $M$ where $M \gg v$. The physical mass of neutrino $m_\nu \propto v^2/M$, consequently neutrino mass is suppressed by the seesaw scale and naturally small.

The existence of neutrino mass is a clear sign for new physics beyond the SM, neutrino non-standard interactions (NSIs) were introduced to account for BSM effects using a general EFT description. Among numerous NSIs, there is one term that draws increasing attention recently:

$$\mathscr{L}_{\text{NSIs}} \supset G_{\text{eff}}\,(\bar{\nu}\nu)(\bar{\nu}\nu) \tag{1.23}$$

because the measured Hubble parameter $H_0$ from CMB measurement is lower than what we got from supernovae measurement [24, 25, 26, 27, 28], such discrepancy has grown to $\sim 4\sigma$. Scientists start exploring the non-standard four neutrino self-interaction, if $G_{\text{eff}} \gg G_{\text{fermi}}$, the neutrinos still scatter with each other after weak decoupling from electromagnetic plasma,

preventing neutrinos from free streaming. As a consequence, the temperature of neutrinos would evolve differently, causing the effective number of degrees of freedom $g^*$ or effective number of neutrinos $N_{\text{eff}}$ higher than what the SM predicts in early universe. The Hubble parameter is proportional to the square root of energy density, which is proportional to $g^*$. A higher $g^*$ will lead to a higher $H_0$, so the NSI in Eq.(1.23) provides a possibility to relax the current Hubble tension.

Neutrino NSIs are typically expressed in EFT like Eq.(1.23), it means the underlying UV complete picture is usually ignored. In Chapter 4, a ultraviolet(UV)-complete model which achieves a four-neutrino self interaction is presented, our model is motivated by the famous Type-II Seesaw model, and additionally introduces a new complex scalar carrying lepton number to mediate the neutrino self interaction, thus the new complex scalar is dubbed as "leptonic scalar". Due to the enlarged particle contents, our model has rich phenomenology at LHC, and several most intriguing channels are studied in details in that Chapter.

## 2.0 Off-shell Higgs Couplings in $H^* \to ZZ \to \ell\ell\nu\nu$

After the Higgs boson discovery at the Large Hadron Collider (LHC) [15, 29, 30, 31, 32], the study of the Higgs properties has been one of the top priorities in searching for new physics beyond the Standard Model (BSM). Indeed, the Higgs boson is a unique class in the SM particle spectrum and is most mysterious in many aspects. The puzzles associated with the Higgs boson include the mass hierarchy between the unprotected electroweak (EW) scale ($v$) and the Planck scale ($M_{PL}$), the neutrino mass generation, the possible connection to dark matter, the nature of the electroweak phase transition in the early universe, to name a few. Precision studies of the Higgs boson properties can be sensitive to new physics at a higher scale. Parametrically, new physics at a scale $\Lambda$ may result in the effects of the order $v^2/\Lambda^2$.

So far, the measurements at the LHC based on the Higgs signal strength are in full agreement with the SM predictions. However, these measurements mostly focus on the on-shell Higgs boson production, exploring the Higgs properties at low energy scales of the order $v$. It has been argued that if we explore the Higgs physics at a higher scale $Q$, the sensitivity can be enhanced as $Q^2/\Lambda^2$. A particularly interesting option is to examine the Higgs sector across different energy scales, using the sizable off-shell Higgs boson rates at the LHC [33, 34, 35, 36, 37]. While the off-shell Higgs new physics sensitivity is typically derived at the LHC with the $H^* \to ZZ \to 4\ell$ channel [38, 39, 40, 41, 42, 43, 44, 45], we demonstrate in this work that the extension to the channel $ZZ \to \ell\ell\nu\nu$ can significantly contribute to the potential discoveries. This channel provides two key ingredients to probe the high energy regime with enough statistics despite of the presence of two missing neutrinos in the final state. First, it displays a larger event rate by a factor of six than the four charged lepton channel. Second, the transverse mass for the $ZZ$ system sets the physical scale $Q^2$ and results in a precise phenomenological probe to the underlying physics.

In this chapter, we extend the existing studies and carry out comprehensive analyses for an off-shell channel in the Higgs decay

$$pp \to H^* \to ZZ \to \ell^+\ell^-\ \nu\bar{\nu}, \tag{2.1}$$

where $\ell = e, \mu$ and $\nu = \nu_e, \nu_\mu, \nu_\tau$. Because of the rather clean decay modes, we focus on the leading production channel of the Higgs boson via the gluon fusion. First, we phenomenologically explore a theoretical scenario with additional unobserved Higgs decay channels leading to an increase in the Higgs boson width, $\Gamma_H/\Gamma_H^{SM} > 1$. The distinctive dependence for the on-shell and off-shell cross-sections with the Higgs boson width foster the conditions for a precise measurement for this key ingredient of the Higgs sector. We adopt the Machine-learning techniques in the form of Boosted Decision Tree (BDT) to enhance the signal sensitivity. This analysis sets the stage for our followup explorations. Second, we study the effective field theory framework, taking advantage of the characteristic energy-dependence from some of the operators. Finally, we address a more general hypothesis that features a non-local momentum-dependent Higgs-top interaction [45], namely, a form factor, that generically represents the composite substructure. Overall, the purpose of this chapter is to highlight the complementarity across a multitude of frameworks [41, 40, 46, 42, 43, 44, 45] via the promising process at the LHC $H^* \to Z(\ell\ell)Z(\nu\nu)$, from models that predict invisible Higgs decays, passing by the effective field theory, and a non-local form-factor scenario. Our results demonstrate significant sensitivities at the High-Luminosity LHC (HL-LHC) to the new physics scenarios considered here beyond the existing literature.

The rest of the chapter is organized as follows. In Sec. 2.1, we derive the Higgs width limit at HL-LHC. Next, in Sec. 2.2, we study the new physics sensitivity within effective field theory framework. In Sec. 2.3, we scrutinize the effects of a non-local Higgs-top form-factor. Finally, we present a summary table in Table.3 to compare our reach of new physics scale with other channel and literature, and conclude our study in Chaper 5.

## 2.1 Higgs Boson Width

The combination of on-shell and off-shell Higgs boson rates addresses one of the major shortcomings of the LHC, namely the Higgs boson width measurement [33, 34]. This method

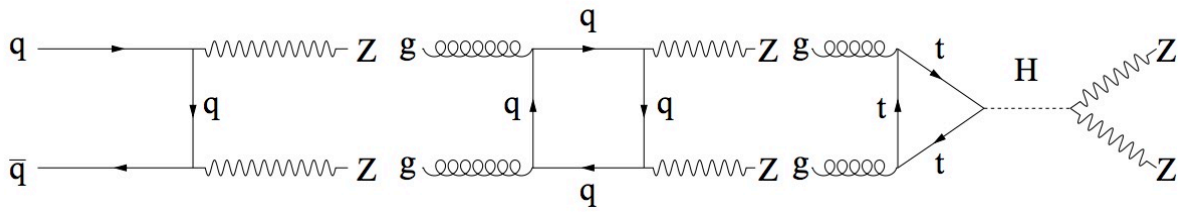


Figure 2: Representative Feynman diagrams for the DY $q\bar{q} \to ZZ$ (left), GF $gg \to ZZ$ continuum (center), and $s$-channel Higgs signal $gg \to H^* \to ZZ$ (right).

breaks the degeneracy present on the on-shell Higgs coupling studies

$$\sigma^{\text{on-shell}}_{i\to H\to f} \propto \frac{g_i^2(m_H) g_f^2(m_H)}{\Gamma_H}\,, \tag{2.2}$$

where the total on-shell rate can be kept constant under the transformation $g_{i,f}(m_H) \to \xi g_{i,f}(m_H)$ with $\Gamma_H \to \xi^4 \Gamma_H$. The off-shell Higgs rate, due to a sub-leading dependence on the Higgs boson width $\Gamma_H$

$$\sigma^{\text{off-shell}}_{i\to H^*\to f} \propto g_i^2(\sqrt{\hat{s}}) g_f^2(\sqrt{\hat{s}})\,, \tag{2.3}$$

breaks this degeneracy, where $\sqrt{\hat{s}}$ is the partonic c.m. energy that characterizes the scale of the off-shell Higgs. In particular, if the new physics effects result in the same coupling modifiers at both kinematical regimes [41, 40, 42, 43], the relative measurement of the on-shell and off-shell signal strengths can uncover the Higgs boson width, $\mu_{\text{off-shell}}/\mu_{\text{on-shell}} = \Gamma_H/\Gamma_H^{SM}$.

In this section, we derive a projection for the Higgs boson width measurement at the $\sqrt{s} = 14$ TeV high-luminosity LHC, exploring the $ZZ \to 2\ell 2\nu$ final state. We consider the signal channel as in Eq. (2.1). The signal is characterized by two same-flavor opposite sign leptons, $\ell = e$ or $\mu$, which reconstruct a $Z$ boson and recoil against a large missing transverse momentum from $Z \to \nu\bar{\nu}$. The major backgrounds for this search are the Drell-Yan (DY) processes $q\bar{q} \to ZZ, ZW$ and gluon fusion (GF) $gg \to ZZ$ process, see Fig. 2 for a sample of the Feynman diagrams. While the Drell-Yan component displays the largest rate, the gluon fusion box diagrams interfere with the Higgs signal, resulting in important contributions mostly at the off-shell Higgs regime [33].

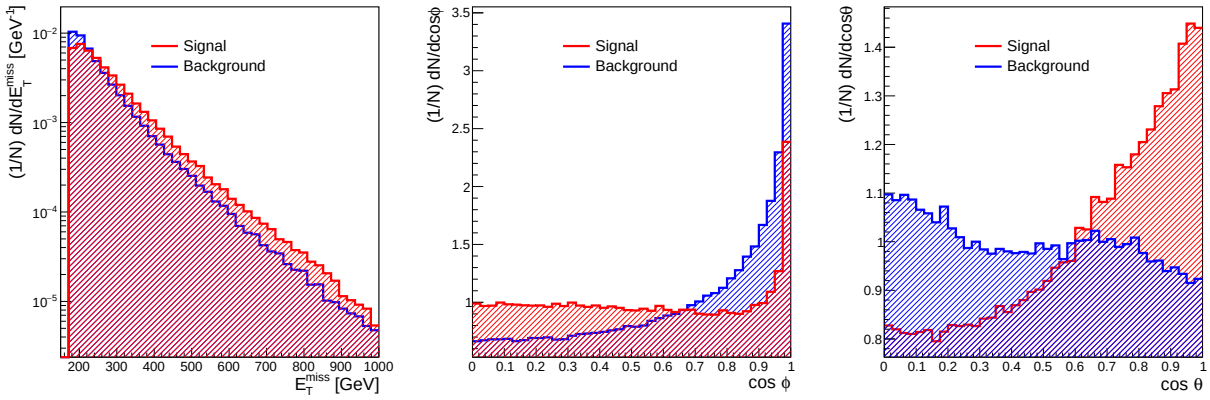


Figure 3: Normalized distributions for the missing transverse momentum $E_T^{\rm miss}$ (left panel), azimuthal $\phi$ (central panel) and polar $\theta$ angles (right panel) of the charged lepton $\ell^-$ in the $Z$ boson rest frame.

In our calculations, the signal and background samples are generated with MadGraph5 aMC@NLO [47, 48]. The Drell-Yan background is generated at the NLO with the MC@NLO algorithm [49]. Higher order QCD effects to the loop-induced gluon fusion component are included via a universal $K$-factor [35, 50]. Spin correlation effects for the $Z$ and $W$ bosons decays are obtained in our simulations with the MadSpin package [51]. The renormalization and factorization scales are set by the invariant mass of the gauge boson pair $Q = m_{VV}/2$, using the PDF set nn23nlo [52]. Hadronization and underlying event effects are simulated with Pythia8 [53], and detector effects are accounted for with the Delphes3 package [54].

We start our analysis with some basic lepton selections. We require two same-flavor and opposite sign leptons with $|\eta_\ell| < 2.5$ and $p_{T\ell} > 10$ GeV in the invariant mass window 76 GeV $< m_{\ell\ell} <$ 106 GeV. To suppress the SM backgrounds, it is required large missing energy selection $E_T^{\rm miss} > 175$ GeV and a minimum transverse mass for the $ZZ$ system $m_T^{ZZ} > 250$ GeV, defined as

$$m_T^{ZZ} = \sqrt{\left(\sqrt{m_Z^2 + p_{T(\ell\ell)}^2} + \sqrt{m_Z^2 + (E_T^{\rm miss})^2}\right)^2 - \left|\overrightarrow{p}_{TZ} + \overrightarrow{E}_T^{\rm miss}\right|^2}\,. \tag{2.4}$$

The consistency of our event simulation and analysis setup is confirmed through a cross-

check with the ATLAS study in Ref. [36].

To further control the large Drell-Yan background, a Boosted Decision Tree (BDT) is implemented via the Toolkit for Multivariate Data Analysis with ROOT (TMVA) [55]. The BDT is trained to distinguish the full background events from the $s$-channel Higgs production. The variables used in the BDT are missing transverse energy, the momenta and rapidity for the leading and sub-leading leptons $(p_T^{\ell 1}, \eta^{\ell 1}, p_T^{\ell 2}, \eta^{\ell 2})$, the leading jet $(p_T^{j1}, \eta^{j1})$, the separation between the two charged leptons $\Delta R_{\ell\ell}$, the azimuthal angle difference between the di-lepton system and the missing transverse energy $\Delta\phi(\vec{p}_T^{\,\ell\ell}, \vec{E}_T^{\rm miss})$, and the scalar sum of jets and lepton transverse momenta $H_T$. Finally, we also include the polar $\theta$ and azimuthal $\phi$ angles of the charged lepton $\ell^-$ in the $Z$ rest frame [56, 57]. We choose the coordinate system for the $Z$ rest frame following Collins and Soper (Collins-Soper frame) [58]. The signal and background distributions for these observables are illustrated in Fig. 3. We observe significant differences between the $s$-channel signal and background in the $(\theta, \phi)$ angle distributions. These kinematic features arise from the different $Z$ boson polarizations for the signal and background components at the large di-boson invariant mass $m_T^{ZZ}$ [42, 59]. Whereas the $s$-channel Higgs tends to have $Z_L$ dominance, the DY background is mostly $Z_T$ dominated.

Figure 4: BDT distribution for the $s$-channel Higgs signal (red) and background (blue).

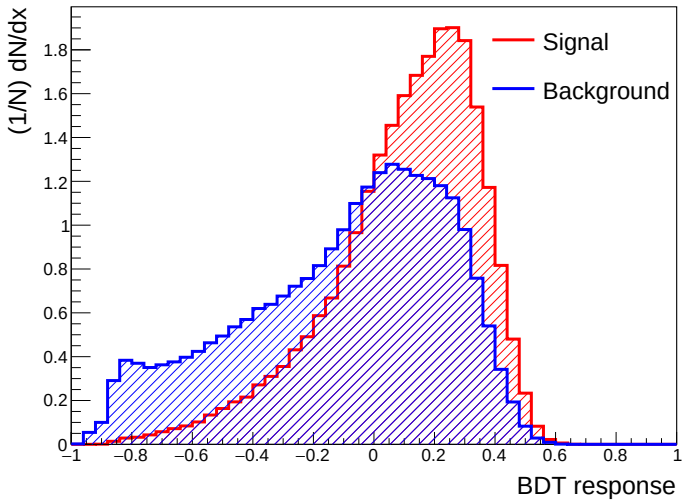


We would like to illustrate the power of the implemented BDT analysis to separate the $s$-channel Higgs from the background contributions in Fig. 4. The BDT discriminator

is defined in the range $[-1, 1]$. The events with discriminant close to $-1$ are classified as background-like and those close to 1 are signal-like. The optimal BDT score selection has been performed with TMVA. To estimate the effectiveness of the BDT treatment, we note that one can reach $S/\sqrt{S+B} = 5$ at an integrated luminosity of 273 fb$^{-1}$ with signal efficiency 88% and background rejection of 34%, by requiring $\text{BDT}_{\text{response}} > -0.26$. Now that we have tamed the dominant backgrounds $q\bar{q} \to ZZ, ZW$, we move on to the new physics sensitivity study.

To maximize the sensitivity of the Higgs width measurement, we explore the most sensitive variable, $m_T^{ZZ}$ distribution, and perform a binned log-likelihood ratio analysis. In Fig. 5, we display the 95% CL on the Higgs width $\Gamma_H/\Gamma_H^{SM}$ as a function of the $\sqrt{s} = 14$ TeV LHC luminosity. To infer the relevance of the multivariate analysis, that particularly explore the observables $(E_T^{\text{miss}}, \theta, \phi)$ depicted in Fig. 3, we display the results in two analysis scenarios: in blue we show the cut-based analysis and in red the results accounting for the BDT-based framework. The significant sensitivity enhancement due to the BDT highlights the importance of accounting for the full kinematic dependence, including the $Z$-boson spin correlation effects. Whereas the Higgs width can be constrained to $\Gamma_H/\Gamma_H^{SM} < 1.35$ at 95% CL level following the cut-based analysis, $\Gamma_H/\Gamma_H^{SM} < 1.31$ in the BDT-based study assuming $\mathcal{L} = 3$ ab$^{-1}$ of data. Hence, the BDT limits result in an improvement of $\mathcal{O}(5\%)$ on the final Higgs width sensitivity. These results are competitive to the HL-LHC estimates for the four charged lepton final state derived by ATLAS and CMS, where the respective limits are $\Gamma_H/\Gamma_H^{SM} < \mathcal{O}(1.3)$ and $\mathcal{O}(1.5)$ at 68% CL [1, 2].

### 2.2 Effective Field Theory

The Effective Field Theory (EFT) provides a consistent framework to parametrize beyond the SM effects in the presence of a mass gap between the SM and new physics states. In this context, the new physics states can be integrated out and parametrized in terms of higher dimension operators [60]. In this section we parametrize the new physics effects in terms of the EFT framework [61, 62]. Instead of performing a global coupling fit, we will focus on

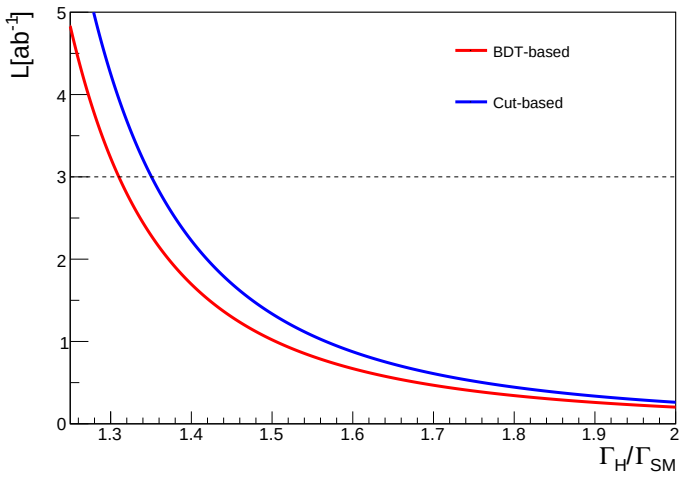


Figure 5: 95% CL bound on the Higgs width $\Gamma_H/\Gamma_H^{SM}$ as a function of the $\sqrt{s} = 14$ TeV LHC luminosity. We display the results for the cut-based study (blue) and BDT-based analysis (red).

a relevant subset of higher dimension operators that affect the Higgs production via gluon fusion. This will shed light on the new physics sensitivity for the off-shell $pp \to H^* \to Z(\ell\ell)Z(\nu\nu)$ channel. Our effective Lagrangian can be written as

$$\mathscr{L} \supset c_g \frac{\alpha_s}{12\pi v^2} |\mathcal{H}|^2 G_{\mu\nu} G^{\mu\nu} + c_t \frac{y_t}{v^2} |\mathcal{H}|^2 \bar{Q}_L \tilde{\mathcal{H}} t_R + \text{h.c.} \ , \tag{2.5}$$

where $\mathcal{H}$ is the SM Higgs doublet and $v = 246$ GeV is the vacuum expectation value of the SM Higgs field. The couplings are normalized in such a way for future convenience. If we wish to make connection with the new physics scale $\Lambda$, we would have the scaling as $c_g, c_t \sim v^2/\Lambda^2$. After electroweak symmetry breaking, Eq. (2.5) renders into the following interaction terms with a single Higgs boson

$$\mathscr{L} \supset \kappa_g \frac{\alpha_s}{12\pi v} H G_{\mu\nu} G^{\mu\nu} - \kappa_t \frac{m_t}{v} H \left( \bar{t}_R t_L + \text{h.c.} \right) \ , \tag{2.6}$$

where the coupling modifiers $\kappa_{g,t}$ and the Wilson coefficients $c_{g,t}$ are related by $\kappa_g = c_g$ and $\kappa_t = 1 - \text{Re}(c_t)$. We depict in Fig. 6 the $gg \to ZZ$ Feynman diagrams that account for these new physics effects.

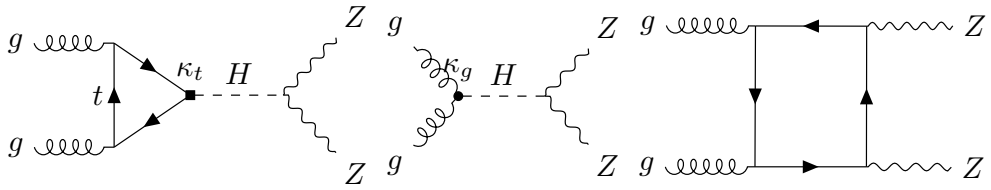


Figure 6: Feynman diagrams for the GF $gg \to ZZ$ process. The new physics effects from Eq. (2.6) display deviations on the coefficients $\kappa_t$ and $\kappa_g$ from the SM point $(\kappa_t, \kappa_g) = (1, 0)$.

Whereas Eq. (2.5) represents only a sub-set of high dimensional operators affecting the Higgs interactions [61, 62], we focus on it to highlight the effectiveness for the off-shell Higgs measurements to resolve a notorious degeneracy involving these terms. The gluon fusion Higgs production at low energy regime can be well approximated by the Higgs Low Energy Theorem [63, 64], where the total Higgs production cross-section scales as $\sigma_{\rm GF} \propto |\kappa_t + \kappa_g|^2$. Therefore, low energy measurements, such as on-shell and non-boosted Higgs production [65, 66, 67, 68, 69, 40, 70, 42, 71], are unable to resolve the $|\kappa_t + \kappa_g| =$ constant degeneracy. While the combination between the $t\bar{t}H$ and gluon fusion Higgs production have the potential to break this blind direction [72], we will illustrate that the Higgs production at the off-shell regime can also result into relevant contributions to resolve this degeneracy.

Since the Higgs boson decays mostly to longitudinal gauge bosons at the high energy regime, it is enlightening to inspect the signal amplitude for the longitudinal components. The amplitudes associated to each contribution presented in Fig. 6 can be approximated at $m_{ZZ} \gg m_t, m_H, m_Z$ by [73, 40, 42]

$$\begin{aligned}
\mathcal{M}_t^{++00} &\approx +\frac{m_t^2}{2m_Z^2} \log^2 \frac{m_{ZZ}^2}{m_t^2}\,, \\
\mathcal{M}_g^{++00} &\approx -\frac{m_{ZZ}^2}{2m_Z^2}\,, \\
\mathcal{M}_c^{++00} &\approx -\frac{m_t^2}{2m_Z^2} \log^2 \frac{m_{ZZ}^2}{m_t^2}\,.
\end{aligned} \tag{2.7}$$

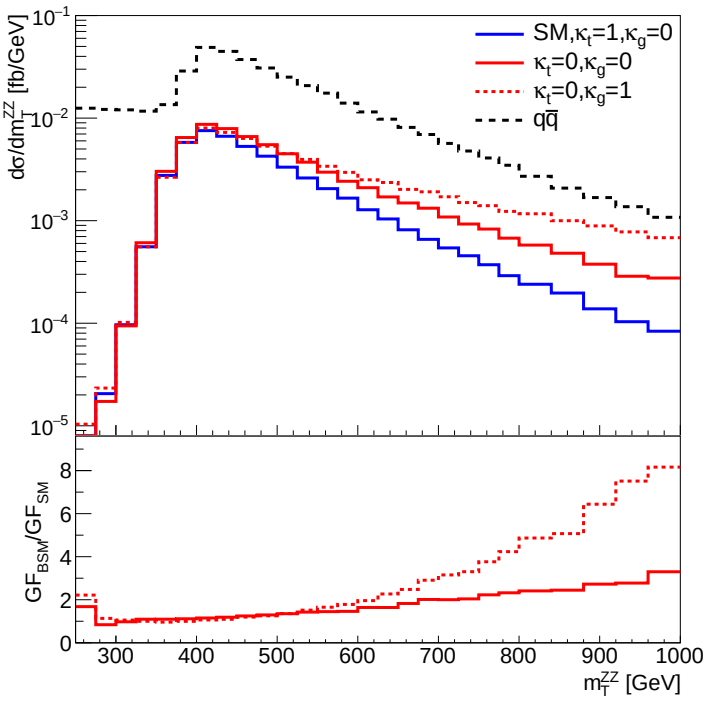


Figure 7: Transverse mass distributions $m_T^{ZZ}$ for the DY and GF $Z(\ell\ell)Z(\nu\nu)$ processes. The new physics effects are parametrized by deviations from the SM point $(\kappa_t, \kappa_g) = (1, 0)$. We follow the benchmark analysis defined in Sec 2.1.

Two comments are in order. First, both the $s$-channel top loop $\mathcal{M}_t$ and the continuum $\mathcal{M}_c$ amplitudes display logarithmic dependences on $m_{ZZ}/m_t$ at the far off-shell regime. In the SM scenario the ultraviolet logarithm between these two amplitudes cancel, ensuring a proper high energy behavior when calculating the full amplitude. Second, it is worth noting the difference in sign between the $s$-channel contributions $\mathcal{M}_t$ and $\mathcal{M}_g$. This results into a destructive interference between $\mathcal{M}_t$ and $\mathcal{M}_c$, contrasting to a constructive interference between $\mathcal{M}_g$ and $\mathcal{M}_c$. In the following, we will explore these phenomenological effects pinning down the new physics sensitivity with a higher precision.

Exploiting the larger rate for $ZZ \to \ell\ell\nu\nu$ than that for $ZZ \to 4\ell$ [40, 41, 42], we explore the off-shell Higgs physics at the HL-LHC. To simulate the full loop-induced effects, we implemented Eq. (2.6) into FeynRules/NLOCT [74, 75] through a new fermion state,

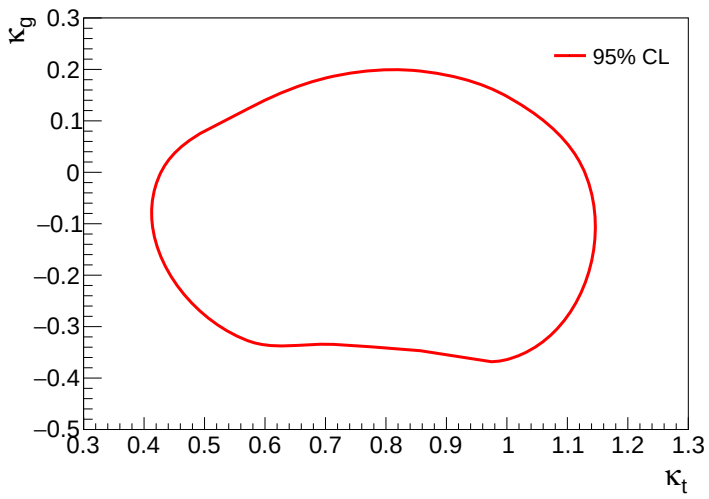


Figure 8: 95% CL bound on the coupling modifiers $\kappa_t$ and $\kappa_g$ when accounting for the off-shell Higgs measurement in the $Z(\ell\ell)Z(\nu\nu)$ channel. We assume the 14 TeV LHC with 3 ab$^{-1}$ of data.

and adjusting its parameters to match the low-energy Higgs interaction $HG_{\mu\nu}G^{\mu\nu}$ [63, 64]. Feynman rules are exported to a Universal FeynRules Output (UFO) [76] and the Monte Carlo event generation is performed with MadGraph5aMC@NLO [47].

In Fig. 7, we present the Drell-Yan (DY) and the gluon-fusion (GF) $m_T^{ZZ}$ distributions for different signal hypotheses. In the bottom panel, we display the ratio between the GF beyond the SM (BSM) scenarios with respect to the GF SM. In agreement with Eq. (2.7), we observe a suppression for the full process when accounting for the $s$-channel top loop contributions and an enhancement when including the new physics terms associated to $\mathcal{M}_g$ at high energies.

We follow the benchmark analysis defined in Sec. 2.1. After the BDT study, the resulting events are used in a binned log-likelihood analysis with the $m_T^{ZZ}$ distribution. This approach explores the characteristic high energy behavior for the new physics terms highlighted in Eq. (2.7) and illustrated in Fig. 7. We present in Fig. 8 the resulting 95% CL sensitivity to the $(\kappa_t, \kappa_g)$ new physics parameters at the high-luminosity LHC. In particular, we observe

that the LHC can bound the top Yukawa within $\kappa_t \approx [0.4, 1.1]$ at 95% CL, using this single off-shell channel. The observed asymmetry in the limit, in respect to the SM point, arises from the large and negative interference term between the $s$-channel and the continuum amplitudes. The upper bound on $\kappa_t$ is complementary to the direct Yukawa measurement via $ttH$ [77] and can be further improved through a combination with the additional relevant off-shell Higgs final states. The results derived in this section are competitive to the CMS HL-LHC prediction that considers the boosted Higgs production combining the $H \to 4\ell$ and $H \to \gamma\gamma$ channels [2]. The CMS projection results into an upper bound on the top Yukawa of $\kappa_t \lesssim 1.2$ at 95% CL.

### 2.3 Higgs-Top Form Factor

The fact that the observed Higgs boson mass is much lighter than the Planck scale implies that there is an unnatural cancellation between the bare mass and the quantum corrections. Since the mass of the Higgs particle is not protected from quantum corrections, it is well-motivated to consider that it may not be fundamental, but composite in nature [78, 79, 80, 81]. In such a scenario, the Higgs boson is proposed as a bound state of a strongly interacting sector with a composite scale $\Lambda$. In addition, the top quark, which is the heaviest particle in the SM, can also be composite. In this case, the top Yukawa coupling will be modified by a momentum-dependent form factor at a scale $q^2$ close to or above the new physics scale $\Lambda^2$. It is challenging to find a general construction for such form factor without knowing the underlying dynamics. Here, we will adopt a phenomenological ansatz motivated by the nucleon form factor [82]. It is defined as

$$\Gamma(q^2/\Lambda^2) = \frac{1}{(1 + q^2/\Lambda^2)^n}\,, \tag{2.8}$$

where $q^2$ is the virtuality of the Higgs boson. For $n = 2$, it is a dipole-form factor and corresponds to an exponential spacial distribution. Building upon Ref. [45], we study the impact of this form factor on $gg \to H^* \to ZZ$ process now with the complementary final state $\ell^+\ell^-\nu\overline{\nu}$.

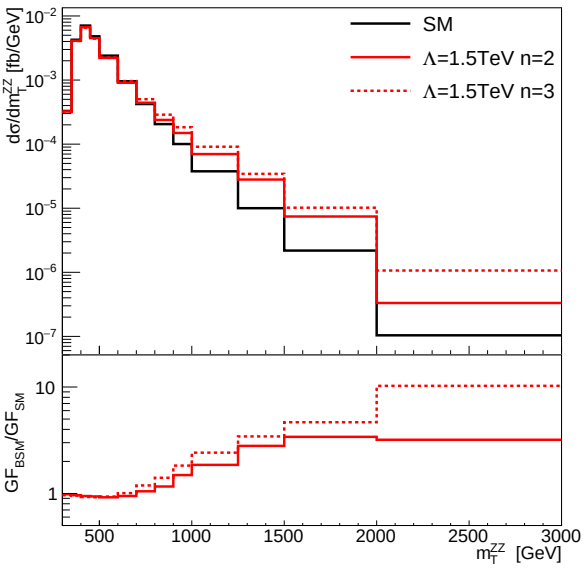


Figure 9: Transverse mass distribution $m_T^{ZZ}$ for $gg(\to H^*) \to Z(2\ell)Z(2\nu)$ in the Standard Model (black) and with a new physics form factor (red). We assume $n = 2, 3$ and $\Lambda = 1.5$ TeV for the form factor scenario.

In Fig. 9, we illustrate the $m_T^{ZZ}$ distribution for the full gluon fusion $gg(\to H^*) \to ZZ$ process. We show the Standard Model (black) and the form factor scenario (red). We assume $n = 2$ or 3 and $\Lambda = 1.5$ TeV for the depicted form factor scenarios. The differences between Standard Model and form factor cases become larger when the energy scales are comparable or above $\Lambda$ due to the suppression of destructive interference between Higgs signal and continuum background. Thus, we perform the same BDT procedure introduced in Sec. 2.1 followed by a binned log-likelihood ratio test in the $m_T^{ZZ}$ distribution to fully explore this effect. In Fig. 10, we display the sensitivity reach for the LHC in the Higgs-top form factor. We observe that the LHC can bound these new physics effects up to $\Lambda = 1.5$ TeV for $n = 2$ and $\Lambda = 2.1$ TeV for $n = 3$ at 95% CL. The large event rate for the $H^* \to ZZ \to \ell\ell\nu\nu$ signal results in a more precise probe to the ultraviolet regime than for the $H^* \to ZZ \to 4\ell$ channel, where the limits on the new physics scale are $\Lambda = 0.8$ TeV for $n = 2$ and $\Lambda = 1.1$ TeV for $n = 3$ at 95% CL [45].

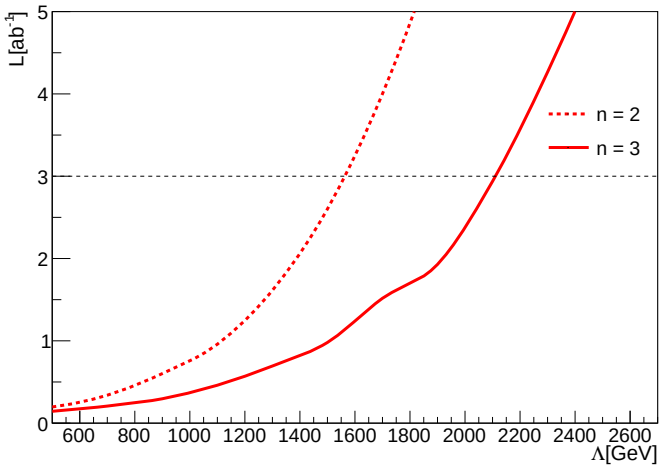


Figure 10: 95% CL sensitivity on the new physics scale $\Lambda$ as a function of the LHC luminosity. We assume the form factor in Eq. (2.8) with $n = 2$ (dashed line) and $n = 3$ (solid line) at the 14 TeV LHC.

Table 3: Comparison of the sensitivity reaches between $H^* \to ZZ \to \ell\ell\nu\nu$ in this study and $H^* \to ZZ \to 4\ell$ in the literature as quoted. All results are presented at 95% CL except for the Higgs width projection derived by ATLAS with 68% CL [1]. We assume that the Wilson coefficient for the EFT framework is given by $c_t = v^2/\Lambda^2_{EFT}$. Besides the $H \to 4\ell$ channel, Ref. [2] also accounts for the $H \to \gamma\gamma$ final state with a boosted Higgs analysis.

| | $\Gamma_H/\Gamma_H^{SM}$ | $\Lambda_{EFT}$ | $\Lambda^{n=2}_{Composite}$ |
|---|---|---|---|
| $H^* \to ZZ \to \ell\ell\nu\nu$ | 1.31 | 0.8 TeV | 1.5 TeV |
| $H^* \to ZZ \to 4\ell$ | 1.3 (68% CL) [1] | 0.55 TeV [2] | 0.8 TeV [45] |

## 3.0 Directly Probing the Higgs-top Coupling at High Scales

The top-quark Yukawa coupling ($y_t$) is the strongest interaction of the Higgs boson in the Standard Model (SM) with $y_t \sim 1$. Owing to its magnitude, it plays a central role in Higgs phenomenology in the SM and could be most sensitive to physics beyond the Standard Model (BSM) associated with the electroweak symmetry breaking [83]. It is crucial for the stability of the SM vacuum during the electroweak phase transition in the early universe [84, 85]. It yields the largest quantum correction to the Higgs boson mass and can trigger the electroweak symmetry breaking in many well-motivated new physics scenarios [86, 79, 87, 78, 88, 80]. Thus, the precise measurement of $y_t$ can be fundamental to pin down possible new physics effects.

The top-quark Yukawa coupling has been determined indirectly at the LHC from the Higgs discovery channel $gg \to h$ via the top-quark loop [89]. It can also be directly measured via top pair production in association with a Higgs boson, $t\bar{t}h$. The observation of this channel was reported in 2018 by both ATLAS and CMS collaborations, with respective significances of 6.3 and 5.2 standard deviations [90, 91]. These measurements confirm the SM expectation that the Higgs boson interacts with the top-quark with an order one Yukawa coupling. The high-luminosity LHC (HL-LHC) projections indicate that the top Yukawa will be probed to a remarkable precision at the end of the LHC run, reaching an accuracy of $\delta y_t \lesssim \mathcal{O}(4)\%$ [77].

The current measurements are performed near the electroweak scale $Q \sim v$. If the new physics scale $\Lambda$ is significantly larger than the energy probed at the LHC, the BSM effects generally scale as $(Q/\Lambda)^n$ with $n \geq 0$ [60, 61, 62], before reaching a new resonance. Therefore, it is desirable to enhance the new physics effects by exploring the high energy regime associated with the Higgs physics. Proposals have been made recently to study the off-shell Higgs signals $gg \to h^* \to VV$ [40, 41, 42, 43, 44, 45, 92]. This process could be sensitive to potential new physics of the $tth^*$ and $VVh^*$ interactions or a $h^*$ propagation at high energy scales $Q > v$.

In the present study, we **directly** explore the Higgs-top coupling at high energy scales

using the $t\bar{t}h$ production channel. For an on-shell Higgs production with high transverse momentum, this process effectively probes the top-quark Yukawa interaction at a high scale in both the space-like and time-like regimes. In contrast, the off-shell Higgs physics probes the complementary physics only in the time-like domain [44, 45, 92]. As a concrete formulation, we study the BSM effects to the Higgs-top Yukawa in the Effective Field Theory (EFT) framework, focusing on two relevant higher dimensional contributions. Then, we move on to a BSM hypothesis that features a non-local momentum-dependent form factor of the Higgs-top interaction [45, 92]. This form factor generally captures the top Yukawa composite substructure. To combine the large event yield with a high energy physics probe, we focus on the channel with the largest Higgs decay branching fraction, $\mathcal{BR}(h \to b\bar{b}) \sim 58\%$, in association with jet substructure techniques at the boosted Higgs regime.

The rest of the chapter is organized as follows. In Section 3.1, we present the theoretical parameterization associated with the potential new physics for the Higgs-top couplings in the EFT framework and an interaction form factor. We then derive the new physics sensitivity to those interactions in Section 3.2, featuring the effects that benefit with the energy enhancement at the boosted Higgs regime.

### 3.1 New Physics parametrization

In this section, we describe two qualitatively different new physics parametrizations for beyond-the-Standard Model effects to the Higgs-top coupling at high energy scales. The first one considered is in the effective field theory framework by adding in a few relvant dimension-6 operators that are results from integrating out some heavy degrees of freedom mediating the Higgs and top interactions. The second formulation is a non-local Higgs-top form factor, motivated from a strongly interacting composite theory for the Higgs and top quarks. These two forms of new physics parameterizations are quite representative in capturing the general features of the BSM couplings for the Higgs and the top quark.

### 3.1.1 Effective Field Theory

The Standard Model Effective Field Theory (SMEFT) provides a consistent bottom-up framework to search for new physics [61, 62, 93, 94, 95, 43, 96]. In this scenario, the beyond the SM particles are too heavy to be produced on-shell. The new states can be integrated out and parametrized in terms of higher dimension operators as contact interactions [60]. In general, the EFT Lagrangian can be written as

$$\mathscr{L}_{\text{EFT}} = \mathscr{L}_{\text{SM}} + \sum_i \frac{c_i}{\Lambda^2}\mathcal{O}_i + \mathcal{O}\left(\frac{1}{\Lambda^4}\right), \tag{3.1}$$

where $\Lambda$ is the scale of new physics, $\mathcal{O}_i$ are effective operators of dimension-six compatible with the SM symmetries, and $c_i$ are corresponding Wilson coefficients. Higher dimensional operators can modify the existing SM interactions, as well as generate new Lorentz structures, both of which can give rise to phenomenologically relevant energy enhancements in the scattering amplitudes.

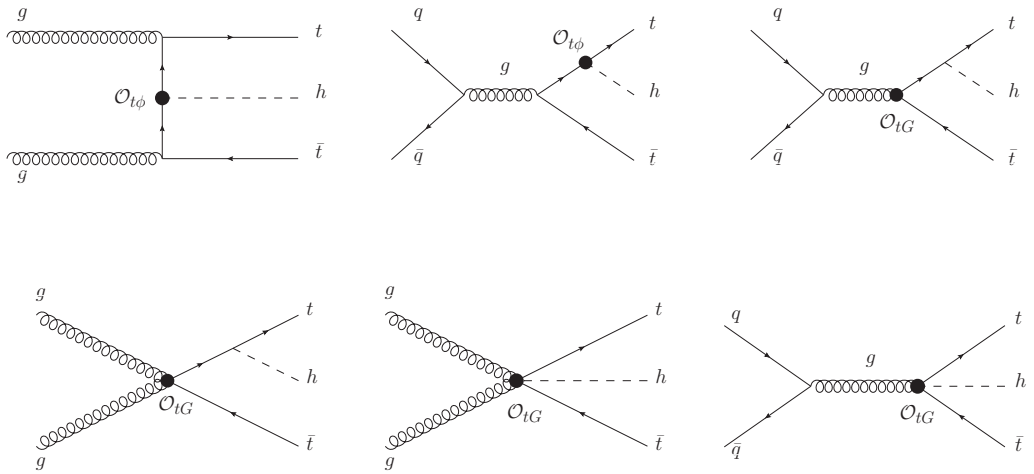


Figure 11: Representative Feynman diagrams contributing to $t\bar{t}h$ production. The black dots represent the BSM vertices arising from the EFT operators.

We follow the SMEFT framework to study the new physics effects to the Higgs-top coupling at high scales. We adopt the Warsaw basis of operators [62] and focus on two-fermion operators, leading to contributions to $t\bar{t}h$ production at the LHC which are relatively unconstrained

$$\mathcal{O}_{t\phi} = (H^\dagger H)(\bar{Q}t)\tilde{H} + \text{h.c.}\,, \tag{3.2}$$

$$\mathcal{O}_{tG} = g_s(\bar{Q}\sigma^{\mu\nu}T_A t)\tilde{H}G^A_{\mu\nu} + \text{h.c.}\,. \tag{3.3}$$

The first new physics operator, $\mathcal{O}_{t\phi}$, rescales the SM top Yukawa coupling. The second one, $\mathcal{O}_{tG}$, corresponds to the chromomagnetic dipole moment of the top-quark. Besides modifying the $gtt$ vertex in the SM, $\mathcal{O}_{tG}$ also gives rise to new interaction vertices, namely $ggtt$, $gtth$ and $ggtth$. While $\mathcal{O}_{tG}$ results in phenomenological effects to the associated $t\bar{t}$ processes, it amounts to possibly significant new physics sensitivity in the $t\bar{t}h$ channel [97]. Hence, we incorporate it in our analysis exploring its high energy behavior. In Fig. 11, we present a representative set of Feynman diagrams for $t\bar{t}h$ production arising from the EFT interactions. The experimental LHC analyses constrain these Wilson coefficients at 95% Confidence Level (CL) to the ranges [98, 99]

$$c_{t\phi}/\Lambda^2 = [-2.3, 3.1]/\text{TeV}^2, \quad c_{tG}/\Lambda^2 = [-0.24, 0.07]/\text{TeV}^2.$$

Guided by these results, we choose illustrative values of the coefficients as

$$|c_{tG}/\Lambda^2| = 0.1 \text{ TeV}^{-2} \quad \text{and} \quad |c_{t\phi}/\Lambda^2| = 1 \text{ TeV}^{-2}, \tag{3.4}$$

for our following representative kinematic distributions. For recent phenomenological SMEFT global fit studies, see Refs. [93, 94].

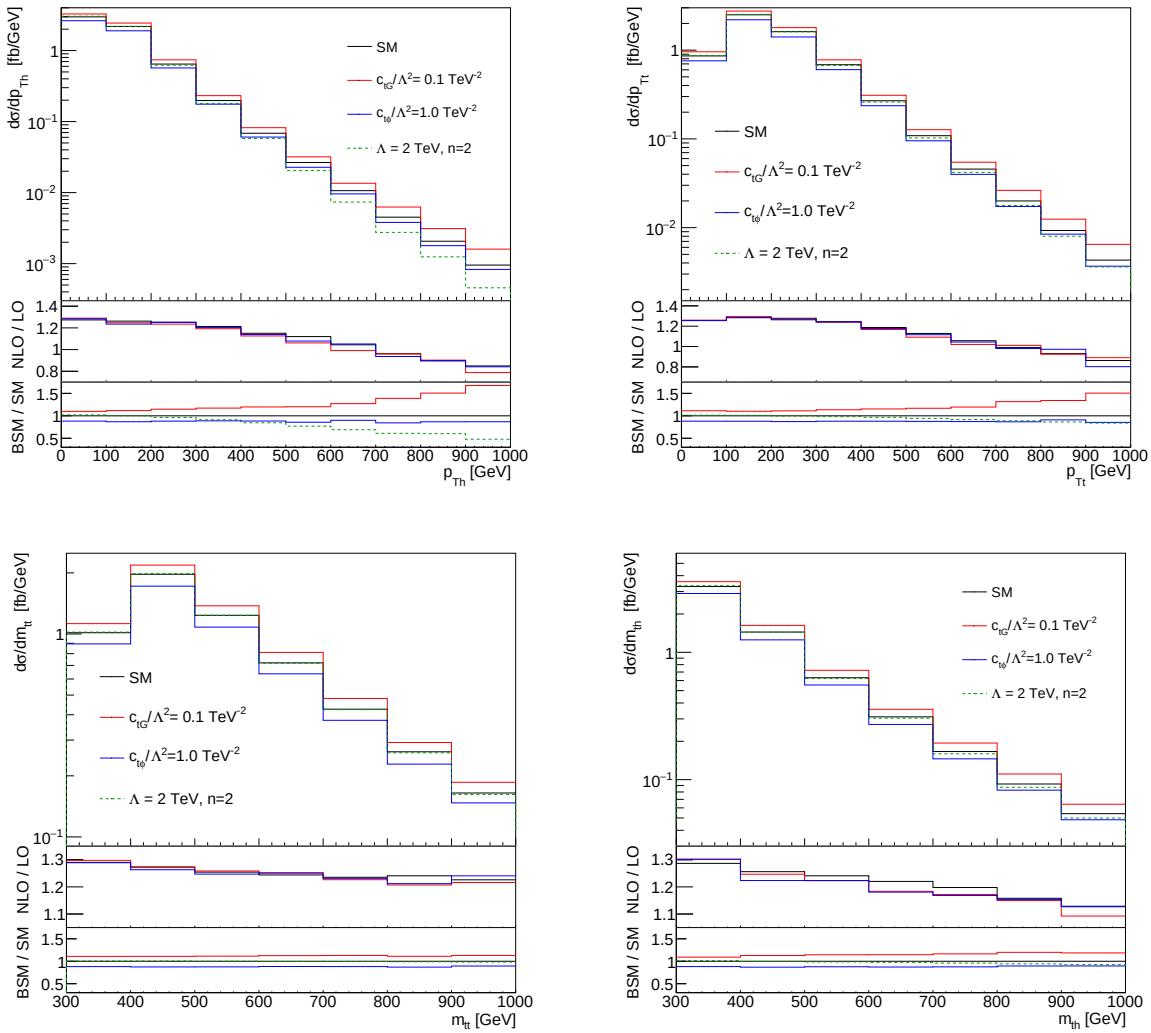


Figure 12: Top panels: Transverse momentum distributions for the Higgs boson $p_{Th}$ (left) and the hardest top-quark $p_{Tt}$ (right). Bottom panels: Invariant mass distributions for the top pair $m_{tt}$ (left) and the Higgs and top-quark $m_{th}$ (right). Each panel shows on the top the $t\bar{t}h$ sample in the SM and new physics scenarios. The results are presented at the NLO QCD fixed order. We also show the local NLO $K$-factor (middle panel in each figure as NLO/LO) and the ratio between new physics and SM scenarios (bottom panel in each figure as BSM/SM). We assume the LHC at 14 TeV.

### 3.1.2 Higgs-Top coupling form-factor

The top-quark Yukawa coupling has a special role in the naturalness problem, displaying the dominant quantum corrections to the Higgs mass. Thus, it is crucially important to probe the Higgs-top interaction at high scales into the ultra-violet regime. It is well-motivated to consider that the top-quark and Higgs boson may not be fundamental, but composite particles arising from strongly interacting new dynamics at a scale $\Lambda$ [78, 80, 81, 100]. In such scenarios, the top Yukawa may exhibit a momentum-dependent form-factor near or above the new physics scale $\Lambda$, rather than a point-like interaction. It is challenging to write a form-factor, in a general form, without prior knowledge of the underlying strong dynamics of the specific composite scenario. Inspired by the nucleon form-factor [82], we adopt the following phenomenological ansatz

$$\Gamma(Q^2/\Lambda^2) = \frac{1}{(1+Q^2/\Lambda^2)^n}\,, \tag{3.5}$$

where $Q$ is the energy scale associated with the physical process. This educated guess results in a dipole form-factor for the $n = 2$ scenario with an exponential spatial distribution in a space-like probe. Higher values of $n$ correspond to higher multi-poles, typically leading to a stronger suppression.

## 3.2 Analysis

To probe these new physics contributions, we explore the $pp \to t\bar{t}h$ channel at high energy scales. We combine the large signal event rate with controlled backgrounds, studying the boosted $h \to b\bar{b}$ final state in association with leptonic top-quark pair decays. The signal is defined in the four $b$-tag sample and displays two opposite sign leptons. The leading backgrounds, in order of relevance, are $t\bar{t}b\bar{b}$ and $t\bar{t}Z$.

We perform the signal and background event generation with `MadGraph5_aMC@NLO` [47]. The $t\bar{t}h$ and $t\bar{t}Z$ samples are generated at NLO QCD and the $t\bar{t}b\bar{b}$ sample at LO. The dimension-six EFT contributions are added through the FeynRules model `SMEFT@NLO` [101].

This implementation grants one-loop QCD computations, accounting for the EFT contributions. In particular, it incorporates relevant extra radiation effects at the matrix element level [102]. Shower, hadronization, and underlying event effects are simulated with `Pythia8` [53] using the `Monash` tune [103]. We use `MadSpin` to properly describe the top-quark decays, accounting for spin correlation effects [51]. We adopt the parton distribution functions from MMHT2014 NLO with $\alpha_S(m_Z) = 0.118$ [104] in the five flavor scheme. Additional relevant parameters are $m_t = 172$ GeV, $m_h = 125$ GeV, $m_Z = 91.1876$ GeV, $m_W = 79.82$ GeV, and $G_F = 1.16637 \times 10^{-5}$ GeV$^{-2}$. We set our scales to a constant value of $\mu_F = \mu_R = m_t + m_h/2$ to align better with previous studies [97]. We assume the LHC at $\sqrt{s} = 14$ TeV.

Robust new physics studies at the LHC usually come hand in hand with precise theoretical calculations. The impact of the higher order QCD corrections, which can be conventionally estimated by a $K$-factor (*i.e.* the ratio between the NLO and LO predictions), usually result in significant contributions. To illustrate the higher order and new physics effects at high energies, we present in Fig. 12 the NLO fixed order parton level distribution for several relevant kinematic observables associated with the $t\bar{t}h$ signal sample: the transverse momentum distribution for the Higgs boson $p_{Th}$ (upper left), for the hardest top-quark $p_{Tt}$ (upper right), the invariant mass distribution for the top pair $m_{tt}$ (lower left), and for the Higgs and top-quark $m_{th}$ (lower right). We observe that the higher order QCD corrections are correlated with the kinematic observables, resulting in about $20\% - 30\%$ variation (as seen in the panels of NLO/LO) and cannot be captured by a global NLO $K$-factor. It is thus crucial to include the higher order predictions in the full differential analysis.

New physics contributions may sensitively depend on the kinematics as well, as demonstrated in the panels of BSM/SM in Fig. 12. High transverse momenta of an on-shell top quark or Higgs boson could probe the space-like regime for the top-Higgs interactions, while the high invariant mass of the $tH$ system could be sensitive to the time-like regime from heavy states in $s$-channels. First, we observe sizable energy enhancement arising from the $\mathcal{O}_{tG}$ operator, in particular, for the transverse Higgs momentum distribution (as seen in the panels of BSM/SM), starting with a 10% increase at the non-boosted regime $p_{Th} < 100$ GeV, adding up to 65% for $p_{Th} = 1$ TeV. In contrast, due to the generic dipole suppression, the

form-factor scenario displays a depletion in cross-section at higher energies. The rate is reduced by 5% at $p_{Th} = 200$ GeV, reaching 55% suppression at $p_{Th} = 1$ TeV. For the form-factor scenario, we adopt a representative scale $Q = p_{Th}$. New physics effects associated with the operator $\mathcal{O}_{t\phi}$ do not result in a distinct energy profile with respect to the SM. In the $t\bar{t}h$ process, this operator only contributes with a shift to the top Yukawa, resulting in a flat rescale with respect to the SM cross-section, independent of the process energy scale. Despite the absence of a manifest energy enhancement, this new physics contribution can also benefit from our high energy scale analysis due to more controlled backgrounds at the boosted Higgs regime, as we will show in the following.

The boosted Higgs analysis, in combination with jet substructure techniques effectively suppress the initially overwhelming backgrounds for the $t\bar{t}h$ signal with the dileptonic top decays and $h \to b\bar{b}$, as first shown in Ref. [105]. Here we follow a similar strategy. We start our analysis requiring two isolated and opposite sign leptons with $p_{T\ell} > 10$ GeV and $|\eta_\ell| < 3$. For the hadronic component of the event, we first reconstruct jets with the Cambridge-Aachen algorithm with $R = 1.2$ [106], requiring at least one boosted fat-jet with $p_{TJ} > 200$ GeV and $|\eta_J| < 3$. We demand that one of the fat-jets be Higgs tagged with the Butterworth-Davison-Rubin-Salam (BDRS) algorithm [107, 108]. Higgs tagging of the fat-jet via the BDRS algorithm involves identifying three subjets within the fat-jet. This is done by shrinking the jet radius until the fat-jet splits into three filtered jets. The radius of separation among the filtered jets is defined as $R_{\rm filt} = \min(0.3, R_{bb}/2)$. Among the three filtered jets, the two hardest are required to be $b$-tagged, while the third filtered jet tracks the dominant $\mathcal{O}(\alpha_s)$ radiation from the Higgs decay.

As we only have one hadronic heavy particle decay, namely the Higgs boson, we proceed with the event reconstruction using a smaller jet size to further reduce the underlying event contamination. Thus, we remove all the hadronic activity associated with the Higgs fat-jet and re-cluster the remaining particles with the jet radius $R = 0.4$, using the anti-k$_t$ jet algorithm. We demand two $b$-tagged jets with $p_{tb} > 30$ GeV and $|\eta_b| < 3$. As our final state displays in total four $b$-tagged jets, we exploit the improvements in the central tracking system, that will be in operation for the HL-LHC run, to enhance the event rate for our signal. Based on the ATLAS report [109], we assume 85% $b$-tagging efficiency and 1% mistag rate

for light-jets. To further suppress the backgrounds, the filtered mass for the Higgs candidate is imposed to be around the Higgs boson mass $|m_h^{\rm BDRS} - 125 \text{ GeV}| < 10$ GeV. We show in Table 4 more details on the cut-flow analysis.

Table 4: Cut-flow for signal and backgrounds at LHC $\sqrt{s} = 14$ TeV. The selection follows the BDRS analysis described in the text. Rates are in units of fb and account for 85% (1%) $b$-tag (mistag) rate, hadronization, and underlying event effects.

| cuts | $t\bar{t}h$ | $t\bar{t}b\bar{b}$ | $t\bar{t}Z$ |
|---|---|---|---|
| BDRS $h$-tag, $p_{T\ell} > 10$ GeV, $\lvert\eta_\ell\rvert < 3$, $n_\ell = 2$ | 3.32 | 6.35 | 1.02 |
| $p_{Tj} > 30$ GeV, $\lvert\eta_j\rvert < 3$, $n_j \geq 2$, $n_b$=2 | 0.72 | 1.97 | 0.22 |
| $\lvert m_h^{\rm BDRS} - 125\rvert < 10$ GeV | 0.15 | 0.14 | 0.009 |

### 3.2.1 Scale for the EFT operators

In Fig. 13, we go beyond the partonic level calculation and display the hadron level transverse momentum distribution ($p_{Th}$) for the Higgs boson candidate from the $pp \to t\bar{t}h$ channel in the SM and the EFT contributions, in addition to the leading backgrounds $t\bar{t}b\bar{b}$ and $t\bar{t}Z$. We observe that the boosted Higgs search dovetails nicely with our BSM physics study as presented in Fig. 12. At the higher energy scales, both the backgrounds get further depleted and the new physics effects become more prominent. In particular, we observe a large enhancement from the $\mathcal{O}_{tG}$ contributions at the high energy scales.

To explore the sensitivity reach for these effects in the boosted regime, we perform a binned log-likelihood analysis on the $p_{Th}$ distribution. In Fig. 14, we present the 68% and 95% CL limits on the Wilson coefficients $(c_{tG}/\Lambda^2, c_{t\phi}/\Lambda^2)$. We assume the HL-LHC at 14 TeV with 3 ab$^{-1}$ of data. To infer the uncertainty on the EFT expansion, we present the results accounting for terms up to linear and quadratic order on the Wilson coefficient $c_i/\Lambda^2$. We observe only small differences between these two scenarios, which is a good indication of the robustness of our results.

CMS has recently reported an EFT interpretation using associated top quark production

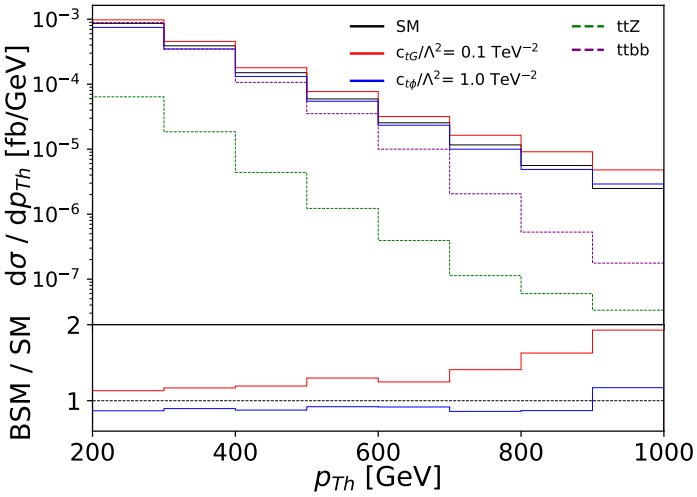


Figure 13: Transverse momentum distribution of the Higgs boson $p_{Th}$ for the $t\bar{t}h$ sample in the SM (black) and new physics scenarios with $c_{tG}/\Lambda^2 = 0.1$ TeV$^{-2}$ (red), $c_{t\phi}/\Lambda^2 = 1$ TeV$^{-2}$ (blue). The leading backgrounds $t\bar{t}b\bar{b}$ (purple) and $t\bar{t}Z$ (green) are also presented. We assume the LHC at 14 TeV.

data with an integrated luminosity of $\mathcal{L} = 41.5$ fb$^{-1}$ [110]. The signal samples include, in particular, the $t\bar{t}h$ and $thq$ processes, being direct sensitive to the top-quark Yukawa coupling. The resulting constraint at the 95% CL for the chromomagnetic operator leads to two regions $c_{tG}/\Lambda^2 = [-1.26, -0.69]$ TeV$^{-2}$ and $[0.08, 0.79]$ TeV$^{-2}$. The same holds for the $\mathcal{O}_{t\phi}$ operator where $c_{t\phi} = [-14.12, -1.46]$ TeV$^{-2}$ and $[32.30, 44.48]$ TeV$^{-2}$. While CMS does not focus on the very high energy scales and uses the leptonic Higgs decays, we explore the largest Higgs branching ratio, $h \to b\bar{b}$, in the boosted Higgs regime, and thus obtaining significantly higher sensitivities at the HL-LHC.

### 3.2.2 Probing the form-factor

In Fig. 15, we present the transverse momentum distribution ($p_{Th}$) for the Higgs boson candidate from the $pp \to t\bar{t}h$ channel in the SM and the form-factor contribution. We

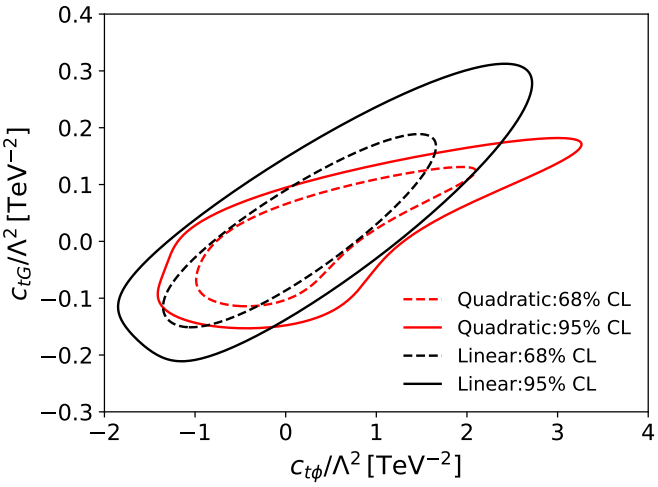


Figure 14: 95% (full line) and 68% (dashed line) CL limits on the Wilson coefficients $(c_{tG}/\Lambda^2, c_{t\phi}/\Lambda^2)$ at the 14 TeV HL-LHC with 3 $ab^{-1}$ of data. The results are presented both at the linear (black) and quadratic (red) order in dimension-6 SMEFT operator coefficients.

consider two hypotheses $n = 2$ and $n = 3$ with the new physics scale $\Lambda = 2$ TeV. While it is challenging to probe the BSM effects at relatively small scales, these contributions can be effectively enhanced at the boosted regime. For instance, starting at $p_{Th} \sim 200$ GeV with $n = 2$ ($n = 3$), we observe a 5% (9%) effect. Moving to $p_{Th} \sim 400$ GeV, the new physics results in larger depletion of 18% (25%) with respect to the SM hypothesis.

Our relatively large event rate with the boosted $h \to b\bar{b}$ analysis, grants probes at large energy scales with relevant statistics. Hence, we explore the full profile of the $p_{Th}$ distribution through a binned log-likelihood analysis. The new physics sensitivity is presented in Fig. 16. The HL-LHC, with 3 ab$^{-1}$ of data, will be able to probe these new physics effects up to a scale of $\Lambda = 2.1$ TeV for $n = 2$ and $\Lambda = 2.7$ TeV for $n = 3$ at 95% CL. These results are complementary to the off-shell Higgs analyses, $gg \to h^* \to ZZ$. For the latter, assuming $n = 3$, the limits on the new physics scale are $\Lambda = 1.1$ TeV for the $4\ell$ final state and $\Lambda = 2.1$ TeV for the $\ell\ell\nu\nu$ final state [45, 92].

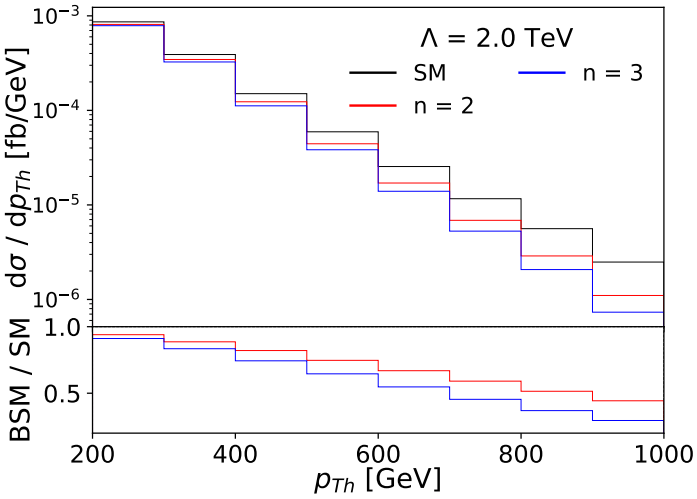


Figure 15: Transverse momentum distribution of the Higgs boson $p_{Th}$ for the $t\bar{t}h$ sample in the SM (black) and new physics scenarios with $n = 2$ (red) and $n = 3$ (blue), assuming $\Lambda = 2$ TeV. We assume the LHC at 14 TeV.

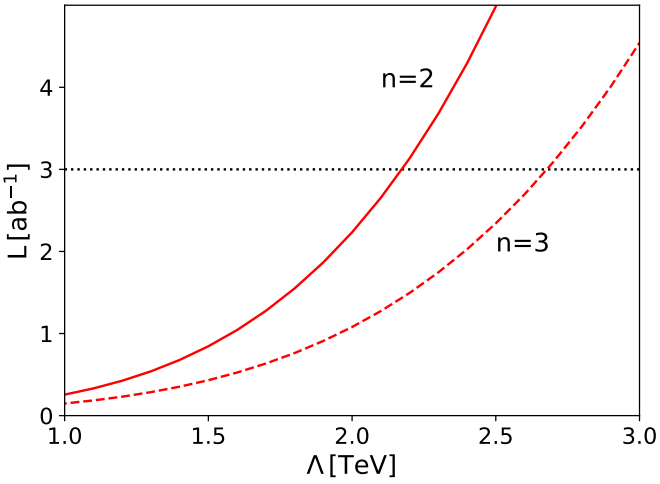


Figure 16: 95% CL sensitivity on the new physics scale $\Lambda$ as a function of the LHC luminosity. We consider two form-factor scenarios: $n = 2$ (solid line) and $n = 3$ (dashed line).

Finally, we give a summary table which compares the reach of new physics scale between this work and others in Table.5. We can see from the table that the direct probe of $t\bar{t}h$ is very competitive and could result in a better BSM sensitivity compared to other channels.

Table 5: Summary results from the $t\bar{t}h$ studies for the Higgs-top coupling at high scales in terms of the dimension-6 operators and general form-factor scenarios. The results are shown at 95% CL, and we assume the HL-LHC at 14 TeV with 3 ab$^{-1}$ of data. For comparison, we also show the results from off-shell $h^*$ studies, the ATLAS Higgs combination with 139 fb$^{-1}$, and the CMS top pair bound with 35.9 fb$^{-1}$.

| | channel | $c_i/\Lambda^2$ [TeV$^{-2}$] 95% CL bounds | $\Lambda/\sqrt{c_i}$ [TeV] BSM scale |
|---|---|---|---|
| $c_{t\phi}$ | $t\bar{t}h$ (this work) | $[-1.04, 1.00]$ | 1.0 |
| | $h^* \to ZZ \to \ell\ell\nu\nu$ [92] | $[-2.8\ ,\ 1.5]$ | 0.6 |
| | $h^* \to ZZ \to 4\ell$ [45] | $[-3.3\ ,\ 3.3]$ | 0.55 |
| | Higgs comb. ATLAS [98] | $[-2.3\ ,\ 3.1]$ | 0.57 |
| $c_{tG}$ | $t\bar{t}h$ (this work) | $[-0.11\ ,\ 0.12]$ | 2.9 |
| | $t\bar{t}$ CMS [99] | $[-0.24\ ,\ 0.07]$ | 2.1 |
| form-factor $n = 2$ | $t\bar{t}h$ (this work) | - | 2.1 |
| | $h^* \to ZZ \to \ell\ell\nu\nu$ [92] | - | 1.5 |
| | $h^* \to ZZ \to 4\ell$ [45] | - | 0.8 |
| form-factor $n = 3$ | $t\bar{t}h$ (this work) | - | 2.7 |
| | $h^* \to ZZ \to \ell\ell\nu\nu$ [92] | - | 2.1 |
| | $h^* \to ZZ \to 4\ell$ [45] | - | 1.1 |

## 4.0 Leptonic Scalars and Collider Signatures in a UV-complete Model

Explanation of tiny but non-zero masses of neutrinos, as confirmed in various experiments over the past two decades [3], requires new physics beyond the Standard Model (SM). In addition to the origin of their masses and mixing, neutrinos pose many more unanswered questions. For example, we still do not know whether the neutrino masses are of Dirac-type or Majorana-type; see Ref. [111] for a recent review. We would also like to understand whether the neutrino sector contains new interactions beyond those allowed by the SM gauge structure, *i.e.* the so-called non-standard interactions (NSIs); see Ref. [112] for a recent status report. Furthermore, the origin of dark matter (DM) is an outstanding puzzle and it is conceivable that these two puzzles could be somehow correlated at a fundamental level [113, 114, 115]. We also wonder whether the leptonic sector breaks CP-symmetry and whether it is responsible for the observed matter-antimatter asymmetry in the Universe [116]. In order to address these outstanding puzzles, construction of neutrino models and investigation of their predictions at various experiments are highly motivated.

If neutrinos are Majorana particles, lepton number $L$, which is an accidental global symmetry of the SM Lagrangian, must be broken either at tree-level or loop-level. On the other hand, if neutrinos are Dirac particles, lepton number (or some non-anomalous symmetry that contains $L$, such as $B - L$) remains a good symmetry of the Lagrangian. We will focus on this latter case, assuming that $B - L$ is conserved even in presence of higher-dimensional operators. Thus, any new, additional degrees of freedom must be charged appropriately under global $B - L$ [117]. In a recent paper [118], motivated by certain observational considerations at the LHC and beyond, we considered the possibility that Dirac neutrinos could exhibit NSIs with a new (light) scalar field $\phi$ which has a $B-L$ charge of $+2$ but is a singlet under the SM gauge group. These were dubbed as "leptonic scalars", which can only couple to right-handed neutrinos ($\nu_R$) (or left-handed anti-neutrinos) like $\nu_R^T C \nu_R \phi$ at the renormalizable level. Then the question arises as to how these leptonic scalars couple to the SM fields. At the dimension-6 level, we can write an effective coupling

of the form

$$\frac{1}{\Lambda^2}(LH)(LH)\phi\,, \tag{4.1}$$

where $L$ and $H$ are the SM lepton and Higgs doublets, respectively, and $\Lambda$ is the new physics scale. After electroweak (EW) symmetry breaking, the operator (4.1) yields flavor-dependent NSIs of neutrinos with the leptonic scalar of the form $\lambda_{\alpha\beta}\phi\nu_\alpha\nu_\beta$. Furthermore, at energy scales below the mass of $\phi$, this leads to an effective non-standard neutrino self-interaction, which could bring down the measurement of Hubble parameter from Cosmic Wave Background (CMB) by modifying the effective number of neutrinos, thus relax the tension of Hubble parameter between CMB measurement and low-redshift measurement [119, 120, 121, 122, 123, 124].

Our goal in this paper is to find an ultraviolet (UV)-completion of the operator (4.1) and to test the model at the ongoing LHC and future 100 TeV colliders, such as the Future Circular Collider (FCC-hh) at CERN [125] and the Super Proton-Proton Collider (SPPC) in China [126]. To be concrete, we adopt a Type-II seesaw motivated neutrino mass model [127, 128, 129, 130, 131, 132], which can also account for the baryon asymmetry in the Universe [133]. In our model the neutral component of the triplet scalar field $\Delta$ does not acquire a vacuum expectation value (VEV), which keeps the custodial symmetry intact. The lepton number is not broken and the neutrinos are Dirac-type in this model. We also add a SM-singlet complex scalar field $\Phi$, which gives rise to the leptonic scalar $\phi$ in the model. Beyond the NSIs between the active neutrinos and the leptonic scalar, the particle spectrum and new interactions in this model lead to rich phenomenology and consequently new observable signatures. In some other UV-complete models, the effective interactions of $\phi$ with the SM neutrinos stemming from Eq. (4.1) might also be relevant to DM phenomenology [134, 135, 121, 136, 123].

In this paper we will show that the distinguishing features of the signatures of our UV-complete model compared to the standard Type-II seesaw model is due to the new sources of missing energy carried away by $\phi$, which would help the model to be detected at the ongoing LHC and future higher-energy colliders. After taking into account the current limits from the low-energy lepton flavor violating (LFV) constraints (cf. Table 7 and Fig. 18)

and the theoretical limits from perturbativity and unitarity (see Fig. 19), we consider three scenarios with respectively small, large and intermediate Yukawa couplings of the leptonic scalar $\phi$. In all these scenarios, $\phi$ can be produced either from the doubly-charged scalar $H^{\pm\pm} \to W^{\pm}W^{\pm}\phi$ or from the singly-charged scalar $H^{\pm} \to W^{\pm}\phi -$ channels which are unique and absent in the standard Type-II seesaw. As the leptonic scalar $\phi$ decays exclusively into neutrinos, these new channels will lead to same-sign dilepton plus missing transverse energy plus jets signal at the hadron colliders. Detailed cut-based analysis is carried out for both scenarios, and the technique of Boosted Decision Tree (BDT) [137] is also utilized to improve the observational significance (see Tables 9 and 11). We find that the mass of doubly-charged scalars in the small and large Yukawa coupling scenarios can be probed up to respectively 800 GeV and 1.1 TeV at the $2\sigma$ significance, corresponding to a 95% confidence level, in the new channels at the high-luminosity LHC (HL-LHC) with integrated luminosity of 3 ab$^{-1}$, and can be improved up to 3.8 TeV and 4 TeV respectively at future 100 TeV colliders with luminosity of 30 ab$^{-1}$. This can be further improved in the intermediate Yukawa coupling case, with the help of increasing leptonic decay channel of the doubly-charged scalar. We also show that since in the large Yukawa coupling case, the missing energy is completely from the leptonic scalar in the associate production channel $pp \to H^{\pm\pm}H^{\mp}$, its mass can be determined with an accuracy of about 10% at the HL-LHC.

The rest of the chapter is organized as follows. In Section 4.1, we present the model details and lay out relevant experimental and theoretical constraints, including the key parameters and resultant main decay channels of $H^{\pm\pm}$ and $H^{\pm}$ in Section 4.1.1, the current LFV constraints on $H^{\pm\pm}$ in Section 4.1.2, and the high-energy limits from perturbativity and unitarity in Section 4.1.3. In Section 4.2, we discuss our search strategy at the LHC and future 100 TeV hadron colliders, presenting the small Yukawa coupling case in Section 4.2.1, large Yukawa coupling scenario in Section 4.2.2, and the intermediate Yukawa coupling case in Section 4.2.3. We show the discovery potential by utilizing the cut-based analysis and the BDT techniques, and obtain the prospect for determining the mass of $\phi$ in the large Yukawa coupling case even though the scalar $\phi$ escapes from the detectors as missing energy. For the sake of completeness, the complete set of Feynman rules for the model are listed in Appendix A. The functions $G$ and $\mathcal{F}$ for some three-body decays are given in Appendix B.

The renormalization group equations (RGEs) for the couplings are detailed in Appendix C. The perturbativity limits are analytically derived in Appendix D, and the unitarity limits are described in Appendix E.

### 4.1 The model

In this section, we present a global $(B-L)$-conserved UV-complete model of a leptonic scalar, which is motivated by the well-known Type-II seesaw model [127, 128, 129, 130, 131, 132]. The enlarged particle content of the model includes a leptonic complex scalar $\Phi$, which is a singlet under the SM gauge groups and carries a $B-L$ charge of +2. The model contains also an $SU(2)_L$ triplet scalar $\Delta$ with hypercharge +1 and $B-L$ charge +2:

$$\Delta = \begin{pmatrix} \frac{1}{\sqrt{2}}\delta^+ & \delta^{++} \\ \delta^0 & -\frac{1}{\sqrt{2}}\delta^+ \end{pmatrix} \tag{4.2}$$

and three SM-singlet $B-L=-1$ right-handed neutrino fields $\nu_{R_i}$ $(i=1,2,3)$.

The allowed Yukawa interactions in the model are given by

$$-\mathcal{L}_Y = y_{\nu,\,\alpha\beta}\overline{L}_\alpha H \nu_{R_\beta} + Y_{\alpha\beta} L_\alpha^{\mathsf{T}} C i\sigma_2 \Delta L_\beta + \tilde{y}_{\nu,\,\alpha\beta}\nu_{R_\alpha}^{\mathsf{T}} C \nu_{R_\beta}\Phi + \text{H.c.}\,, \tag{4.3}$$

where $\alpha,\ \beta = e,\ \mu,\ \tau$ are the lepton flavor indices, $C$ is the charge-conjugation operator, $\sigma_2$ is the second Pauli matrix, $y_\nu$ are the SM-like Yukawa couplings of the neutrinos, $Y_{\alpha\beta}$ are the new leptonic Yukawa couplings of the triplet that govern the heavy scalar phenomenology, and $\tilde{y}_\nu$ are the Yukawa couplings of the leptonic scalar $\Phi$ to the right-handed neutrinos. In a $(B-L)$-conserved theory where $\Delta$ and $\Phi$ do not acquire any VEV, neutrinos are Dirac fermions and non-zero neutrino masses can be generated after the EW symmetry breaking from the first term of the Yukawa Lagrangian given in Eq. (4.3), just like the other fermions in the SM. However, one requires $y_\nu \lesssim 10^{-12}$ in order to satisfy the absolute neutrino mass constraints [27, 138].

The kinetic and potential terms of the scalar sector are given by

$$\mathcal{L}_{\text{Scalar}} = (D_\mu H)^\dagger (D^\mu H) + \text{Tr}[(D_\mu \Delta)^\dagger (D^\mu \Delta)] + (\partial_\mu \Phi)^\dagger (\partial^\mu \Phi) - V(H,\Delta,\Phi), \tag{4.4}$$

where the covariant derivatives are given by

$$D_\mu H = \partial_\mu H - i\frac{g_L}{2}W_\mu^a \sigma_a H - i\frac{g_Y}{2}B_\mu H\,, \tag{4.5}$$

$$D_\mu \Delta = \partial_\mu \Delta - i\frac{g_L}{2}[W_\mu^a \sigma_a, \Delta] - i g_Y B_\mu \Delta\,, \tag{4.6}$$

with $g_L$ and $g_Y$ respectively the gauge couplings for the SM gauge groups $SU(2)_L$ and $U(1)_Y$, and $\sigma_a$ ($a = 1,\ 2,\ 3$) the Pauli matrices. The most general renormalizable potential involving the scalar fields of the model is given by

$$\begin{aligned} V(H,\Delta,\Phi) = \quad & -m_H^2 + \frac{\lambda}{4}(H^\dagger H)^2 + M_\Delta^2 \mathrm{Tr}(\Delta^\dagger\Delta) + M_\Phi^2 \Phi^\dagger\Phi \\ & + \lambda_1 (H^\dagger H)\mathrm{Tr}(\Delta^\dagger\Delta) + \lambda_2[\mathrm{Tr}(\Delta^\dagger\Delta)]^2 + \lambda_3 \mathrm{Tr}[(\Delta^\dagger\Delta)^2] + \lambda_4 (H^\dagger\Delta)(\Delta^\dagger H) \\ & + \lambda_5 (\Phi^\dagger\Phi)^2 + \lambda_6 (\Phi^\dagger\Phi)(H^\dagger H) + \lambda_7 (\Phi^\dagger\Phi)\mathrm{Tr}(\Delta^\dagger\Delta) \\ & + \lambda_8 (i\Phi H^{\mathsf{T}}\sigma_2\Delta^\dagger H + \mathrm{H.c.})\,, \end{aligned} \tag{4.7}$$

where all the mass parameters $m_H^2$, $M_\Delta^2$, $M_\Phi^2$ and the quartic couplings $\lambda$ and $\lambda_i$ are assumed to be real. The scalar $\Delta$ in our model carries the same $SU(3)_C \times SU(2)_L \times U(1)_Y$ charges (**1**,**3**,1) as in the Type-II seesaw model. However, the presence of a $(B-L)$-charged $\Phi$ and the $B-L$ conservation in our model have important phenomenological consequences associated with the triplet $\Delta$, which is different from that in the Type-II seesaw scenario. In the Type-II seesaw model, the EW symmetry breaking induces a non-vanishing VEV for the triplet $\Delta$ via the cubic term $H^{\mathsf{T}} i\sigma_2 \Delta^\dagger H$. However, due to the $B-L$ conservation such a cubic term does not exist in our model, and as a result the triplet $\Delta$ does not develop a VEV in our model. As we will see in Section 4.2, this leads to very interesting signatures at the LHC and future 100 TeV colliders, which are key to distinguish our model from the Type-II seesaw.

After the EW symmetry breaking, the Higgs doublet $H$ develops a VEV $v = (\sqrt{2}G_F)^{-1/2}$ with $G_F$ being the Fermi constant, and the mass matrix of the CP-even neutral components in the $\{h, \delta^{0r}, \Phi^r\}$ basis (here $X^r$ refers to the real component of the field $X$) is

$$M^2_{\mathrm{CP-even}} = \begin{pmatrix} \frac{1}{2}\lambda v^2 & 0 & 0 \\ 0 & M_\Delta^2 + \frac{1}{2}(\lambda_1+\lambda_4)v^2 & -\frac{1}{2}\lambda_8 v^2 \\ 0 & -\frac{1}{2}\lambda_8 v^2 & M_\Phi^2 + \frac{1}{2}\lambda_6 v^2 \end{pmatrix}. \tag{4.8}$$

As the singlet and triplet scalars do not have VEVs, the component $h$ from the SM doublet $H$ does not mix with other neutral scalars, as can be seen from Eq. (4.8). Then $h$ can be readily identified as the 125 GeV Higgs boson observed at the LHC [13, 14], and the quartic coupling $\lambda$ can be identified as the SM quartic coupling. The two remaining physical CP-even scalar eigenstates are from mixing of the components $\Phi^r$ and $\delta^{0r}$ of the leptonic fields $\Phi$ and $\Delta$ with $B-L$ charge of +2, and thus are both physical leptonic scalars. Denoting $H_1$ as the lighter one and $H_2$ as the heavier one, they can be obtained by the following rotation

$$\begin{pmatrix} H_1 \\ H_2 \end{pmatrix} = \begin{pmatrix} \cos\theta & -\sin\theta \\ \sin\theta & \cos\theta \end{pmatrix} \begin{pmatrix} \Phi^r \\ \delta^{0r} \end{pmatrix} , \tag{4.9}$$

where the mixing angle $\theta$ is given by

$$\tan 2\theta = \frac{\lambda_8 v^2}{M_\Delta^2 + v^2(\lambda_1+\lambda_4-\lambda_6)/2 - M_\Phi^2} , \tag{4.10}$$

and the two eigenvalue masses are

$$\begin{aligned} M^2_{H_{1,2}} = {} & \frac{1}{2}\left(M_\Delta^2 + M_\Phi^2\right) + \frac{1}{4}(\lambda_1+\lambda_4+\lambda_6)v^2 \\ & \mp \frac{1}{4}\sqrt{\left[2M_\Delta^2 - 2M_\Phi^2 + (\lambda_1+\lambda_4-\lambda_6)v^2\right]^2 + 4\lambda_8^2 v_H^4} . \end{aligned} \tag{4.11}$$

Similarly, the two CP-odd leptonic scalars $(A_1, A_2)$ from the imaginary components $\Phi^i, \delta^{0i}$ have exactly the same masses as the CP-even scalars, *i.e.*

$$M_{A_1} = M_{H_1} , \quad M_{A_2} = M_{H_2} . \tag{4.12}$$

For the sake of illustration, we choose to work in the regime where the leptonic scalars $(A_1, H_1)$ are in the mass range $M_h/2 < M_{H_1,A_1} \lesssim \mathcal{O}(100)$ GeV. The lower mass bound is to avoid the invisible decay of the SM Higgs $h \to H_1 H_1,\ A_1 A_1 \to \nu\nu\bar{\nu}\bar{\nu}$, while the upper bound is mainly motivated from our previous collider study [118], where the sensitivity in the vector boson fusion (VBF) channel was found to drop exponentially beyond 100 GeV or so. Since setting $\lambda_6 = 0$ gives us more freedom in the choices of other parameters while keeping leptonic scalars $(A_1, H_1)$ light and not damaging the main purpose of the study, we choose this simplest scenario for our numerical simulation. There is also a pair of heavy leptonic scalars $H_2$ and $A_2$, which can either decay into neutrinos or cascade decay into gauge bosons

and lighter scalars. For simplicity, we just assume $(H_2, A_2)$ to be heavier than the EW scale such that they are not relevant for our consideration here, and a detailed collider study of their phenomenology is deferred to future work. Finally, it is trivial to get the masses of the singly- and doubly-charged scalars, which are respectively given by

$$M^2_{H^\pm} = M^2_\Delta + \frac{1}{4}(2\lambda_1 + \lambda_4)v^2\,, \tag{4.13}$$

$$M^2_{H^{\pm\pm}} = M^2_\Delta + \frac{1}{2}\lambda_1 v^2\,. \tag{4.14}$$

Depending on the sign of $\lambda_4$, $H^\pm$ can be lighter or heavier than $H^{\pm\pm}$.

### 4.1.1 Key parameters and decay channels of $H^{\pm\pm}$ and $H^\pm$

The interactions of the new scalars with the SM fields are generated through the gauge couplings in Eqs. (4.5) and (4.6), the scalar couplings in Eq. (4.7) and the Yukawa interactions in Eq. (4.3) including potential scalar mixing in Eq. (4.9). All the key interactions of the neutral scalars $H_1$, $A_1$, the singly-charged scalar $H^\pm$ and the doubly-charged scalar $H^{\pm\pm}$ for the hadron collider analysis below are collected in Table 6. For the sake of completeness, we have listed the complete set of Feynman rules in Tables 12 to 16 in Appendix A.

The gauge interactions of $H^\pm$ and $H^{\pm\pm}$ with the SM photon, $W$ and $Z$ bosons in Table 6 are relevant for the pair production $H^{++}H^{--}$ and the associated production $H^{\pm\pm}H^\mp$ of the doubly-charged scalar at hadron colliders, as in the Type-II seesaw case [139, 140, 141, 142, 143, 144, 145, 146, 147, 148, 149, 150, 151, 152, 153, 154, 155, 156, 157].

The remaining couplings in Table 6 are relevant to the decays of $H^\pm$ and $H^{\pm\pm}$. For the singly-charged scalar $H^\pm$, besides the leptonic final states, it can decay into a light neutral scalar $H_1$ or $A_1$ and a $W$ boson, which is absent in the Type-II seesaw model. The corresponding partial decay widths are respectively

$$\Gamma(H^\pm \to \ell^\pm_\alpha v_\beta) \;=\; \frac{Y^2_{\alpha\beta} M_{H^\pm}}{8\pi}\,, \tag{4.15}$$

$$\Gamma(H^\pm \to W^\pm H_1) \;=\; \Gamma(H^\pm \to W^\pm A_1) \;=\; \frac{G_F \sin^2\theta M^3_{H^\pm}}{4\sqrt{2}\pi}\lambda^{3/2}\left(\frac{M^2_W}{M^2_{H^\pm}}, \frac{M^2_{H_1}}{M^2_{H^\pm}}\right)\,, \tag{4.16}$$

where the function

$$\lambda(x,y) \;\equiv\; 1 + x^2 + y^2 - 2xy - 2x - 2y\,. \tag{4.17}$$

Table 6: Important couplings for the neutral scalars $H_1$, $A_1$, the singly-charged scalar $H^\pm$ and the doubly-charged scalar $H^{\pm\pm}$. Here $e$ is the electric charge, $s_W \equiv \sin\theta_W$ and $c_W \equiv \cos\theta_W$ the sine and cosine of the Weinberg angle $\theta_W$, $p_{1,2}$ the momenta for the first and second particles in the vertices, and $P_L = \frac{1}{2}(1-\gamma_5)$ the left-handed projection operator. See Appendix. A for the full set of Feynman rules.

| Vertices | Couplings |
|---|---|
| $H_1\nu_\alpha\nu_\beta$ | $-i\sqrt{2}Y_{\alpha\beta}\sin\theta\, P_L$ |
| $A_1\nu_\alpha\nu_\beta$ | $\sqrt{2}Y_{\alpha\beta}\sin\theta\, P_L$ |
| $H^+H^-\gamma_\mu$ | $i\,e(p_1-p_2)_\mu$ |
| $H^+H^-Z_\mu$ | $-i\,e\frac{s_W}{c_W}(p_1-p_2)_\mu$ |
| $H^+\ell^-_\alpha\nu_\beta$ | $\sqrt{2}i\,Y_{\alpha\beta}\,P_L$ |
| $H^+H_1W^-_\mu$ | $i\frac{g_L}{\sqrt{2}}\,(p_1-p_2)_\mu\,\sin\theta$ |
| $H^+A_1W^-_\mu$ | $\frac{g_L}{\sqrt{2}}\,(p_1-p_2)_\mu\,\sin\theta$ |
| $H^{++}H^{--}\gamma_\mu$ | $2i\,e(p_1-p_2)_\mu$ |
| $H^{++}H^{--}Z_\mu$ | $i\,e\frac{c_W^2-s_W^2}{c_W s_W}(p_1-p_2)_\mu$ |
| $H^{++}\ell^-_\alpha\ell^-_\beta$ | $2i\,Y_{\alpha\beta}\,P_L$ |
| $H^{++}H^-W^-_\mu$ | $-ig_L\,(p_1-p_2)_\mu$ |
| $H^{++}W^-_\mu W^-_\nu H_1$ | $-i\sqrt{2}g_L^2\,\sin\theta\, g_{\mu\nu}$ |
| $H^{++}W^-_\mu W^-_\nu A_1$ | $-\sqrt{2}g_L^2\,\sin\theta\, g_{\mu\nu}$ |

As in the standard Type-II seesaw, the singly-charged scalar $H^\pm$ can decay into a heavy scalar $H_2$ or $A_2$ and a $W$ boson. However, the mass splitting between the triplet scalar components is severely constrained by the EW precision data (EWPT), in terms of the oblique $S$ and $T$ parameters [158, 159]: depending on the triplet scalar masses, it is required that the mass splitting $\Delta M \lesssim 50$ GeV [145, 160, 161, 154]. Therefore the $W$ boson is always off-shell, *i.e.* $H^\pm \to W^{\pm *}H_2$, $W^{\pm *}A_2$ (the corresponding interaction can be found in

Table 14), and the corresponding widths are given by

$$\Gamma(H^\pm \to W^{\pm *} H_2) \;=\; \Gamma(H^\pm \to W^{\pm *} A_2) \;=\; \frac{9 g_L^4 \cos^2\theta M_{H^\pm}}{256\pi^3} G\left(\frac{M_{H_2}^2}{M_{H^\pm}^2}, \frac{M_W^2}{M_{H^\pm}^2}\right), \quad (4.18)$$

where the function $G(x,y)$ is explicitly given in Appendix B. Although this channel does not suffer suppression from mixing angle, the off-shellness of the decaying gauge boson leads to a high suppression from $G(x,y)$ function making its contribution negligible compared to other decay channels.

In our model, the doubly-charged scalar $H^{\pm\pm}$ can decay into same-sign dilepton pairs and the three-body final state $W^\pm W^\pm H_1$ and $W^\pm W^\pm A_1$. The partial widths are given respectively by

$$\Gamma(H^{\pm\pm} \to \ell_\alpha^\pm \ell_\beta^\pm) \;=\; \frac{S_{\alpha\beta} Y_{\alpha\beta}^2 M_{H^{\pm\pm}}}{4\pi}\,, \quad (4.19)$$

$$\Gamma(H^{\pm\pm} \to W^\pm W^\pm H_1) \;=\; \Gamma(H^{\pm\pm} \to W^\pm W^\pm A_1) = \frac{g_L^4 \sin^2\theta}{512\pi^3 M_{H^{\pm\pm}}^3} \int \mathcal{F} dm_{12}^2 dm_{23}^2\,, \quad (4.20)$$

where $S_{\alpha\beta} = 1/2$ (1) for $\alpha \neq \beta$ ($\alpha = \beta$) is a symmetry factor, and the dimensionless lengthy function $\mathcal{F}$ is put in Appendix B, which is a function of $m_{12}^2$ and $m_{23}^2$. The phase space is integrated over the allowed ranges of $m_{12}^2$ and $m_{23}^2$ according to Dalitz plot. There is also a two-body bosonic channel, the partial width is

$$\Gamma(H^{\pm\pm} \to W^{\pm *} H^\pm) = \frac{9 g_L^4 M_{H^{\pm\pm}}}{128\pi^3} G\left(\frac{M_{H^+}^2}{M_{H^{\pm\pm}}^2}, \frac{M_W^2}{M_{H^{\pm\pm}}^2}\right). \quad (4.21)$$

with the function $G(x,y)$ defined in Appendix B. As for the singly-charged scalar in Eq. (4.18), this channel is highly suppressed by the off-shell $W$ boson, and will be neglected in the following analysis. Since the masses and decay properties of $H_1$ and $A_1$ are the same in our model, we henceforth collectively use $\phi$ to denote both the leptonic scalars $H_1$ and $A_1$, *i.e.* $\phi = H_1,\, A_1$.

In the standard Type-II seesaw, there is also the cascade decay channel for the doubly-charged scalar [142, 145]:

$$H^{\pm\pm} \to H^\pm W^{\pm *} \to H_2 W^{\pm *} W^{\pm *}\,. \quad (4.22)$$

In a large region of parameter space, the dilepton channels $H^{\pm\pm} \to \ell^\pm \ell^\pm$ and diboson channel $H^{\pm\pm} \to W^\pm W^\pm$ are highly suppressed respectively by the small Yukawa couplings $Y_{\alpha\beta}$ and

the small VEV $v_\Delta$ of the triplet, and the doubly-charged scalar $H^{\pm\pm}$ decays mostly via the cascade channel above. When the mixing of $H_2$ with the SM Higgs is small, the neutral scalar $H_2$ decays mostly further into neutrinos via the Yukawa coupling $Y_{\alpha\beta}$. If the cascade channel dominates, the current direct LHC constraints on $M_{H^{\pm\pm}}$ in the $\ell^\pm\ell^\pm$ [11, 162] and $W^\pm W^\pm$ [163, 10] channels will be largely weakened. Then a relatively light $H^{\pm\pm}$ implies that the neutral scalar $H_2$ may also be light. This makes the decay channel of (4.22) in the standard Type-II seesaw to some extent similar to our case in Eq. (4.20), both leading to the signal of same-sign dilepton plus missing transverse energy (assuming $W$ boson decaying leptonically). However, as a result of the severe EWPT constraint on the mass splitting $\Delta M$ of the triplet scalars [145, 160, 161, 154], the two $W$ bosons are both off-shell in the cascade decay in Eq. (4.22), which is very different from the on-shell $W$ bosons in Eq (4.20) in our case.

Similarly, in the standard Type-II seesaw model the singly-charged scalar $H^\pm$ can decay into $\ell^\pm\nu$ and $hW^\pm$, $ZW^\pm$, $t\bar{b}$, which are respectively proportional to the couplings $Y_{\alpha\beta}$ and $v_\Delta$ [142]. When both $Y_{\alpha\beta}$ and $v_\Delta$ are relatively small, the decay of $H^\pm$ will be dominated by

$$H^\pm \to H_2 W^{\pm *}\,, \tag{4.23}$$

where the $W$ boson is again off-shell as a result of the EWPT limit on the triplet scalar mass splitting. As in the doubly-charged scalar case, the decay $H^\pm \to H_2 W^{\pm *}$ with a light $H_2$ in the Type-II seesaw is very similar to the channel $H^\pm \to W^\pm \phi$ in our model, except for the off-shell $W$ boson.

Therefore, the new decay channels $H^{\pm\pm} \to W^\pm W^\pm \phi$ and $H^\pm \to W^\pm \phi$ make our model very different from the standard Type-II seesaw in the following aspects, which can be used to distinguish the two models at the high-energy colliders:

- The $W^\pm W^\pm \phi$ final state from the $H^{\pm\pm}$ decay is absent in the standard Type-II seesaw model, where the $W$ bosons in the decays in Eqs. (4.20) and (4.23) are off-shell.
- Another distinguishing feature of this model is that the decays $H^{\pm\pm} \to W^\pm W^\pm \phi$ and $H^\pm \to W^\pm \phi$ does not necessarily correspond to the compressed mass gaps among different particle states of the triplet $\Delta$, whereas in the standard Type-II seesaw model the

decays in Eqs. (4.20) and (4.23) are very sensitive to the mass splitting $\Delta M$ of the triplet scalars.

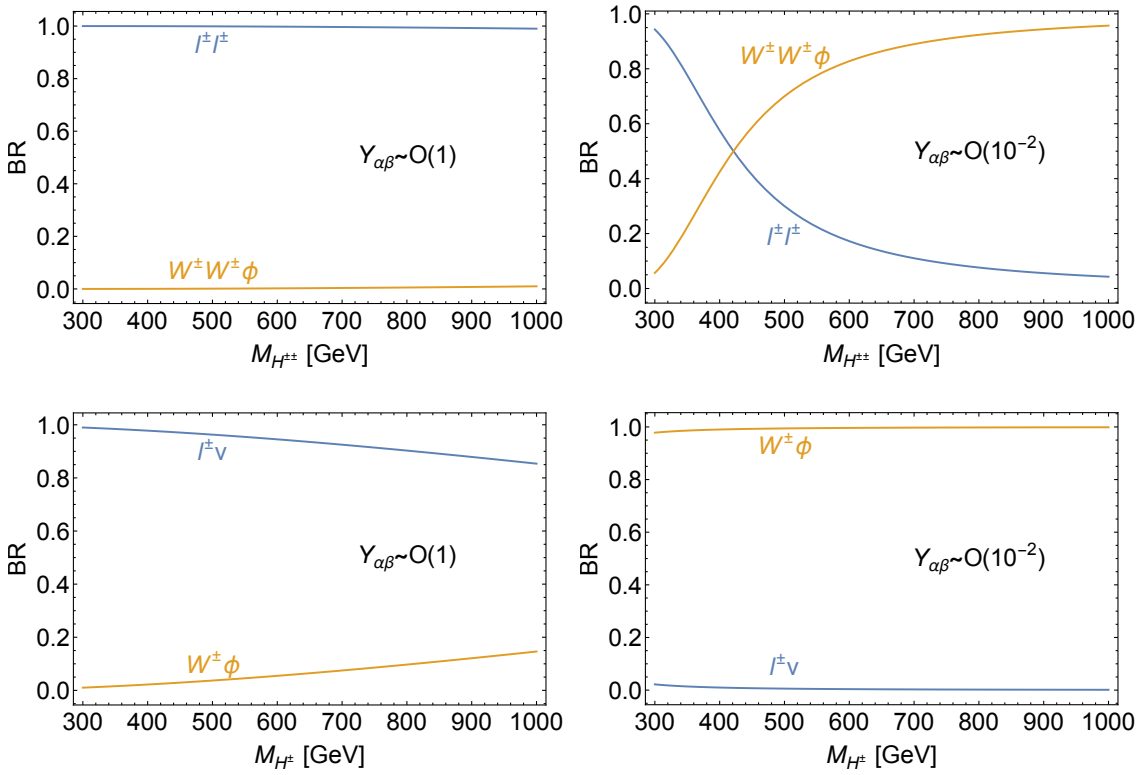


Figure 17: Branching fractions of $H^{\pm\pm}$ decay (upper panels) and $H^{\pm}$ decay (lower panels) as a function of their masses. The left and right panels are for the large and small Yukawa coupling scenarios, respectively. Here $\phi$ denotes a leptonic scalar $H_1/A_1$.

Depending on the value of the Yukawa couplings $Y_{\alpha\beta}$, there are two distinct scenarios for the decays of $H^{\pm\pm}$ and $H^{\pm}$:

- Large Yukawa coupling scenario with $Y_{\alpha\beta} \sim \mathcal{O}(1)$. In this case the leptonic channels $H^{\pm\pm} \to \ell^{\pm}\ell^{\pm}$ and $H^{\pm} \to \ell^{\pm}\nu$ dominate, which are from the Yukawa interactions $Y_{\alpha\beta}$.
- Small Yukawa coupling scenario with $Y_{\alpha\beta} \lesssim \mathcal{O}(10^{-2})$. In this case the bosonic channels $H^{\pm\pm} \to W^{\pm}W^{\pm}\phi$ and $H^{\pm} \to W^{\pm}\phi$ dominate, which originate from the gauge couplings in Eqs. (4.5) and (4.6).

For simplicity, we will not consider the intermediate scenarios, where the branching fractions (BRs) of bosonic and fermionic decay channels above are comparable. The $W$-dominated

final states for small Yukawa couplings $Y_{\alpha\beta}$ depend on the scalar mixing angle $\sin\theta$, which in turn depends on $\lambda_8$ as shown in Eq. (4.10), where we find that $\lambda_8$ needs to be $\mathcal{O}(1)$ in order to have a sizable $\sin\theta$. The decay branching fractions of $H^{\pm\pm}$ and $H^{\pm}$ are shown respectively in the upper and lower panels of Fig. 17 as a function of their masses. The left and right panels are respectively for the large and small Yukawa coupling scenarios. As shown in the bottom left panel, if the Yukawa couplings are of order one, the dominant decay channels of $H^{\pm}$ will be $\ell^{\pm}\nu$, but the bosonic channel $W^{\pm}\phi$ is still feasible in the high mass regime with a branching fraction around 10%. For small Yukawa couplings of order $\mathcal{O}(10^{-2})$, the singly-charged scalar $H^{\pm}$ decays predominantly into $W^{\pm}\phi$, as demonstrated in the bottom right panel. On the other hand, as shown in the top left panel, the doubly-charged scalar $H^{\pm\pm}$ will decay mostly to $\ell^{\pm}\ell^{\pm}$ if the Yukawa couplings are large, while the $W^{\pm}W^{\pm}\phi$ channel is dominant for small Yukawa couplings although a crossover happens for low $M_{H^{\pm\pm}}$, as shown in the top right panel.

### 4.1.2 LFV constraints

There exist numerous constraints on the charged Higgs sector from the low-energy flavor data, such as those from the LFV decays $\ell_\alpha \to \ell_\beta \ell_\gamma \ell_\delta$, $\ell_\alpha \to \ell_\beta \gamma$ [3, 4], anomalous electron [5] and muon [6, 7] magnetic moments, muonium oscillation [8], and the LEP $e^+e^- \to \ell^+\ell^-$ data [9]. Following Ref. [151], the updated LFV limits on the Yukawa couplings $Y_{\alpha\beta}$ are collected in Table 7, and the most stringent ones are shown in Fig. 18, as a function of the doubly-charged scalar mass $M_{H^{\pm\pm}}$. We see that the products involving two flavor transitions are highly constrained, while the bounds on an individual coupling are much weaker, especially for the tau flavor.

It should be noted that the contributions of $H^{\pm\pm}$ to the electron and muon $g-2$ are always negative [164]. Therefore, the recent measurement of muon $g-2$ at Fermilab [7] cannot be interpreted as the effect of $H^{\pm\pm}$ in our model. On the other hand, we can use the reported measurement of Ref. [7]

$$\Delta a_\mu = a_\mu^{\rm exp} - a_\mu^{\rm SM} = (251 \pm 59) \times 10^{-11}\,, \tag{4.24}$$

which is $4.2\sigma$ larger than the SM prediction [165], to set limits on the $H^{\pm\pm}$ parameter space. We will use a conservative $5\sigma$ bound, *i.e.* require that the magnitude of the new contribution to $(g-2)_\mu$ from $H^{\pm\pm}$ must not exceed $0.8 \times 59 \times 10^{-11}$. The corresponding limit on the Yukawa coupling $Y_{\mu\beta}$ is shown by the purple shaded region in Fig. 18 and also in Table 7. Note that if a light scalar has an LFV coupling $h_{\mu\tau}$ to muon and tau, it could be a viable candidate to explain the muon $g-2$ anomaly, while satisfying all current constraints [166, 167, 168, 169, 170, 171, 172]. Such neutral scalar interpretations of muon $g-2$ anomaly can be definitively tested at a future muon collider [173, 174, 175, 176, 177].

Table 7: Upper limits on the Yukawa couplings $|Y_{\alpha\beta}|^2$ (or $|Y^\dagger_{\alpha\gamma}Y_{\beta\gamma}|$) from the current experimental limits on the LFV branching fractions of $\ell_\alpha \to \ell_\beta\ell_\gamma\ell_\delta$, $\ell_\alpha \to \ell_\beta\gamma$ [3, 4], anomalous electron [5] and muon [6, 7] magnetic moments, muonium oscillation [8], and LEP $e^+e^- \to \ell^+\ell^-$ data [9]. See also Fig. 18.

| Process | Experimental bound | Constraint $\times \left(\frac{M_{H^{\pm\pm}}}{100\,\mathrm{GeV}}\right)^2$ |
|---|---|---|
| $\mu^- \to e^-e^+e^-$ | $< 1.0 \times 10^{-12}$ | $\lvert Y^\dagger_{ee}Y_{e\mu}\rvert < 2.3 \times 10^{-7}$ |
| $\tau^- \to e^-e^+e^-$ | $< 1.4 \times 10^{-8}$ | $\lvert Y^\dagger_{ee}Y_{e\tau}\rvert < 6.5 \times 10^{-5}$ |
| $\tau^- \to e^-\mu^+\mu^-$ | $< 1.6 \times 10^{-8}$ | $\lvert Y^\dagger_{e\mu}Y_{\mu\tau}\rvert < 4.9 \times 10^{-5}$ |
| $\tau^- \to \mu^-e^+\mu^-$ | $< 9.8 \times 10^{-9}$ | $\lvert Y^\dagger_{e\tau}Y_{\mu\mu}\rvert < 5.5 \times 10^{-5}$ |
| $\tau^- \to \mu^-e^+e^-$ | $< 1.1 \times 10^{-8}$ | $\lvert Y^\dagger_{e\mu}Y_{e\tau}\rvert < 4.1 \times 10^{-5}$ |
| $\tau^- \to e^-\mu^+e^-$ | $< 8.4 \times 10^{-9}$ | $\lvert Y^\dagger_{ee}Y_{\mu\tau}\rvert < 5.1 \times 10^{-5}$ |
| $\tau^- \to \mu^-\mu^+\mu^-$ | $< 1.2 \times 10^{-8}$ | $\lvert Y^\dagger_{\mu\mu}Y_{\mu\tau}\rvert < 6.1 \times 10^{-5}$ |
| $\mu^- \to e^-\gamma$ | $< 4.2 \times 10^{-13}$ | $\lvert\sum_\gamma Y^\dagger_{e\gamma}Y_{\mu\gamma}\rvert < 2.7 \times 10^{-6}$ |
| $\tau^- \to e^-\gamma$ | $< 3.3 \times 10^{-8}$ | $\lvert\sum_\gamma Y^\dagger_{e\gamma}Y_{\tau\gamma}\rvert < 1.8 \times 10^{-3}$ |
| $\tau^- \to \mu^-\gamma$ | $< 4.4 \times 10^{-8}$ | $\lvert\sum_\gamma Y^\dagger_{\mu\gamma}Y_{\tau\gamma}\rvert < 2.1 \times 10^{-3}$ |
| electron $g-2$ | $< 5.2 \times 10^{-13}$ | $\sum_\beta \lvert Y_{e\beta}\rvert^2 < 1.2$ |
| muon $g-2$ | $< 4.7 \times 10^{-10}$ | $\sum_\beta \lvert Y_{\mu\beta}\rvert^2 < 0.025$ |
| muonium oscillation | $< 8.2 \times 10^{-11}$ | $\lvert Y^\dagger_{ee}Y_{\mu\mu}\rvert < 0.0012$ |
| $e^+e^- \to e^+e^-$ | $\Lambda_{\rm eff} > 5.2$ TeV | $\lvert Y_{ee}\rvert^2 < 0.0012$ |
| $e^+e^- \to \mu^+\mu^-$ | $\Lambda_{\rm eff} > 7.0$ TeV | $\lvert Y_{e\mu}\rvert^2 < 6.4 \times 10^{-4}$ |
| $e^+e^- \to \tau^+\tau^-$ | $\Lambda_{\rm eff} > 7.6$ TeV | $\lvert Y_{e\tau}\rvert^2 < 5.4 \times 10^{-4}$ |

The doubly-charged scalar $H^{\pm\pm}$ can induce leptonic decays of SM $Z$ and Higgs boson at 1-

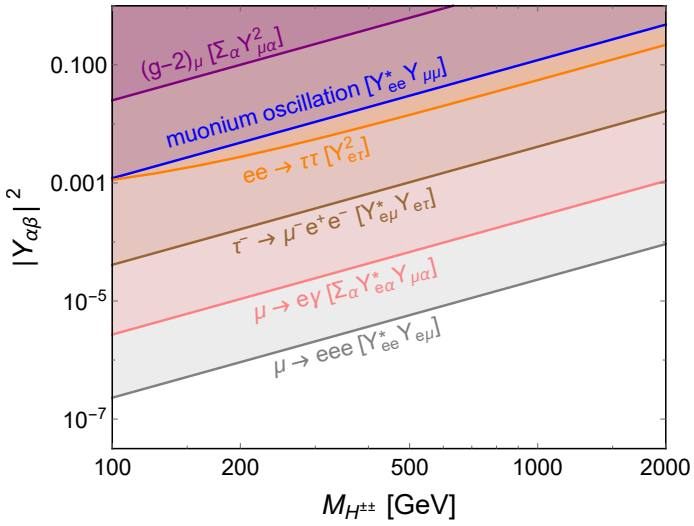


Figure 18: LFV limits on the Yukawa couplings $|Y_{\alpha\beta}|^2$ as a function of the doubly-charged scalar mass $M_{H^{\pm\pm}}$. The shaded regions are excluded. See text and Table 7 for more details.

loop level. With the coupling $Y_{\alpha\beta}$, the corresponding partial withs are respectively [178, 179]

$$\Gamma(Z \to \ell_\alpha^+ \ell_\beta^-) \simeq \frac{g_L^2 M_Z}{144\pi^4} \left(\frac{\cos 2\theta_w}{\cos\theta_w}\right)^2 \left|\frac{\sum_\gamma m_{\ell_\gamma}^2 Y_{\alpha\gamma} Y_{\gamma\beta}^*}{M_{H^{\pm\pm}}^2}\right|^2 , \tag{4.25}$$

$$\Gamma(h \to \ell_\alpha^+ \ell_\beta^-) \simeq \frac{M_h (\lambda_1 v)^2}{2^{15}\pi^5} \left|\frac{\sum_\gamma m_{\ell_\gamma} Y_{\alpha\gamma} Y_{\gamma\beta}^*}{M_{H^{\pm\pm}}^2}\right|^2 \left|F\left(\frac{4M_{H^{\pm\pm}}^2}{M_h^2}\right)\right|^2 , \tag{4.26}$$

where $M_Z$ is the $Z$ boson mass, $m_{\ell_\gamma}$ is the mass for the charged lepton $\ell_\gamma$, the factor of $\lambda_1 v$ in Eq. (4.26) is from the trilinear scalar coupling $hH^{++}H^{--}$ in Table 12, and the loop function $F(x)$ can be found in Eq. (B.8) of Ref. [179]. For the case of $\alpha \neq \beta$, the $H^{\pm\pm}$ induced decays in Eqs. (4.25) and (4.26) are apparently LFV. However, in addition to the loop factor, both the (LFV) decays of SM Higgs and $Z$ bosons above are highly suppressed by powers of the small ratio $m_{\ell_\gamma}/M_{h,Z}$. It turns out that the current precision $Z$ and Higgs data [3] can only exclude $|Y_{\alpha\beta}|^2 \gg 1$ for $M_{H^{\pm\pm}} = 1$ TeV, and the corresponding limits are much weaker than those in Table 7 and Fig. 18.

Similarly, given the coupling $Y_{\alpha\beta}$, the couplings of the leptonic scalar $\phi$ with neutrinos induce the tree-level invisible decays $Z \to \nu_\alpha \nu_\beta \phi$, $h \to \nu_\alpha \nu_\beta \phi$ and the leptonic decay $W \to$

$\ell_\alpha \nu_\beta \phi$. However, the limits from current precision EW and Higgs data are at most $Y_{\alpha\beta} \gtrsim \mathcal{O}(1)$ [117, 118], and therefore, are not shown in Table 7 and Fig. 18.

### 4.1.3 High-energy behavior: perturbativity and unitarity limits

Since larger values of $\lambda_8$ and $Y_{\alpha\beta}$ play important roles for the hadron collider signal of this model, let us first check the largest values of these couplings which can be accommodated at the EW scale without becoming non-perturbative at a higher energy scale. For the purpose of illustration, we set just one Yukawa coupling $Y_{\mu\mu}$ to be non-vanishing, with all other Yukawa couplings $Y_{\alpha\beta}$ ($\alpha\beta \neq \mu\mu$) to be zero. This choice is compatible with the current limits in Table 7, as the products of the Yukawa couplings must be small due to the existing LFV limits, while a single coupling ($Y_{\mu\mu}$ in our case) can be as large as $Y_{\mu\mu} \sim \mathcal{O}(1)$ for $M_{H^{\pm\pm}} \sim 1$ TeV.

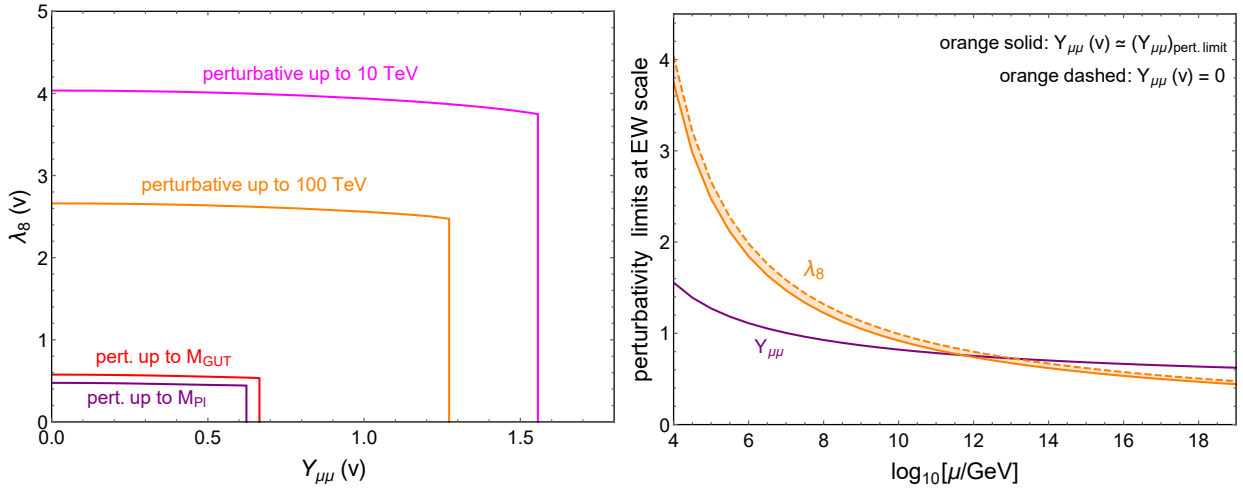


Figure 19: *Left panel*: Perturbativity limits on $\lambda_8(v)$ by the Landau pole at a higher scale of 10 TeV (magenta), 100 TeV (orange), the GUT scale (red) and the Planck scale (purple), as function of $Y_{\mu\mu}(v)$. *Right panel*: Perturbativity limits on $\lambda_8$ (orange) and $Y_{\mu\mu}$ (purple) at the EW scale, as function of the Landau pole scale $\mu$. For the solid and dashed orange lines, we take $Y_{\mu\mu}$ to be respectively the perturbativity limit and zero at the EW scale.

To implement the perturbativity limits from the high-energy scale, we use the RGEs in Appendix C for all the gauge, scalar and Yukawa couplings given in Eqs. (4.5), (4.6), (4.3)

and (4.7). From the RGEs, we find that $\lambda_8$ depends on $Y_{\mu\mu}$ at one-loop level, since both $\lambda_8$ and $Y_{\mu\mu}$ are associated with the interaction terms which involve the triplet scalars. The dependence of perturbativity limits on $\lambda_8$ on the Yukawa coupling $Y_{\mu\mu}(v)$ at the EW scale is shown in the left panel of Fig. 19, with perturbativity up to Planck scale $M_{\rm Pl}$ and the grand unified theory (GUT) scale $M_{\rm GUT}$ for the purple and red lines, and up to the 100 TeV and 10 TeV scales for the orange and pink lines, respectively. Comparing these lines, we can see that the perturbativity limits on $\lambda_8$ are very sensitive to the value of $Y_{\mu\mu}$ at the EW scale. To have a perturbative $\lambda_8$ at the 10 TeV (100 TeV) scale, it is required that the coupling $Y_{\mu\mu}(v) \lesssim 1.6$ (1.3). For a perturbative theory up to the GUT or Planck scale, the coupling $Y_{\mu\mu}$ needs to be even smaller, *i.e.* $Y_{\mu\mu}(v) \lesssim 0.67$. The perturbativity limits on $\lambda_8$ and $Y_{\mu\mu}$ at the EW scale as function of the scale 10 TeV $< \mu <$ $M_{\rm Pl}$ are shown in the right panel of Fig. 19. For the quartic coupling $\lambda_8$, the solid and dashed lines correspond respectively to the cases of $Y_{\mu\mu}$ set at the perturbative limit and $Y_{\mu\mu} = 0$ at the EW scale. As shown in both the two panels of Fig. 18, the quartic coupling $\lambda_8$ can be as large as 4 (2.7), with perturbativity holding up to 10 TeV (100 TeV). With the requirement of perturbativity up to the Planck (GUT) scale, we have $\lambda_8 \lesssim 0.48$ (0.58) at the EW scale.

The high-energy behavior of $\lambda_8$, $Y_{\mu\mu}$ and other couplings can be understood analytically from the solutions of RGEs for these couplings. As a rough approximation, let us first see the analytical solution of $Y_{\mu\mu}$ without including the contributions from the gauge couplings $g_{S,\,L,\,Y}$ for the $SU(3)_C, SU(2)_L, U(1)_Y$ respectively. Defining $\alpha_\mu \equiv Y_{\mu\mu}^2/4\pi$, it is trivial to get the analytical solution of $\alpha_\mu$ at scale $\mu$ from Eq. ( C.14) as

$$\alpha_\mu(\mu) = \frac{\alpha_\mu(v)}{1 - \frac{4}{\pi}\alpha_\mu(v) t}\,, \quad \text{with} \quad t = \ln\frac{\mu}{v}\,. \tag{4.27}$$

It is clear from the above equation that the coupling $Y_{\mu\mu}$ is not asymptotically free and will blow up when the scale parameter approaches the value of

$$t_c = \ln\left(\frac{\mu_c}{v}\right) = \frac{\pi^2}{Y_{\mu\mu}^2(v)}\,. \tag{4.28}$$

With an initial value of $Y_{\mu\mu}(v) = 1.5$ at the EW scale, we can get the critical value of $t_c \simeq 4.39$, which corresponds to an energy scale of $\mu \simeq 20$ TeV. The full analytic solution of $Y_{\mu\mu}$ including the gauge coupling contributions is shown in Appendix D. Following the running of

gauge couplings, and taking $g_L(M_Z) = 0.65100$, $g_Y(M_Z) = 0.357254$ [180, 181, 182, 183, 184], we find that in this case $t_c = 4.67$, which corresponds to $\mu \simeq 26$ TeV.

The contribution of $Y_{\mu\mu}$ to the evolution of $\lambda_8$ can be obtained from the following analytical solution of the RGE for $\lambda_8$ (see Appendix D for more details)

$$\lambda_8(\mu) = \lambda_8(v) \exp\left[\frac{1}{4\pi^2}\int_v^\mu E_8(\mu) d\mu\right], \tag{4.29}$$

where $E_8$ depends on $Y_{\mu\mu}$ as well as the couplings $g_{L,Y}$ and the top-quark Yukawa coupling $y_t$ and is given in Eq. ( D.12). As soon as $Y_{\mu\mu}$ turns non-perturbative, the exponential becomes very large and $\lambda_8$ also becomes non-perturbative.

We have also checked the unitarity constraints on $Y_{\mu\mu}$ and $\lambda_8$, and the details are given in Appendix E. It is found that the unitarity constraints are much weaker $\lambda_8 < 10.0$, compared to the perturbativity constraints obtained here.

### 4.2 Collider signatures

In this section we analyze the striking signatures of this model at the LHC and future 100 TeV hadron colliders. The model parameters adopted have been cooperated with low engery & high energy constraints we studied as well as the current experimental limit. We consider both the pair production and the associated production channels:

$$pp \to H^{++}H^{--},\ H^{\pm\pm}H^{\mp}\,. \tag{4.30}$$

The production cross sections in the two channels for the doubly-charged scalar coming from an $SU(2)_L$-triplet $\Delta$ at the 14 TeV LHC and future 100 TeV colliders have been estimated in Refs. [152, 185], which are reproduced in Fig. 20. As shown in Section 4.1.1, the final states associated with these production processes depend on the decay branching fractions of $H^{\pm\pm}$ and $H^{\pm}$. Our model predicts novel decay processes

$$H^{\pm\pm} \to W^{\pm}W^{\pm}\phi \quad \text{and} \quad H^{\mp} \to W^{\mp}\phi\,, \tag{4.31}$$

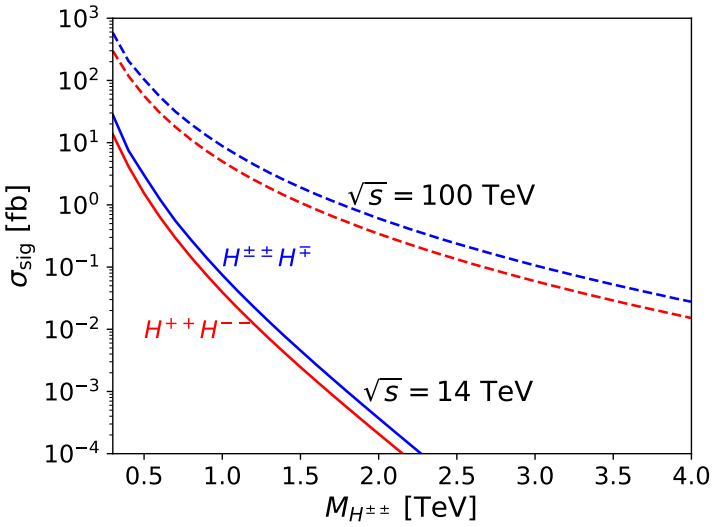


Figure 20: Cross sections of $H^{++}H^{--}$ pair (red) and $H^{\pm\pm}H^{\pm}$ associated (blue) production of doubly-charged scalars at $\sqrt{s} = 14$ TeV (solid) and $\sqrt{s} = 100$ TeV (dashed) $pp$ colliders.

where the light leptonic scalars $\phi = H_1,\ A_1$ will escape from detection and lead to missing momentum. This can be used to distinguish our model from the standard Type-II seesaw. In this paper, we will focus on these novel channels. The prospects of the small Yukawa coupling scenario at future hadron colliders are investigated in Section 4.2.1, the large Yukawa coupling case is analyzed in Section 4.2.2, and the intermediate Yukawa coupling case is considered in Section 4.2.3.

### 4.2.1 Small Yukawa coupling scenario

One typical choice of parameter is that the Yukawa coupling $Y_{\alpha\beta} \lesssim 10^{-2}$ to satisfy all the low-energy experimental limits in Section 4.1.2. Note that this choice of $Y_{\alpha\beta}$ would result in an effective $\nu_\alpha \nu_\beta \phi$ coupling $\lambda_{\alpha\beta}$ of order $10^{-3}$, which is too small to probe in the VBF channel discussed in Ref. [118], but accessible in our UV-complete model due to the additional interactions, as shown below. In particular, under this choice of small Yukawa coupling, the doubly-charged scalar $H^{\pm\pm}$ will mostly decay to two $W$ bosons and a light

neutral leptonic scalar $\phi = H_1, A_1$; cf. the top right panel of Fig. 17. With two same-sign $W$ bosons decaying leptonically and the other two decaying hadronically, the final state of our signal features two same-sign leptons ($e$ or $\mu$) plus jets and large missing transverse momentum in the pair production channel, *i.e.*

$$pp \to H^{++}(\to W^+W^+\phi)\, H^{--}(\to W^-W^-\phi) \to \ell^\pm\ell^\pm + 4 \text{ jets} + E_T^{\rm miss}\,.$$

Similarly, we also have the associated production $pp \to H^{\pm\pm}H^\mp$ with $H^\mp \to W^\mp\phi$ which also has the same final states. However, due to the presence of less number of $W$'s, the contribution from the associated production is small to our signal.

We use `FeynRules` [74] to define the fields and the Lagrangian of our model, then the resulting UFO model file is fed into `MadGraph5_aMC@NLO` [47] to generate the Monte Carlo events where the decay of vector bosons is achieved by the `Madspin` [51] module integrated within `MadGraph5`. Next-to-leading order corrections are included by a $k$-factor of 1.25 [186] for our signal process. The leading SM backgrounds come from $WZ$ and $WW$ productions and the sub-leading ones from $WWW$ and $t\bar{t}W$ processes are also considered. We use `MadGraph5` to generate the background events, and the leading ones are generated with two extra jets to properly account for the jet multiplicity in the final states. The events from the hard processes are showered with `Pythia8` [187] and the jets are clustered using `Fastjet` [106] with the anti-$k_T$ algorithm [188] and the cone radius $\Delta R = 0.4$. All the signal and background events are smeared to simulate the detector effect by our own code using `Delphes CMS_PhaseII` cards [189].

Electrons (muons) are selected by requiring that $p_T > 10\,\text{GeV}$ and $|\eta| < 2.47$ (2.5), jets are required to have $p_T > 20\,\text{GeV}$ and $|\eta| < 3$. We adopt the $b$-tagging formula from the `Delphes` default card where the efficiency is $\varepsilon_b = 0.8\tanh\left(0.003 p_T^{b\text{-jet}}\right) \times 30/(1 + 0.086 p_T^{b\text{-jet}})$ (with $p_T^{b\text{-jet}}$ in unit of GeV) [189]. We apply some pre-selection cuts before launching the carefully designed analysis below. First, all events should have exactly two same-sign leptons and the number of jets should be at least 3: $N_{\rm jet} \geq 3$. Finally we veto any event with $b$-tagged jet: $N_{b\text{-jet}} = 0$.

**4.2.1.1 Cut-based analysis** The same-sign $W$ pair signal from $H^{\pm\pm} \to W^{\pm}W^{\pm}$ has been searched for at the LHC by the ATLAS collaboration [163, 10]. In the searches of same-sign dilepton plus jets plus missing energy, the most stringent lower limit on doubly-charged scalar mass is 350 GeV [10]. As a case study, we first consider the scenario of $M_{H^{\pm\pm}} = 400\,\text{GeV}$, which satisfies the current direct LHC constraints. The kinematic variables we use to distinguish the signal from backgrounds are the missing transverse energy $E_T^{\rm miss}$, the effective mass $M_{\rm eff}$ defined as scalar sum of transverse momenta of all reconstructed leptons, jets, and missing energy, the separation $\Delta R_{\ell\ell}$ between two leptons, the azimuthal angle $\Delta\phi(\ell\ell, E_T^{\rm miss})$ between the two lepton system and $E_T^{\rm miss}$, the invariant mass of all jets $M_{\rm jets}$, and the cluster transverse mass from jets and $E_T^{\rm miss}$ defined as [190]

$$M_T^{\rm jets} \equiv \left[\left(\sqrt{M_{\rm jets}^2 + \left|\sum_j \overrightarrow{p}_T^{\,j}\right|^2} + E_T^{\rm miss}\right)^2 - \left|\sum_j \overrightarrow{p}_T^{\,j} + \overrightarrow{E}_T^{\rm miss}\right|^2\right]^{1/2} . \tag{4.32}$$

To enhance the signal-to-background ratio, the selection cuts we applied are as follows, and the corresponding cut-flows for the cross sections of signal and backgrounds are collected in Table 8.

- $0.3 < \Delta R_{\ell\ell} < 2.0$. The lower limit of $\Delta R_{\ell\ell}$ separates the leptons for isolation. The leptons in our signal emerge from the decay of two same-sign $W$ bosons which are from the decay of $H^{\pm\pm}$. However, the leptons associated with the background processes emerge from the decays of $W$ and $Z$ bosons which are well separated. Therefore, the leptons in the signal tend to have smaller $\Delta R_{\ell\ell}$. The distributions of $\Delta R_{\ell\ell}$ for the signal and backgrounds are presented in the top left panel of Fig. 21.
- $E_T^{\rm miss} > 110\,\text{GeV}$. One of the decay products emerging from $H^{\pm\pm}$ is the light neutral scalar $\phi$ which decays only into neutrinos and appears to be invisible in the detector. Due to the existence of the massive $\phi$ along with the neutrinos from $W$ boson decay, our signal tends to have larger missing transverse energy compared to the background processes (see the top right panel of Fig. 21 for distributions). Consequently, we choose a high $E_T^{\rm miss}$ threshold to distinguish the signal from backgrounds.

- $M_{\rm eff} > 350\,{\rm GeV}$. Borrowed from the SUSY searches [191, 192], the effective mass $M_{\rm eff}$ is a measure of the overall activity of the event. It provides a good discrimination especially for signals with energetic jets. The jets in our signal are from $W$ decay while the jets associated with backgrounds are from the QCD productions, which makes the jets from the signal to be more energetic in general. This can be seen in the middle left panel of Fig. 21. Thus the effective mass associated with the signal is distributed at higher values.
- $M_T^{\rm jets} > 300\,{\rm GeV}$. Since the decay products from $H^{\pm\pm}$ contain invisible particles, we cannot fully reconstruct its mass. The transverse mass $M_T^{\rm jets}$ is an alternative option in this situation. We choose to reconstruct the transverse mass $M_T^{\rm jets}$ of $H^{\pm\pm}$ using jets and $E_T^{\rm miss}$ in order to reproduce its mass peak as close as possible. From the distributions shown in the middle right panel of Fig. 21, we can see that the transverse mass for the signal peaks around 400 GeV while for backgrounds it peaks at a smaller value. Consequently, a large $M_T^{\rm jets}$ cut can help us to discriminate the signal from backgrounds.
- $150\,{\rm GeV} < M_{\rm jets} < 350\,{\rm GeV}$. As mentioned above, the jets in the signal emerge from the hadronic decays of $W$ boson while the jets associated with the main backgrounds are from QCD production. As a result, the invariant mass of all jets from backgrounds has a broader and flatter distribution, while the distribution for the signal is concentrated in the region between the two $W$ boson mass threshold and the doubly-charged scalar mass, as shown in the bottom left panel of Fig. 21. This provides a good observable to distinguish the signal from backgrounds.
- $\Delta\phi(\ell\ell, E_T^{\rm miss}) < 1.5$. The contributions to $E_T^{\rm miss}$ associated with the signal are neutrinos and the light neutral scalar $\phi$ from the decay of $H^{\pm\pm}$. The signal decay products include also same-sign dileptons and, consequently, the azimuthal angle between the same-sign dilepton and $E_T^{\rm miss}$ in the signal tends to have a small value. In contrast, the backgrounds do not have such kinematics and thus the distribution of $\Delta\phi(\ell\ell, E_T^{\rm miss})$ is rather flat for the background processes. The distributions for the signal and backgrounds are shown in the bottom right panel of Fig. 21.

After all the cuts, it is found in Table 8 that the cross section for our signal is only a few times smaller than that for the SM backgrounds. To calculate the signal significance,

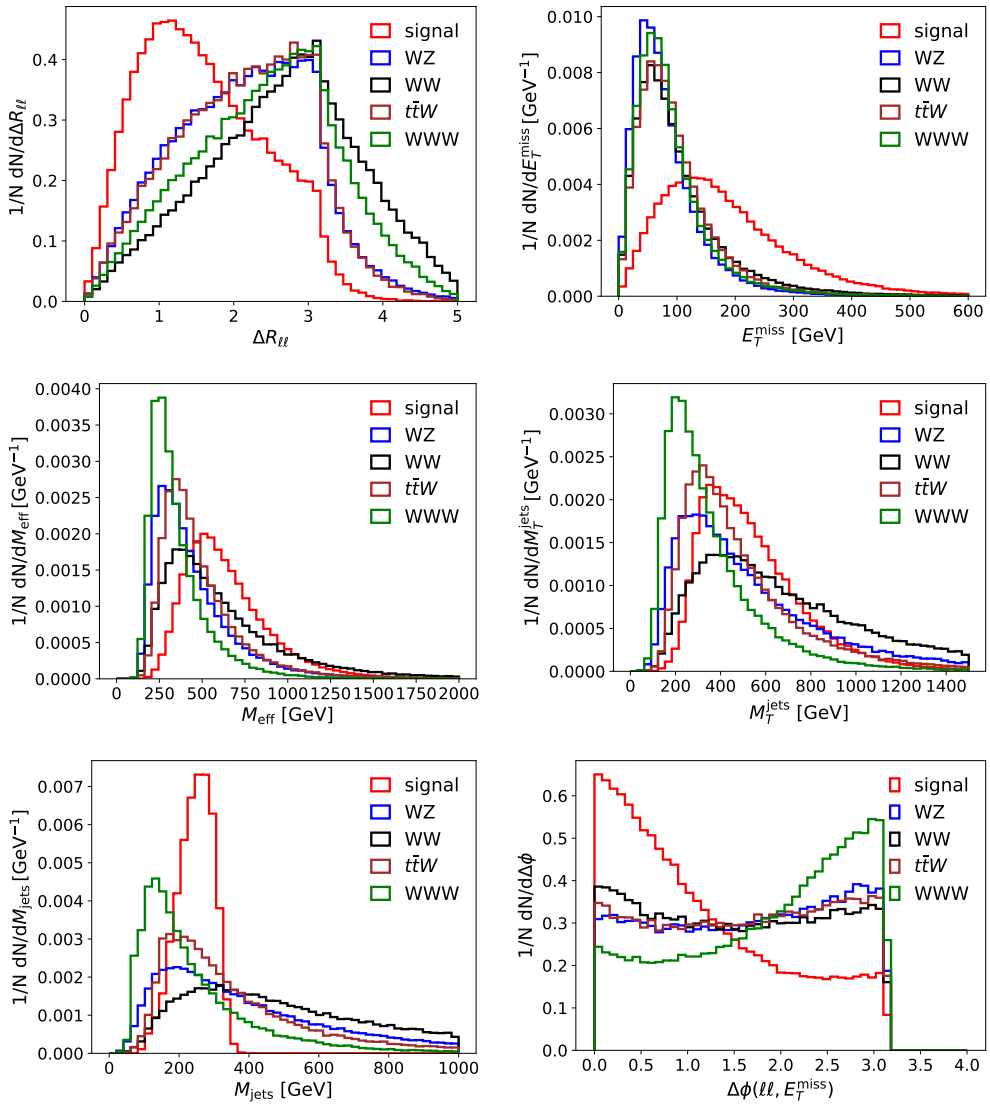


Figure 21: Distributions of observables used in cut-based analysis for the signal $W^{\pm}W^{\pm}\phi$ and SM backgrounds $WZ$, $WW$, $t\bar{t}W$, $WWW$: separation of two leptons $\Delta R_{\ell\ell}$ (top left), missing transverse energy $E_T^{\rm miss}$ (top right), effective mass $M_{\rm eff}$ (middle left), transverse mass $M_T^{\rm jets}$ of $H^{\pm\pm}$ defined in Eq. (4.32) (middle right), invariant mass $M_{\rm jets}$ of jets (bottom left), and the azimuthal angle $\Delta\phi(\ell\ell,\, E_T^{\rm miss})$ between dilepton and missing energy (bottom right). All the distributions are normalized to be unity.

Table 8: Cut-flow of the cross sections for signal and SM backgrounds $WZ$, $WW$, $t\bar{t}W$, $WWW$ at the HL-LHC with $M_{H^{\pm\pm}} = 400\,\text{GeV}$.

| Cut Selection | Signal [fb] | $WZ$ [fb] | $WW$ [fb] | $t\bar{t}W$ [fb] | $WWW$ [fb] |
|---|---|---|---|---|---|
| $0.3 < \Delta R_{\ell\ell} < 2.0$ | 0.092 | 4.5 | 1.3 | 0.64 | 0.25 |
| $E_T^{\text{miss}} > 110\,\text{GeV}$ | 0.067 | 1.1 | 0.41 | 0.191 | 0.053 |
| $M_{\text{eff}} > 350\,\text{GeV}$ | 0.066 | 0.95 | 0.39 | 0.18 | 0.039 |
| $M_T^{\text{jets}} > 300\,\text{GeV}$ | 0.064 | 0.94 | 0.39 | 0.18 | 0.038 |
| $150\,\text{GeV} < M_{\text{jets}} < 350\,\text{GeV}$ | 0.062 | 0.22 | 0.067 | 0.073 | 0.018 |
| $\Delta\phi(\ell\ell, E_T^{\text{miss}}) < 1.5$ | 0.049 | 0.13 | 0.035 | 0.040 | 0.010 |

we use the metric $\sigma = S/\sqrt{S+B}$ where $S$ and $B$ are the numbers of events for signal and backgrounds respectively, and we have not included any systematic uncertainties in our analysis. The expected event yields at the HL-LHC after all the cuts above are shown in Table 9. It is clear that the significance can reach $5\sigma$ in the cut-based analysis, which implies a great potential for discovery of the signal $H^{\pm\pm} \to W^{\pm}W^{\pm}\phi$ at the HL-LHC.

**4.2.1.2 BDT improvement** In order to further control the backgrounds, we adopt the BDT technique. In particular, we use the `XGBoost` package [193] to build the BDT. In addition to the variables mentioned above, we also feed the BDT the following variables:

- invariant mass $M_{\ell\ell}$ of same-sign dileptons;
- transverse mass $M_T^{\ell\ell}$ constructed from leptons and $E_T^{\text{miss}}$;
- azimuthal angles $\Delta\phi(\ell_1, E_T^{\text{miss}})$ and $\Delta\phi(\ell_2, E_T^{\text{miss}})$ between leptons and $E_T^{\text{miss}}$;
- azimuthal angle $\Delta\phi(j_1, E_T^{\text{miss}})$ between leading jet and $E_T^{\text{miss}}$;
- separation $\Delta R_{\ell_1 j_1}$ and $\Delta R_{\ell_2 j_1}$ of leptons and leading jet;
- minimum separation $\min\Delta R_{jj}$ of two jets;

Table 9: Number of events in cut-based and BDT analysis for signal and backgrounds at the HL-LHC with 3 $\text{ab}^{-1}$ luminosity and for $M_{H^{\pm\pm}} = 400\,\text{GeV}$. The last column shows the significance of signal.

| | Signal | $WZ$ | $WW$ | $t\bar{t}W$ | $WWW$ | Backgrounds | $\sigma$ |
|---|---|---|---|---|---|---|---|
| Number of events (cut-based) | 145.56 | 397.54 | 104.17 | 120.00 | 30.42 | 652.12 | 5.15 |
| Number of events (BDT-based) | 184.56 | 70.00 | 23.00 | 29.30 | 10.48 | 132.78 | 10.36 |

- minimum separation $\min\Delta R_{\ell j}$ of leptons and jets;
- minimum invariant mass $\min M_{jj}$ of two jets.

Some of the distributions, such as those for $\min M_{jj}$, $M_{\ell\ell}$, $M_T^{\ell\ell}$ and $\min\Delta R_{jj}$, are shown in Fig. 22. We will see in the lower right panel of Fig. 23 that these distributions are also very important for discriminating the signal from backgrounds.

The hyperparameters we used to train BDT are as follows: the learning rate is 0.1, the number of trees is 500, the maximum depth of each tree is 3, the fraction of events to train tree on is 0.6, the fraction of features to train tree on is 0.8, the minimum sum of instance weight needed in a child is 3, and the minimum loss reduction required to make a further partition on a leaf node of the tree is 0.2.

We split the data set into a training set and a testing set to make sure that there is no over-fitting. The BDT responses for our testing set are shown in the upper panel of Fig. 23. The BDT response close to 1 means the event is more signal-like while the response around 0 means the event is more background-like. We can see that our BDT classifier behaves quite good on the testing set. The receiver operating characteristic curve (ROC curve) of BDT and its feature importance are presented respectively in the lower left and right panels of Fig. 23. The feature importance is measured by "gain", which is defined as the average training loss

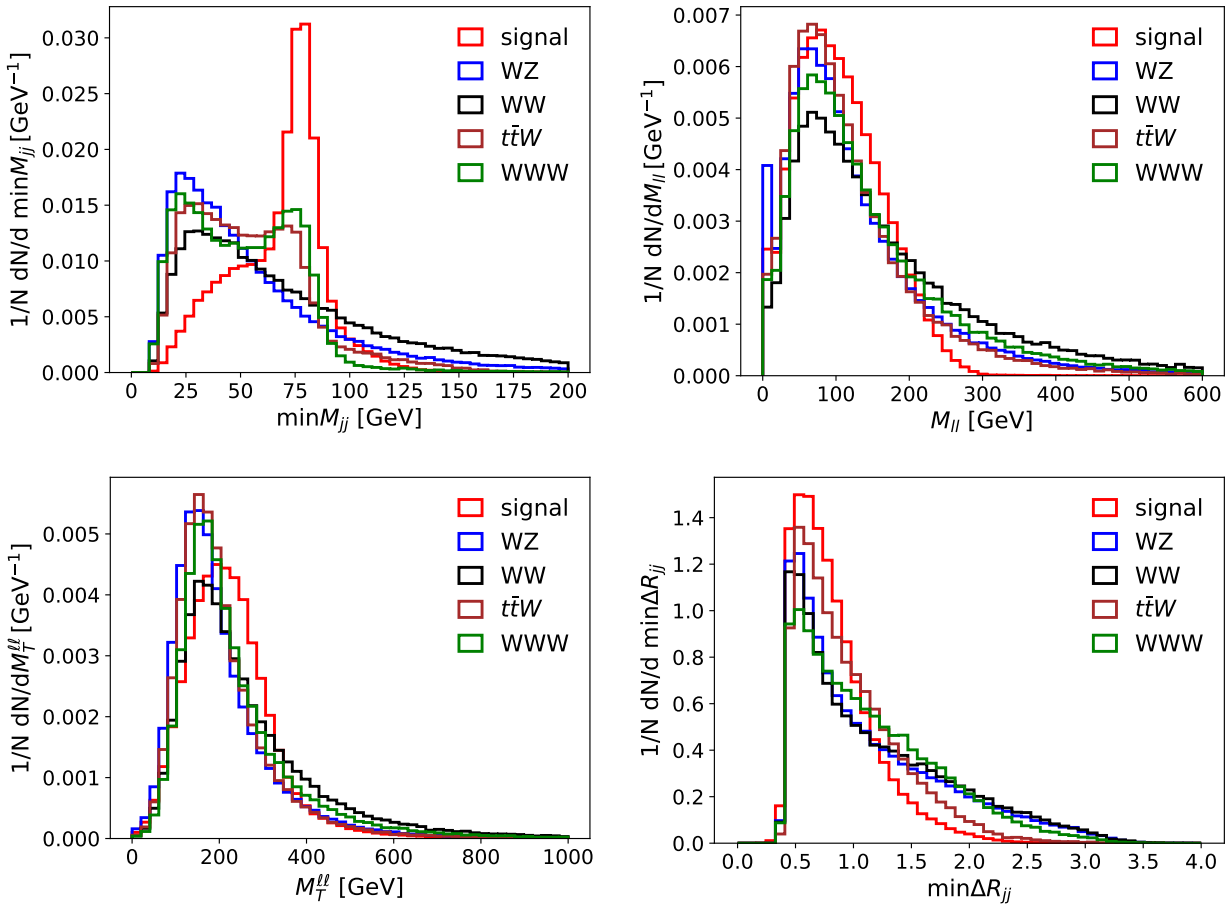


Figure 22: More distributions of variables that are found by BDT to be important for distinguishing signal $W^{\pm}W^{\pm}\phi$ from backgrounds $WZ$, $WW$, $t\bar{t}W$, $WWW$: minimum invariant mass min$M_{jj}$ of two jets (upper left), invariant mass $M_{\ell\ell}$ of same-sign dilepton (upper right), transverse mass $M_T^{\ell\ell}$ of leptons and missing energy (lower left), and minimum separation min$\Delta R_{jj}$ of two jets (lower right).

reduction gained when using a feature for splitting. The importance plot shows the top 10 important variables in the BDT training. The observables used in the cut-based analysis rank among the top 10 by the BDT, where the most important one is the effective mass $M_{\text{eff}}$, followed by $M_{\text{jets}}$ and $E_T^{\text{miss}}$. In addition, the BDT determines that the distributions min$M_{jj}$, $M_{\ell\ell}$, $M_T^{\ell\ell}$ and min$\Delta R_{jj}$ shown in Fig. 22 are also very important.

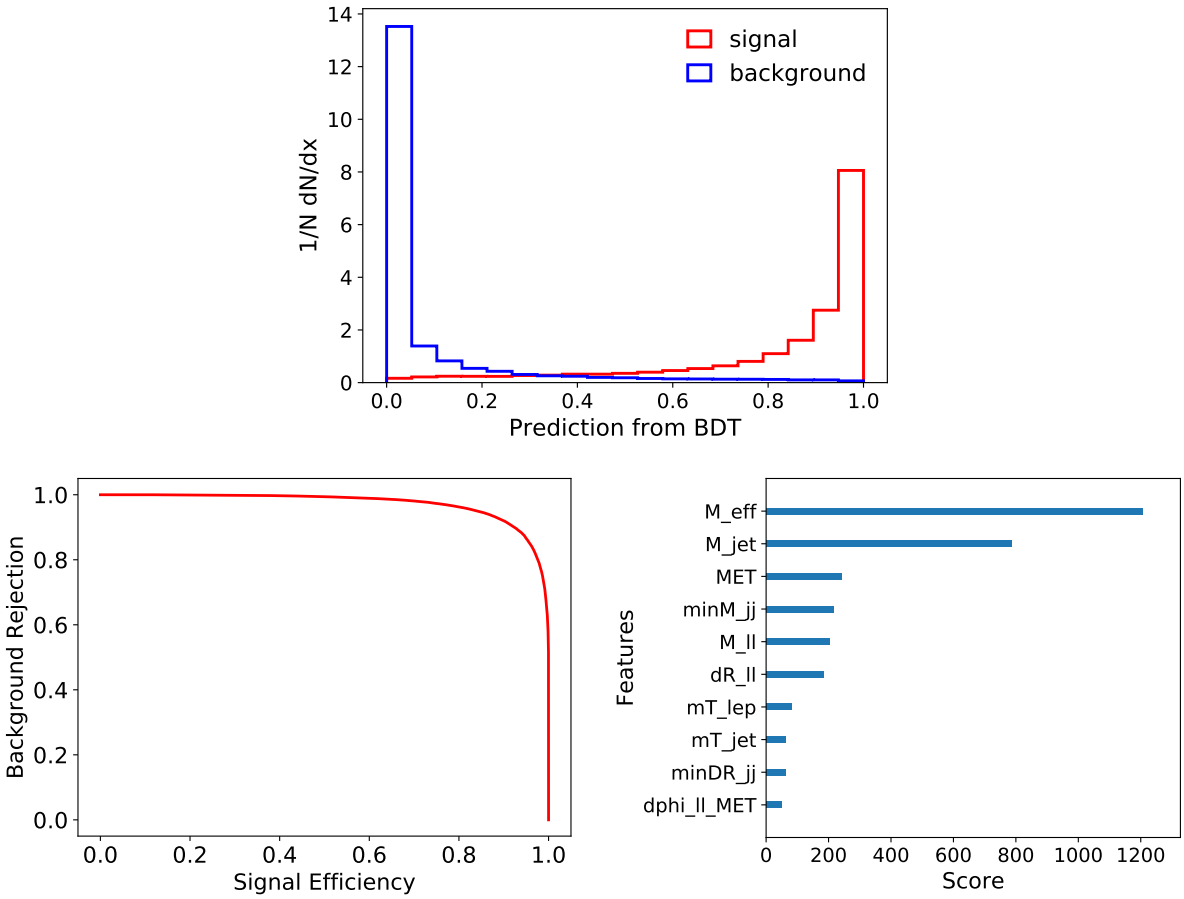


Figure 23: BDT response (upper), ROC curve (lower left) and feature importance (lower right) for the small Yukawa coupling scenario with $M_{H^{\pm\pm}} = 400$ GeV. In the feature importance plot, the variables from top to bottom are respectively $M_{\text{eff}}$, $M_{\text{jets}}$, $E_T^{\text{miss}}$, $\min M_{jj}$, $M_{\ell\ell}$, $\Delta R_{\ell\ell}$, $M_T^{\ell\ell}$, $M_T^{\text{jets}}$, $\min \Delta R_{jj}$ and $\Delta\phi(\ell\ell, E_T^{\text{miss}})$.

We choose the BDT cut such that it maximizes the significance of signal. For $M_{H^{\pm\pm}} = 400\,\text{GeV}$, the event yields of signal and backgrounds after the BDT cut are reported in Table 9. We can see that the BDT can eliminate backgrounds significantly while keeping most of the signal. The significance can reach 10.36 with the help of BDT, which is improved remarkably in comparison to the cut-based method in Section 4.2.1.1.

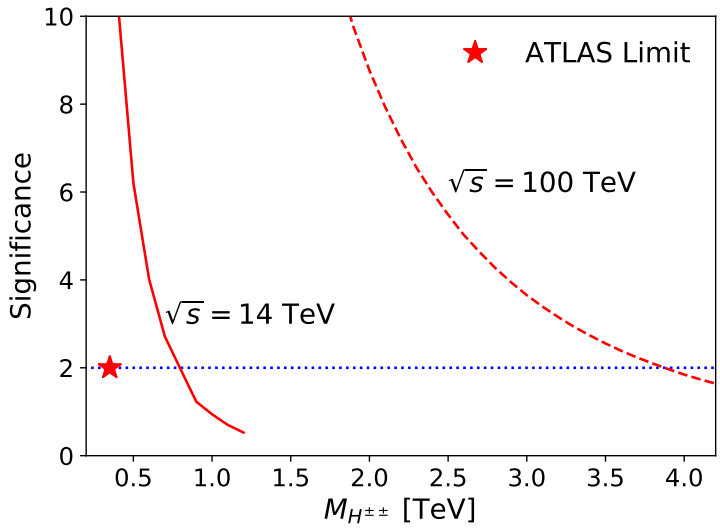


Figure 24: BDT significance as a function of $M_{H^{\pm\pm}}$ at the HL-LHC (solid) and future 100 TeV collider (dashed) for the small Yukawa coupling scenario. The red star is current LHC $2\sigma$ limit on $M_{H^{\pm\pm}}$ in the $W^{\pm}W^{\pm}$ channel [10].

**4.2.1.3 Mass reaches** To explore the discovery potential of $H^{\pm\pm}$ in the small Yukawa coupling scenario at the HL-LHC, we generate event samples for the signal process for $M_{H^{\pm\pm}}$ in the range from 300 GeV to 1.2 TeV with the step of 100 GeV. We build BDTs for different masses to discriminate the signal from the SM backgrounds and maximize the significance. The significance as a function of the doubly-charged scalar mass $M_{H^{\pm\pm}}$ is shown in Figure 24 as the solid line. It is found that we can reach $M_{H^{\pm\pm}} \simeq 800$ GeV at the $2\sigma$ significance in the $W^{\pm}W^{\pm}\phi$ channel for the small Yukawa scenario at the HL-LHC.

At future 100 TeV hadron colliders such as FCC-hh and SPPC, the production cross section of $H^{\pm\pm}$ can be largely enhanced, as shown in Fig. 20. Following the same BDT analysis as that at 14 TeV LHC, the significance of signal as a function of $M_{H^{\pm\pm}}$ is presented as the dashed line in Figure 24. Benefiting from the large cross section, the prospect of $M_{H^{\pm\pm}}$ can reach up to 3.8 TeV at the $2\sigma$ sensitivity at the 100 TeV collider.

### 4.2.2 Large Yukawa coupling scenario

Another case of interest in contrast to the previous one is the large Yukawa coupling scenario. According to the low-energy flavor limits in Table 7, most elements of the Yukawa coupling matrix $Y_{\alpha\beta}$ are bounded to be small while $Y_{\mu\mu}$ can be of $\mathcal{O}(1)$ for TeV-scale $H^{\pm\pm}$. Note that the effective coupling between neutrinos and leptonic scalars ($H_1$ and $A_1$) in our model is of order $\lambda_{\alpha\beta} \sim 2\sqrt{2}\, Y_{\alpha\beta} \sin\theta$ (cf. Table 6); therefore, $Y_{\mu\mu} \sim \mathcal{O}(1)$ could also be probed at hadron colliders via the VBF process discussed in our previous study [118]. For example, a $Y_{\mu\mu} = 1.5$ Yukawa coupling leads to an effective coupling $\lambda_{\mu\mu} \sim 0.58$ which is within the $2\sigma$ LHC sensitivity in the VBF mode [118]. Although the $Y_{\tau\tau}$ coupling is the least constrained (cf. Table 7), final states involving taus at the hadron colliders are more difficult to analyze; therefore, we only focus on the muon final states and leave the tau signal for a future work.

After considering the constraints from perturbativity and unitarity in Section 4.1.3, we found that the $Y_{\mu\mu}$ component can be as high as 1.5 as presented in Fig. 19. This is still consistent with the muon $g-2$ bound given in Table 7 for a TeV-scale $H^{\pm\pm}$. In this scenario, the contributions from other Yukawa coupling elements are negligible, and the doubly-charged scalar $H^{\pm\pm}$ decays predominately into a pair of same-sign muons, *i.e.* $\mathrm{BR}(H^{\pm\pm} \to \mu^\pm\mu^\pm) \simeq 100\%$. For large $Y_{\mu\mu}$ the main decay channel for the singly-charged scalar will be $H^\pm \to \mu^\pm\,\nu$. However, the $H^\pm \to W^\pm\,\phi$ channel is still feasible and its BR varies from 10% to 20% depending on the mass of $H^\pm$, as shown in the lower left panel of Fig. 17. With the $W$ boson decaying hadronically, the $\phi$ induced signal at the hadron collider emerges from the associated production channel as follows:

$$pp \to H^{\pm\pm}(\to \mu^\pm\mu^\pm)\, H^\mp(\to W^\mp\phi) \to \mu^\pm\mu^\pm + 2\,\mathrm{jets} + E_T^{\mathrm{miss}}\,,$$

*i.e.* same-sign muon pair plus two jets from $W$ boson decay plus transverse missing energy from $\phi$. We should mention here that the traditional 3-$\mu$ or 4-$\mu$ channels will still be the discovery mode for this scenario, but our choice of the final state and analysis is useful to determine the mass of leptonic scalar $\phi$ ($H_1/A_1$) as will be shown in Section 4.2.2.2.

The same-sign dilepton signals are "smoking-gun" signals of doubly-charged scalars at the high-energy colliders, and have been searched for at the LEP [194, 195, 196], Tevatron [197,

198, 199, 200], LHC data at 7 TeV [201, 202], 8 TeV [203, 204] and 13 TeV [11, 162]. For the scenario BR($H^{\pm\pm} \to \mu^\pm\mu^\pm$) = 100%, the current most stringent lower dilepton limit on $M_{H^{\pm\pm}}$ is from the LHC 13 TeV data, being 846 GeV [11]. For illustration purpose, we use

$$M_{H^{\pm\pm}} = 900\,\text{GeV}\,, \quad M_{H^\pm} = 893\,\text{GeV} \tag{4.33}$$

as our benchmark scenario for the analysis below.

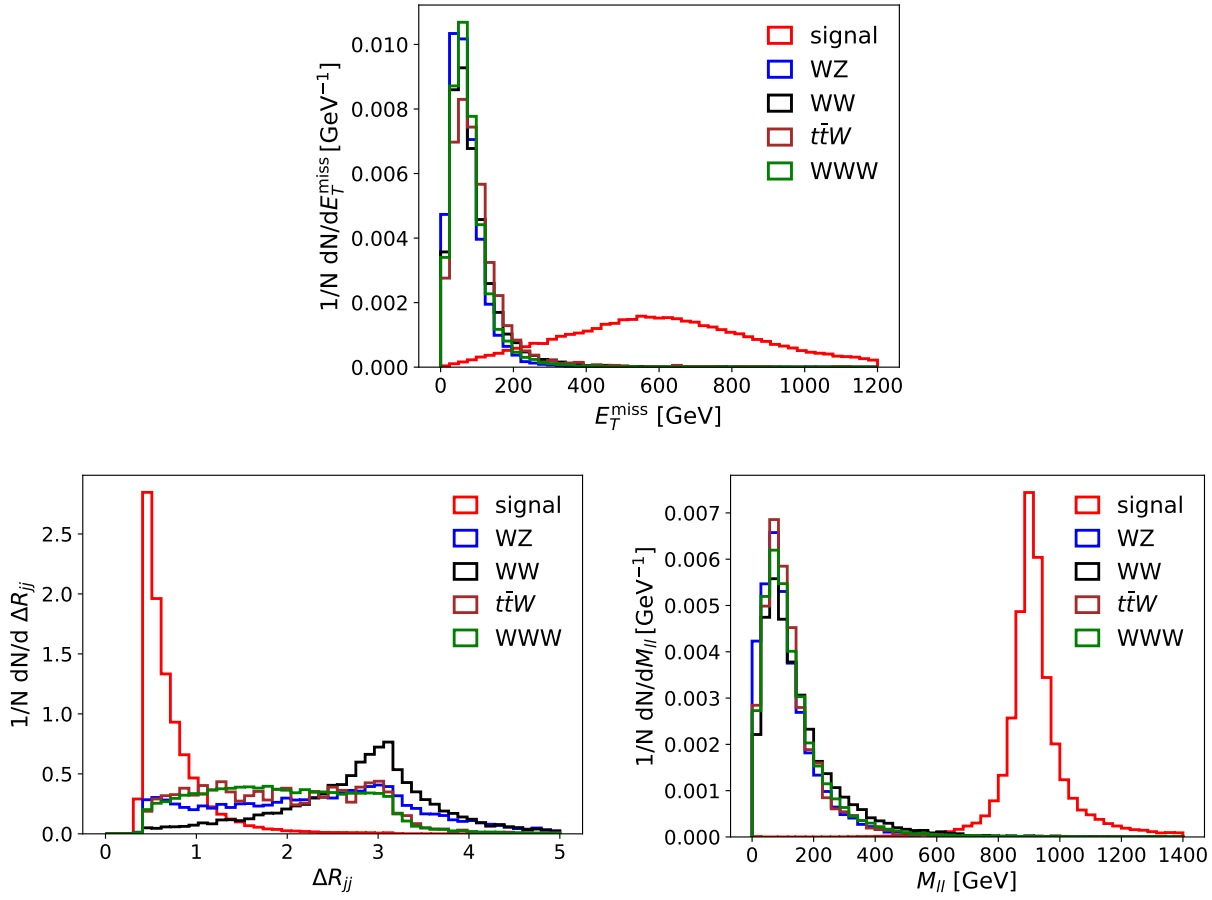


Figure 25: Distributions of $E_T^{\text{miss}}$ (upper), $\Delta R_{jj}$ (lower left) and $M_{\mu^\pm\mu^\pm}$ (lower right) in associated production $H^{\pm\pm}H^\mp$ and the SM backgrounds $WZ$, $WW$, $t\bar{t}W$, $WWW$.

**4.2.2.1 Analysis and mass reaches** The signal samples are generated by using `MadGraph5`. Since the final state is similar to the small Yukawa coupling case, we use the same background samples as in Section 4.2.1. The muon and jet definitions are also kept unchanged.

All the events are required to have two reconstructed same-sign muons and two jets without any $b$-tagged jet. In addition, to further control the backgrounds the following cuts are applied, and the corresponding cut-flows for the cross sections of signal and backgrounds are presented in Table 10.

- $\min\Delta R_{\mu j} > 0.4$ and $\Delta R_{\mu\mu} > 0.3$. This is to satisfy the muon isolation criteria.
- $E_T^{\rm miss} > 200\,{\rm GeV}$. Since $E_T^{\rm miss}$ in the signal is from the scalar $\phi = H_1,\ A_1$, it tends to have a larger value than the backgrounds with a broader distribution, as shown in the upper panel of Fig. 25.
- $\Delta R_{jj} < 2$. The two jets in the signal are from the decay products of a very energetic $W$ boson, so they tend to be more collimated than the backgrounds. With the distributions shown in the lower left panel of Fig. 25, a small $\Delta R_{jj}$ can help us to reduce the backgrounds.
- $700\,{\rm GeV} < M_{\mu^\pm\mu^\pm} < 1100\,{\rm GeV}$. Since the same-sign muon pair appears from the decay of the $H^{\pm\pm}$ boson, their Breit–Wigner peak provides a strong discrimination against the SM backgrounds. This can be clearly seen in the lower right panel of Fig. 25.

Table 10: Cut-flow of the cross sections for signal and SM backgrounds $WZ$, $WW$, $t\bar{t}W$, $WWW$ at the HL-LHC for the large Yukawa coupling scenario (4.33). Backgrounds that are essentially eliminated are denoted by "$-$"s.

| Cut Selection | Signal [fb] | $WZ$ [fb] | $WW$ [fb] | $t\bar{t}W$ [fb] | $WWW$ [fb] |
|---|---|---|---|---|---|
| $\min\Delta R_{\mu j} > 0.4$ and $\Delta R_{\mu\mu} > 0.3$ | 0.0059 | 1.7 | 0.81 | 0.044 | 0.27 |
| $E_T^{\rm miss} > 200\,{\rm GeV}$ | 0.0056 | 0.036 | 0.049 | 0.0027 | 0.010 |
| $\Delta R_{jj} < 2$ | 0.0054 | 0.017 | 0.013 | 0.0019 | 0.0082 |
| $700\,{\rm GeV} < M_{\mu^\pm\mu^\pm} < 1100\,{\rm GeV}$ | 0.0050 | 0.00010 | 0.00015 | $-$ | 0.00019 |

As a result of very distinct topologies of the signal and backgrounds, the number of background events can be highly suppressed after the cuts, as reported in Table 10. The

expected numbers of events at the HL-LHC are shown in Table 11. In the cut-based analysis, the significance can reach $\sigma = 3.67$ for the benchmark scenario in Eq. (4.33).

Table 11: Number of events in cut-based and BDT analysis for associated production $H^{\pm\pm}H^{\mp}$ in the benchmark scenario (4.33) and the SM backgrounds at the HL-LHC with 3 ab$^{-1}$ luminosity. The last column shows the significance of signal. Backgrounds that are essentially eliminated by our cuts are denoted by "$-$"s.

| | Signal | $WZ$ | $WW$ | $t\bar{t}W$ | $WWW$ | Backgrounds | $\sigma$ |
|---|---|---|---|---|---|---|---|
| Number of events (Cut-based) | 14.87 | 0.32 | 0.46 | $-$ | 0.57 | 1.35 | 3.69 |
| Number of events (BDT-based) | 19.00 | $-$ | $-$ | $-$ | 0.06 | 0.06 | 4.35 |

As in the small Yukawa coupling case in Section 4.2.1, BDT can help us improve to some extent the sensitivity. In addition to the observables above in cut-and-count analysis, we also use the following observables:

- transverse momenta $p_{T,\mu_1}$ and $p_{T,\mu_2}$ of the two muons;
- effective mass $M_{\text{eff}}$;
- invariant mass $M_{jj}$ of two jets;
- total transverse momentum $p_{T,jj}$ of two jets;
- transverse mass $M_T$ constructed from jets and $E_T^{\text{miss}}$;
- azimuthal angle $\Delta\phi(\mu\mu, E_T^{\text{miss}})$ between two muons and $E_T^{\text{miss}}$.

The BDT score distribution is presented in Fig. 26. As expected, the signal is well separated from the backgrounds. Therefore the BDT can eliminate almost all the background events while keeping most of the signal events. The expected numbers of signal and background events after optimal BDT cuts are collected in the last row of Table 11. With the help of BDT, the sensitivity can reach a higher value at $\sigma = 4.35$.

Since the backgrounds can be highly suppressed by the BDT analysis, the significance will be mainly determined by the cross section of signal, which in turn depends on the mass

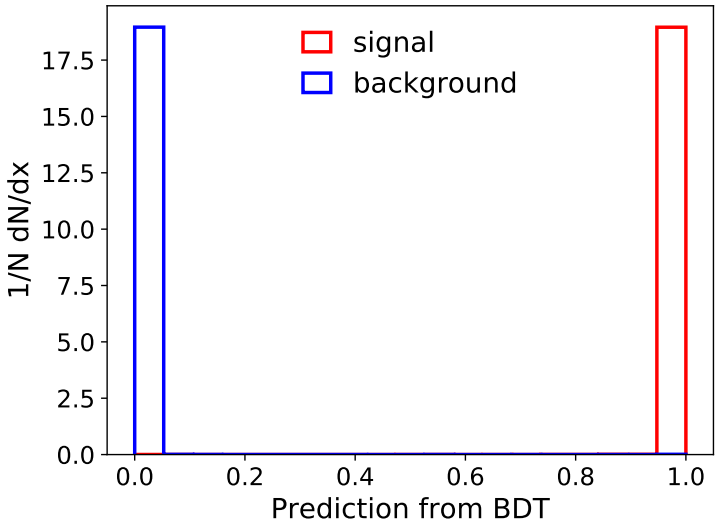


Figure 26: BDT score distribution for the large Yukawa coupling scenario.

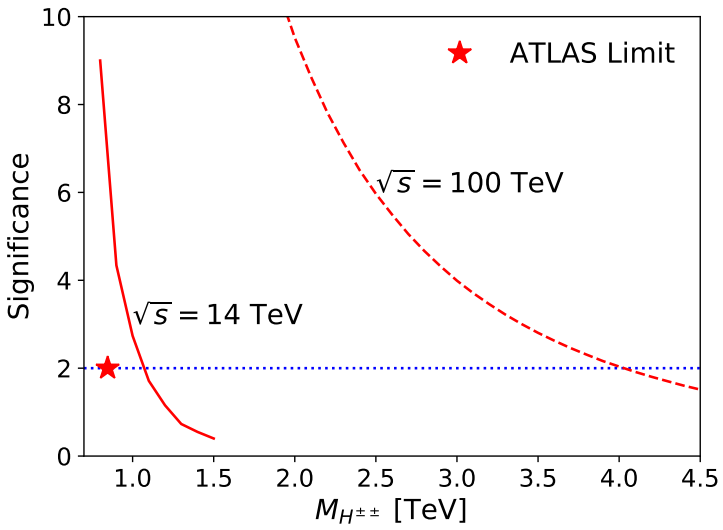


Figure 27: BDT significance as a function of $M_{H^{\pm\pm}}$ at the HL-LHC (solid) and future 100 TeV collider (dashed) for the large Yukawa coupling scenario. The red star indicates the current LHC $2\sigma$ limit on $M_{H^{\pm\pm}}$ with 100% BR into $\mu^{\pm}\mu^{\pm}$ [11].

of $H^{\pm\pm}$. We generate our signal samples in the step of 100 GeV for $M_{H^{\pm\pm}}$ varying from 900 GeV to 1.5 TeV. The resultant significance at the HL-LHC as a function of $M_{H^{\pm\pm}}$ is shown in Fig. 27 as the solid line. It turns out $H^{\pm\pm}$ can be probed up to 1.1 TeV at the $2\sigma$ sensitivity at the HL-LHC in the large Yukawa coupling scenario. At a future 100 TeV collider, the production cross section $\sigma(pp \to H^{\pm\pm}H^{\mp})$ can be enhanced by over one order of magnitude (see Fig. 20). The corresponding prospect of $M_{H^{\pm\pm}}$ can reach up to 4 TeV at the $2\sigma$ sensitivity, which is indicated by the dashed line in Fig. 27.

**4.2.2.2 Mass determination of the leptonic scalar $\phi$** For the associated production $H^{\pm\pm}H^{\mp}$ in the large Yukawa coupling case, the only missing particles is $\phi = H_1$, $A_1$, which provides a possibility to measure its mass. However, at the hadron colliders such as LHC, we can at most determine the transverse momentum of $\phi$ while its longitudinal momentum is completely lost. Therefore the usual method to determine a particle's mass is not applicable here. An alternative approach is to utilizes the transverse mass of a mother particle whose decay products contain a massive invisible daughter particle. To achieve this, we need to modify the definition of transverse mass in Eq. (4.32). In that equation, we do not consider the mass of the missing particles but simply assume the transverse energy of missing particles to be the same as the missing transverse momentum. The modified definition of missing transverse energy is

$$E_T^{\rm miss}(\tilde{m}) = \sqrt{\tilde{m}^2 + p_{T,\,\rm miss}^2}\,, \tag{4.34}$$

where $\tilde{m}$ is the assumed mass of $\phi$, and $p_{T,\,\rm miss}$ is the missing transverse momentum. Thus the cluster transverse mass $M_T$ can be re-expressed as a function of the assumed mass $\tilde{m}$:

$$M_T(\tilde{m}) = \left[\left(\sqrt{M_{\rm jets}^2 + \left|\sum_j \overrightarrow{p}_T^{\,j}\right|^2} + \sqrt{\tilde{m}^2 + p_{T,\,\rm miss}^2}\right)^2 - \left|\sum_j \overrightarrow{p}_T^{\,j} + \overrightarrow{p}_{T,\,\rm miss}\right|^2\right]^{1/2}. \tag{4.35}$$

As shown in Refs. [205, 206], the endpoint of $M_T$ distribution will increase with the assumed mass $\tilde{m}$, and a kink will appear at the point of $\tilde{m} = m$ when the assumed mass $\tilde{m}$ is equal to the real mass $m$ of the invisible daughter particle.

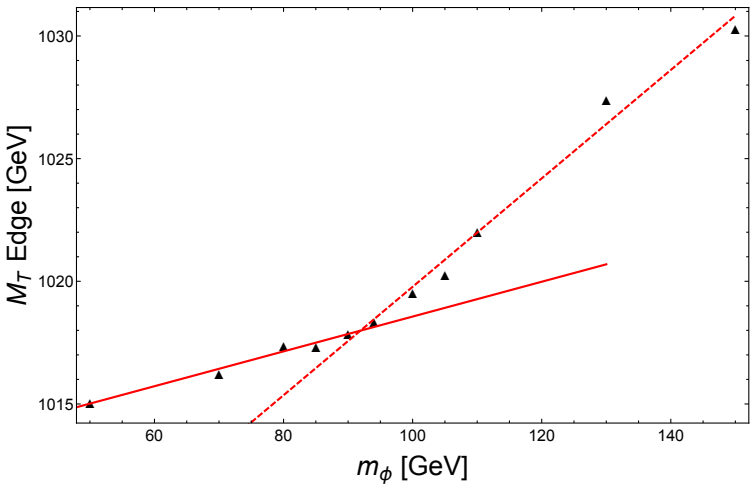


Figure 28: $M_T$ endpoints (black triangles) from `EdgeFinder` fitting [12] as a function of assumed trial mass $m_\phi$. The red straight lines are from linear fittings as an illustration of kink position.

As an explicit example, we choose the scalar mass $m_\phi = 89.28\,\text{GeV}$, and the masses of charged scalars are set as in Eq. (4.33). We calculate the transverse mass $M_T$ of the simulated events by Eq. (4.35) with different choices of $\tilde{m}$, and then use package `EdgeFinder` [12] to find the endpoint of $M_T$ distribution for each $\tilde{m}$ choice. The result is shown in Fig. 28. By fitting the data points, a kink is found at $\tilde{m} = (93.60 \pm 11.43)\,\text{GeV}$. Comparing $\tilde{m}$ at the kink with the real mass $m_\phi$, we find that this method provides a great potential for measuring the mass of the invisible light scalar $\phi = H_1,\, A_1$ at the LHC.

We note that the fitting process may be associated with some uncertainties for both $M_T$ edges and $m_\phi$. To test the robustness of fitting result, we smear the $M_T$ edge according to the initial error bars from the `EdgeFinder` package in a Normal distribution. Using 100 points for trial, we find that the mass determination by the kink yields a result $\tilde{m} = (93.55 \pm 11.41)\,\text{GeV}$. Since the uncertainty range does not change, we can state that the kink-finding method leads to a rather reliable mass determination. It should be noted that it is difficult to apply the mass determination technique used here to the small Yukawa coupling scenario in Section 4.2.1, since in that case $\phi$ is from $H^{\pm\pm}$ decay, which leads to the appearance of

missing energy from both neutrinos from $W$ boson decay and the invisible scalar $\phi$.

### 4.2.3 Intermediate Yukawa coupling scenario

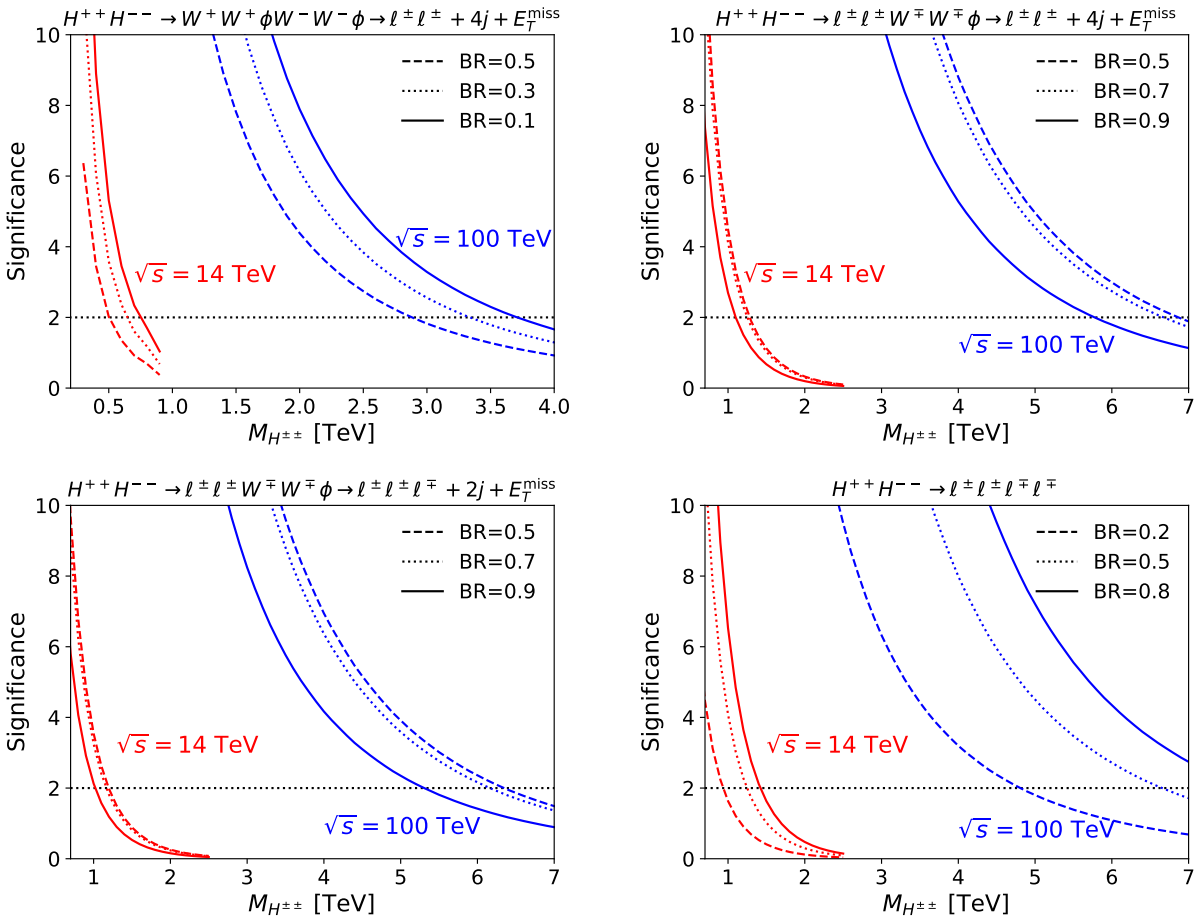


Figure 29: Significance as a function of $M_{H^{\pm\pm}}$ at the HL-LHC (red) and future 100 TeV collider (blue) for the intermediate Yukawa coupling scenario, in the channels of $H^{++}H^{--} \to W^+W^+\phi W^-W^-\phi \to \ell^\pm\ell^\pm + 4j + E_T^{\rm miss}$ (top left), $\ell^\pm\ell^\pm W^\mp W^\mp\phi \to \ell^\pm\ell^\pm + 4j + E_T^{\rm miss}$ (top right), $\ell^\pm\ell^\pm W^\mp W^\mp\phi \to \ell^\pm\ell^\pm\ell^\mp + 2j + E_T^{\rm miss}$ (bottom left) and $\ell^+\ell^+\ell^-\ell^-$ (bottom right). The "BR" in all the legends refers to the leptonic decay branching fraction BR($H^{\pm\pm} \to \ell^\pm\ell^\pm$) of the doubly-charged scalar.

For the completeness of our study, we also investigate the mass reach in the intermediate Yukawa coupling scenario. If the Yukawa coupling is of order $\mathcal{O}(10^{-2} - 1)$, the branching

fraction of leptonic channel $H^{\pm\pm} \to \ell^\pm_\alpha \ell^\pm_\beta$ could be comparable to the bosonic channel $H^{\pm\pm} \to W^\pm W^\pm \phi$. Since these two channels make up all the doubly-charged scalar decay, once we fix the branching fraction of one channel, the other one could be easily obtained, thus we could scale the cross section of pair production $pp \to H^{++}H^{--}$ accordingly to estimate the mass reach with different final states.

The first process we consider is the same as that in small Yukawa coupling scenario in Section 4.2.1, i.e. with both doubly-charged scalars decaying bosonically, and the same-sign $W$ bosons decaying leptonically. The final state would be a pair of same-sign leptons plus jets and large missing transverse energy: $H^{++}(\to W^+W^+\phi)\ H^{--}(\to W^-W^-\phi) \to \ell^\pm\ell^\pm + 4\,\text{jets} + E_T^{\text{miss}}$. Since the branching fraction of the bosonic channel is no longer 100% for intermediate Yukawa couplings, the mass reach would be undermined by the rising branching fraction of the leptonic decay channel $H^{\pm\pm} \to \ell^\pm\ell^\pm$. The significance of $H^{\pm\pm}$ in this channel is shown in the top left panel of Fig. 29 as function of $M_{H^{\pm\pm}}$, where the red and blue lines are respectively for the HL-LHC and future 100 TeV collider. As shown in this figure, the doubly-charged scalar can be probed at the $2\sigma$ C.L. with mass below 500 GeV (2.9 TeV) at the HL-LHC (future 100 TeV collider) for BR($H^{\pm\pm} \to \ell^\pm\ell^\pm$) = 50%. As the leptonic BR decreases, the mass reach increases, as expected, up to the ones reported in Fig. 24 (corresponding to BR($H^{\pm\pm} \to \ell^\pm\ell^\pm$)=0).

When the leptonic branching fraction is large enough, it is more likely that one of the pair-produced $H^{\pm\pm}$ decays leptonically and the other one decays bosonically. In this case, the final states with two or three charged leptons are of great interest. The two same-sign leptons can be used to reconstruct the Breit–Wigner peak of the mother doubly-changed scalar, making such signals almost background free. The corresponding significances of $H^{\pm\pm}$ in the two-lepton channel $H^{++}H^{--} \to \ell^\pm\ell^\pm W^\mp W^\mp \phi \to \ell^\pm\ell^\pm + 4j + E_T^{\text{miss}}$ and three-lepton channel $H^{++}H^{--} \to \ell^\pm\ell^\pm W^\mp W^\mp \phi \to \ell^\pm\ell^\pm\ell^\mp + 2j + E_T^{\text{miss}}$ are shown respectively in the top right and bottom left panels of Fig. 29. In the two-lepton channel, the $2\sigma$ sensitivities for $H^{\pm\pm}$ mass are respectively 1.1 TeV at HL-LHC and 5.7 TeV at future 100 TeV collider for BR($H^{\pm\pm} \to \ell^\pm\ell^\pm$) $< 90\%$. With the same branching fraction choice, the mass reach of $H^{\pm\pm}$ in the three-lepton final state is slightly lower – 1 (5.3) TeV at the HL-LHC (future 100 TeV collider).

The last case is the four-lepton final state via the process $H^{++}H^{--} \to \ell^+\ell^+\ell^-\ell^-$. Since we have two Breit–Wigner peaks from the two pairs of same-sign leptons, the search of $H^{\pm\pm}$ is same as in the standard Type-II seesaw, and the only limitations are the cross section of pair production and the branching fraction of the leptonic decay channel. The resultant significance of $H^{\pm\pm}$ in this channel is shown in the bottom right panel of Fig. 29. As shown in this figure, at the $2\sigma$ C.L. the doubly-charged scalar mass can reach respectively 950 GeV and 4.8 TeV at HL-LHC and future 100 TeV collider in the $\ell^+\ell^+\ell^-\ell^-$ channel with $\mathrm{BR}(H^{\pm\pm} \to \ell^\pm\ell^\pm) > 20\%$.

# 5.0 Conclusions

## 5.1 Conclusions on Higgs couplings Study

Precision measurements of Higgs couplings at high energy scale is of vital importance in today's particle physics research. Any deviation of Higgs couplings from the SM values could be a gateway to possible new physics. The first part of my thesis work focused on this area. In chapters 2 and 3, the phenomenology of $HZZ$ and $Ht\bar{t}$ couplings at TeV scale were studied in details, which highlight the Higgs couplings in time-like domain and space-like domain respectively.

In chapter 2, we have systematically studied the off-shell Higgs production in the $pp \to H^* \to Z(\ell\ell)Z(\nu\nu)$ channel at the high-luminosity LHC. We showed that this signature is crucial to probe the Higgs couplings across different energy scales potentially shedding light on new physics at the ultraviolet regime. To illustrate its physics potential, we derived the LHC sensitivity to three BSM benchmark scenarios where the new physics effects are parametrized in terms of the Higgs boson width, the effective field theory framework, and a non-local Higgs-top coupling form factor. The combination of a large signal rate and a precise phenomenological probe for the process energy scale, due to the transverse $ZZ$ mass, renders strong limits for all considered BSM scenarios. A summary table and comparison with the existing results in the literature are provided in Table 3. Adopting Machine-learning techniques, we demonstrated in the form of BDT that the HL-LHC, with $\mathcal{L} = 3$ ab$^{-1}$ of data, will display large sensitivity to the Higgs boson width, $\Gamma_H/\Gamma_H^{SM} < 1.31$. In addition, the characteristic high energy behavior for the new physics terms within the EFT framework results in relevant bounds on the $(\kappa_t, \kappa_g)$ new physics parameters, resolving the low energy degeneracy in the gluon fusion Higgs production. In particular, we observe that the LHC can bound the top Yukawa within $\kappa_t \approx [0.4, 1.1]$ at 95% CL. The upper bound on $\kappa_t$ is complementary to the direct Yukawa measurement via $ttH$ and can be further improved in conjunction with additional relevant off-shell Higgs channels. Finally, when considering a more general hypothesis that features a non-local momentum-dependent

Higgs-top interaction, we obtain that the HL-LHC is sensitive to new physics effects at large energies with $\Lambda = 1.5$ TeV for $n = 2$ and $\Lambda = 2.1$ TeV for $n = 3$ at 95% CL. We conclude that, utilizing the promising $H^* \to Z(\ell^+\ell^-)Z(\nu\bar{\nu})$ channel at the HL-LHC and adopting the Machine-Learning techniques, the combination of a large signal rate and a precise phenomenological probe for the process energy scale renders improved sensitivities beyond the existing literature, to all the three BSM scenarios considered in this work.

In chapter 3, we studied the prospects to **directly** probe the Higgs-top coupling for new physics at high energy scales using the $pp \to t\bar{t}h$ process at the HL-LHC. We considered two beyond the SM scenarios, namely the SMEFT framework and a general Higgs-top form-factor, as discussed in Sec. 3.1. We presented in Sec. 3.2 the general phenomenological effects for these new physics contributions, showing that they could produce augmented new physics effects at high energy scales. Focusing on the boosted Higgs regime in association with jet substructure techniques, we explored the largest Higgs branching fraction $h \to b\bar{b}$ along with the clean leptonic top-quark decays. The BSM effects were constrained through a shape analysis on the $p_{Th}$ spectrum. We observed the potential sensitivity at the TeV-scale for new physics both in the EFT and form-factor scenarios. The chromomagnetic dipole operator was probed up to $\Lambda/\sqrt{c_{tG}} \approx 2.9$ TeV and the $\mathcal{O}_{t\phi}$ operator to $\Lambda/\sqrt{c_{t\phi}} \approx 1.0$ TeV, as shown in Sec. 3.2.1. The limits presented sub-leading differences between the linear and quadratic $c_i/\Lambda^2$ expansion, indicating that our phenomenological study satisfies the EFT expansion. Finally, when considering a more general Higgs-top quark form-factor in Sec. 3.2.2, we concluded that the HL-LHC is sensitive to new physics up to the scale $\Lambda = 2.1$ TeV for $n = 2$ and 2.7 TeV for $n = 3$ at 95% CL. Further details are summarized in Table 5. The $t\bar{t}h$ studies at high scales, which **directly** explore the Higgs-top Yukawa interaction, results in a competitive and complementary pathway for BSM sensitivity in comparison to the off-shell Higgs channels and the current ATLAS and CMS limits. Some improvements in sensitivity can be anticipated by including other modes, such as $t\bar{t}(h \to \gamma\gamma)$, which would yield a cleaner signal but a lower rate [207]. In addition, we can increase our present $t\bar{t}(h \to b\bar{b})$ statistical sample by about a factor of six, if we include one leptonic decay plus one hadronic decay of the $t\bar{t}$. The analysis, however, would be more complex, with significantly larger QCD backgrounds [208]. Finally, while we adopt `MadGraph5_aMC@NLO`

as our general Monte Carlo generator (that accounts for the signal EFT contributions at NLO QCD), we acknowledge some other recent important developments associated with the $t\bar{t}b\bar{b}$ background [209, 210, 211]. We leave those improvements to future work with realistic simulations.

### 5.2 Conclusions on BSM Search in UV-complete Neutrino Model

Another important part of my PhD research focused on BSM searches related to neutrino interactions. Since the non-standard neutrino interactions (NSIs) have been widely studied, there is an increasing need to achieve a UV completion for the EFT operators. In chapter 4, we presented a global $(B-L)$-conserved UV-complete neutrino mass model which contains a scalar triplet $\Delta$ and a singlet $\Phi$ both carrying a $B-L$ charge of $+2$. From mixing of the neutral components of $\Delta$ with $\Phi$, this model features new neutrino interactions along with a pair of (light) leptonic scalars $H_1$ and $A_1$, collectively denoted by $\phi$. The light leptonic scalar $\phi$ induces very rich phenomenological consequences.

The main points of our model features, allowed parameter space and the prospects of discovering this model at the HL-LHC and a future 100 TeV collider are summarized as follows:

- The proposed model ensembles the Type-II seesaw model. But unlike the standard Type-II seesaw model, the neutral component of the triplet $\Delta$ of this model does not acquire any VEV. As a result, there is no Majorana mass term, neutrinos are Dirac fermions, and the $SU(2)_L$ custodial symmetry remains unbroken in this model.
- In light of all the low-energy LFV constraints, the coupling $Y_{\mu\mu}$ can be as large as $\mathcal{O}(1)$ for a TeV-scale $H^{\pm\pm}$ while all other Yukawa couplings are more stringently constrained (see Fig. 18 and Table 7). Using RGEs, we have also determined the largest values of $\lambda_8$ and $Y_{\alpha\beta}$ at the EW scale in order to keep the theory perturbative all the way to the UV-complete scale, as shown in Fig. 19. It is remarkable that as a good approximation the perturbativity limits can be obtained analytically. We checked also the unitarity constraints for these couplings and found them to be much weaker compared to the

perturbativity limits.

- Originating from the gauge couplings, $H^{\pm\pm}$ and $H^{\pm}$ can decay into the light leptonic scalar $\phi = H_1,\ A_1$ via $H^{\pm\pm} \to W^{\pm}W^{\pm}\phi$ and $H^{\pm} \to W^{\pm}\phi$. The scalar $\phi$ provides additional sources of missing energy (along with the neutrinos from the decays of $W$ when the leptonic final states are selected) since it decays only into neutrinos, *i.e.* $\phi \to \nu\nu$. These new decay channels $H^{\pm\pm} \to W^{\pm}W^{\pm}\phi$ and $H^{\pm} \to W^{\pm}\phi$ dominate for small $Y_{\alpha\beta}$. For $\mathcal{O}(1)$ values of $Y_{\alpha\beta}$, $H^{\pm\pm}$ and $H^{\pm}$ decay primarily into $\ell^{\pm}\ell^{\pm}$ and $\ell^{\pm}\nu$ respectively, while the decay $H^{\pm} \to W^{\pm}\phi$ can still occur with a BR of $10\% - 20\%$ level, as shown in the left panels of Fig. 17, which is used for signal selection in this case.
- For our LHC analysis, we utilized the presence of the new source of missing energy from $\phi$ in the decays of $H^{\pm\pm}$ and $H^{\pm}$, and the BDT analysis can improve significantly the signal significance, in particular for the small Yukawa coupling case. At the HL-LHC, we found that for small and large $Y_{\alpha\beta}$, the $2\sigma$ ($5\sigma$) sensitivity reaches for $H^{\pm\pm}$ are respectively 800 (500) GeV and 1.1 (0.8) TeV (see Tables 9 and 11), as denoted by the solid lines in Figs. 24 and 27. These prospects are well above the current LHC constraints.
- At a future 100 TeV collider, the production cross section of $H^{\pm\pm}$ can be enhanced by over one order of magnitude in both pair production and associated production channels (see Fig. 20). Therefore the mass reaches of $H^{\pm\pm}$ can be largely improved via the observation of $\phi$ induced signals. For the small and large Yukawa coupling cases, the mass $M_{H^{\pm\pm}}$ can reach up to 3.8 (2.6) TeV and 4 (2.7) TeV respectively at the $2\sigma$ ($5\sigma$) significance (see Tables 9 and 11), as indicated by the dashed lines in Figs. 24 and 27.
- In the large Yukawa coupling scenario, the missing transverse energy is completely from the invisible light scalar $\phi$ at the parton level in the $pp \to H^{\pm\pm}H^{\mp} \to \mu^{\pm}\mu^{\pm} + 2j + E_T^{\rm miss}$ channel, and the mass $m_{\phi}$ can be determined with 10% accuracy at the LHC via the transverse mass distributions associated with jets and missing energy. This is demonstrated in Fig. 28.
- In the intermediate Yukawa coupling case with $|Y_{\alpha\beta}| = \mathcal{O}(10^{-2} - 1)$, the branching fractions of leptonic $\ell^{\pm}\ell^{\pm}$ and bosonic $W^{\pm}W^{\pm}\phi$ decays of $H^{\pm\pm}$ are comparable to each other, the doubly-charged scalar $H^{\pm\pm}$ can be searched at the future hadron colliders in the $H^{++}H^{--} \to \ell^{\pm}\ell^{\pm} + 4j + E_T^{\rm miss}$, $\ell^{\pm}\ell^{\pm}\ell^{\mp} + 2j + E_T^{\rm miss}$ and $\ell^{+}\ell^{+}\ell^{-}\ell^{-}$ channels. The

corresponding prospects of $H^{\pm\pm}$ depend largely on the leptonic branching fraction of $H^{\pm\pm}$ and the search channels. For the purpose of studying the leptonic scalar $\phi$ in the final state, the intermediate Yukawa coupling case can be most beneficial, from combining the leptonic and bosonic decay channels.

In this work, we have focused on the light leptonic scalar case with mass $M_h/2 < M_\phi \lesssim \mathcal{O}(100\,\text{GeV})$. It should be noted that the analysis in this chapter can be generalized to the cases with relatively heavier leptonic scalars $\phi$, say with masses of few hundreds of GeV or even larger. Then the $\phi$-induced signals will depend largely on the mass $M_\phi$. The light $\phi$ induced signal in this work can also be compared with the searches of $H^{\pm\pm}$ at future hadron colliders in the standard Type-II seesaw. For instance, the $H^{\pm\pm}$ mass reach has been estimated in the standard Type-II scenario for the LHC and future 100 TeV colliders in Refs. [152, 185]. In a large region of parameter space of Type-II seesaw, the bosonic decay channel $H^{\pm\pm} \to W^\pm W^\pm$ dominates, and the mass reach of $H^{\pm\pm}$ is found to be 1.8 TeV at $5\sigma$ at the 100 TeV collider, which is smaller than our reach of $\sim$2.6 TeV in both the large and small Yukawa coupling scenarios (cf. the dashed line in Figs. 24 and 27). The better reach in our model is due to the extra source of missing energy via $\phi$. This makes the signal in our model more easily distinguishable from the SM backgrounds.

## Appendix A Feynman rules in a UV-complete model with leptonic scalars

This appendix summarizes all the interaction vertices and their Feynman Rules for the model presented in Section 4.1. The model contains three CP-even scalars $h$, $H_1$, $H_2$; two CP-odd scalars $A_1$, $A_2$; the singly-charged scalars $H^{\pm}$; and the doubly-charged scalars $H^{\pm\pm}$. The component $h$ from the $SU(2)_L$-doublet is identified with the 125 GeV SM Higgs boson. In our convention, $H_1$ is lighter than $H_2$, and $A_1$ is lighter than $A_2$. The trilinear and quartic scalar couplings are collected in Tables 12 and 13 respectively, the trilinear and quartic gauge couplings are presented in Tables 14 and 15 respectively, and the Yukawa couplings can be found in Table 16.

Table 12: Trilinear scalar couplings.

| Vertices | Couplings |
|---|---|
| $H_1H_1h,\ A_1A_1h$ | $-i\left((\lambda_1+\lambda_4)\sin^2\theta+\lambda_6\cos^2\theta+\lambda_8\sin 2\theta\right)v$ |
| $H_2H_2h,\ A_2A_2h$ | $-i\left((\lambda_1+\lambda_4)\cos^2\theta+\lambda_6\sin^2\theta-\lambda_8\sin 2\theta\right)v$ |
| $H_1H_2h,\ A_1A_2h$ | $\frac{1}{2}i\left((\lambda_1+\lambda_4-\lambda_6)\sin 2\theta+2\lambda_8\cos 2\theta\right)v$ |
| $H^+H^-h$ | $-i\left(\lambda_1+\frac{1}{2}\lambda_4\right)v$ |
| $H^{++}H^{--}h$ | $-i\,\lambda_1 v$ |

Table 13: Quartic scalar couplings

| Vertices | Couplings |
|---|---|
| $hhH_1H_1,\ hhA_1A_1$ | $-i\left(\lambda_6\cos^2\theta-\lambda_8\sin 2\theta+(\lambda_1+\lambda_4)\sin^2\theta\right)$ |
| $hhH_2H_2,\ hhA_2A_2$ | $-i(\lambda_1\cos^2\theta+\lambda_4\cos^2\theta+\lambda_8\sin 2\theta+\lambda_6\sin^2\theta)$ |

| | |
|---|---|
| $hhH_2H_1,\ hhA_2A_1$ | $i\left(\lambda_8\cos 2\theta - \frac{1}{2}(\lambda_1+\lambda_4-\lambda_6)\sin 2\theta\right)$ |
| $H_1H_1H_1H_1,\ A_1A_1A_1A_1$ | $-6i(\lambda_5\cos^2\theta + \lambda_7\cos^2\theta\sin^2\theta + (\lambda_2+\lambda_3)\sin^4\theta)$ |
| $H_1H_1A_1A_1$ | $-2i\left(\lambda_5\cos^4\theta + \lambda_7\cos^2\theta\sin^2\theta + (\lambda_2+\lambda_3)\sin^4\theta\right)$ |
| $H_2H_2H_2H_2,\ A_2A_2A_2A_2$ | $-6i((\lambda_2+\lambda_3)\cos^4\theta + \lambda_7\cos^2\theta\sin^2\theta + \lambda_5\sin^4\theta)$ |
| $H_2H_2A_2A_2$ | $-2i((\lambda_2+\lambda_3)\cos^4\theta + \lambda_7\cos^2\theta\sin^2\theta + \lambda_5\sin^4\theta)$ |
| $H_1H_1H_1H_2,\ A_1A_1A_1A_2$ | $\frac{3}{2}i\left(-\lambda_2-\lambda_3+\lambda_5+(\lambda_2+\lambda_3+\lambda_5-\lambda_7)\cos 2\theta\right)\sin 2\theta$ |
| $H_1H_1H_2H_2,\ A_1A_1A_2A_2$ | $-\frac{1}{4}i\left(3(\lambda_2+\lambda_3+\lambda_5)+\lambda_7-3(\lambda_2+\lambda_3+\lambda_5-\lambda_7)\cos 4\theta\right)$ |
| $H_1H_2H_2H_2,\ A_1A_2A_2A_2$ | $-\frac{3}{2}i\left(\lambda_2+\lambda_3-\lambda_5+(\lambda_2+\lambda_3+\lambda_5-\lambda_7)\cos 2\theta\right)\sin 2\theta$ |
| $H_1H_1A_2A_2,\ H_2H_2A_1A_1$ | $-\frac{1}{4}i(\lambda_2+\lambda_3+\lambda_5+3\lambda_7-(\lambda_2+\lambda_3+\lambda_5-\lambda_7)\cos 4\theta)$ |
| $H_1H_2A_2A_2,\ H_2H_2A_1A_2$ | $-\frac{1}{2}i\left(\lambda_2+\lambda_3-\lambda_5+(\lambda_2+\lambda_3+\lambda_5-\lambda_7)\cos 2\theta\right)\sin 2\theta$ |
| $H_1H_1A_1A_2,\ H_1H_2A_1A_1$ | $\frac{1}{2}i\left(-\lambda_2-\lambda_3+\lambda_5+(\lambda_2+\lambda_3+\lambda_5-\lambda_7)\cos 2\theta\right)\sin 2\theta$ |
| $H_1H_2A_1A_2$ | $-\frac{1}{2}i\left(\lambda_2+\lambda_3+\lambda_5-\lambda_7\right)\sin^2 2\theta$ |
| $H^+H^-hh$ | $-i(\lambda_1+\frac{1}{2}\lambda_4)$ |
| $H^+H^-H_1H_1,\ H^+H^-A_1A_1$ | $-i\left(\lambda_7\cos^2\theta + 2(\lambda_2+\lambda_3)\sin^2\theta\right)$ |
| $H^+H^-H_2H_2,\ H^+H^-A_2A_2$ | $-i(2(\lambda_2+\lambda_3)\cos^2\theta + \lambda_7\sin^2\theta)$ |
| $H^+H^-H_1H_2,\ H^+H^-A_1A_2$ | $-i(\lambda_2+\lambda_3-\frac{1}{2}\lambda_7)\sin 2\theta$ |
| $H^+H^+H^-H^-$ | $-2i(2\lambda_2+\lambda_3)$ |
| $H^{++}H^{--}hh$ | $-i\lambda_1$ |
| $H^{++}H^{--}H_1H_1,\ H^{++}H^{--}A_1A_1$ | $-i\left(\lambda_7\cos^2\theta + 2\lambda_2\sin^2\theta\right)$ |
| $H^{++}H^{--}H_2H_2,\ H^{++}H^{--}A_2A_2$ | $-i(2\lambda_2\cos^2\theta + \lambda_7\sin^2\theta)$ |
| $H^{++}H^{--}H_1H_2,\ H^{++}H^{--}A_1A_2$ | $-i\left(\lambda_2-\frac{1}{2}\lambda_7\right)\sin 2\theta$ |
| $H^{++}H^-H^-H_1,\ H^{++}H^-H^-H_2$ | $\sqrt{2}i\lambda_3\sin\theta$ |
| $H^{++}H^-H^-A_1,\ H^{++}H^-H^-A_2$ | $\sqrt{2}\lambda_3\sin\theta$ |
| $H^{++}H^{--}H^+H^-$ | $-2i(\lambda_2+\lambda_3)$ |
| $H^{++}H^{++}H^{--}H^{--}$ | $-4i(\lambda_2+\lambda_3)$ |

Table 14: Trilinear gauge couplings. Here $p_1$, $p_2$ are the momenta of the first and second particles in the vertices.

| Vertices | Couplings |
|---|---|
| $A_1 H_1 Z_\mu$ | $\frac{g_L}{c_W}(p_1 - p_2)_\mu \sin^2\theta$ |
| $A_2 H_2 Z_\mu$ | $\frac{g_L}{c_W}(p_1 - p_2)_\mu \cos^2\theta$ |
| $A_1 H_2 Z_\mu,\ A_2 H_1 Z_\mu$ | $-\frac{g_L}{2\,c_W}(p_1 - p_2)_\mu \sin 2\theta$ |
| $H^+ H^- \gamma_\mu$ | $i\,e(p_1 - p_2)_\mu$ |
| $H^+ H^- Z_\mu$ | $-i\,e\frac{s_W}{c_W}(p_1 - p_2)_\mu$ |
| $H^+ H_1 W_\mu^-$ | $-i\,\frac{g_L}{\sqrt{2}}(p_1 - p_2)_\mu \sin\theta$ |
| $H^+ H_2 W_\mu^-$ | $i\,\frac{g_L}{\sqrt{2}}(p_1 - p_2)_\mu \cos\theta$ |
| $H^+ A_1 W_\mu^-$ | $-\frac{g_L}{\sqrt{2}}(p_1 - p_2)_\mu \sin\theta$ |
| $H^+ A_2 W_\mu^-$ | $\frac{g_L}{\sqrt{2}}(p_1 - p_2)_\mu \cos\theta$ |
| $H^{++} H^{--} \gamma_\mu$ | $2i\,e(p_1 - p_2)_\mu$ |
| $H^{++} H^{--} Z_\mu$ | $i\,e\frac{c_W^2 - s_W^2}{c_W s_W}(p_1 - p_2)_\mu$ |
| $H^{++} H^- W_\mu^-$ | $-i\,g_L(p_1 - p_2)_\mu$ |

Table 15: Quartic gauge couplings.

| Vertices | Couplings |
|---|---|
| $H_1H_1Z_\mu Z_\nu,\ A_1A_1Z_\mu Z_\nu$ | $2i\,\frac{g_L^2}{c_W^2}\sin^2\theta\, g_{\mu\nu}$ |
| $H_2H_2Z_\mu Z_\nu,\ A_2A_2Z_\mu Z_\nu$ | $2i\,\frac{g_L^2}{c_W^2}\cos^2\theta\, g_{\mu\nu}$ |
| $H_1H_2Z_\mu Z_\nu,\ A_1A_2Z_\mu Z_\nu$ | $-i\,\frac{g_L^2}{c_W^2}\sin 2\theta\, g_{\mu\nu}$ |
| $H_1H_1W_\mu^+W_\nu^-,\ A_1A_1W_\mu^-W_\nu^-$ | $i\,g_L^2\,\sin^2\theta\, g_{\mu\nu}$ |
| $H_2H_2W_\mu^+W_\nu^-,\ A_2A_2W_\mu^+W_\nu^-$ | $i\,g_L^2\,\cos^2\theta\, g_{\mu\nu}$ |
| $H_1H_2W_\mu^+W_\nu^-,\ A_1A_2W_\mu^+W_\nu^-$ | $-\frac{1}{2}i\,g_L^2\,\sin 2\theta\, g_{\mu\nu}$ |
| $H^+H^-\gamma_\mu\gamma_\nu$ | $2i\,e^2 g_{\mu\nu}$ |
| $H^+H^-Z_\mu Z_\nu$ | $2i\,e^2\,\frac{s_W^2}{c_W^2}\,g_{\mu\nu}$ |
| $H^+H^-Z_\mu\gamma_\nu$ | $-2i\,e^2\,\frac{s_W}{c_W}g_{\mu\nu}$ |
| $H^+H^-W_\mu^+W_\nu^-$ | $2i\,g_L^2\,g_{\mu\nu}$ |
| $H^+H_1W_\mu^-\gamma_\nu$ | $-i\,\frac{e^2}{\sqrt{2}s_W}\,\sin\theta\, g_{\mu\nu}$ |
| $H^+H_2W_\mu^-\gamma_\nu$ | $i\,\frac{e^2}{\sqrt{2}s_W}\,\cos\theta\, g_{\mu\nu}$ |
| $H^+A_1W_\mu^-\gamma_\nu$ | $-\frac{e^2}{\sqrt{2}s_W}\,\sin\theta\, g_{\mu\nu}$ |
| $H^+A_2W_\mu^-\gamma_\nu$ | $\frac{e^2}{\sqrt{2}s_W}\,\cos\theta\, g_{\mu\nu}$ |
| $H^+H_1W_\mu^-Z_\nu$ | $i\,\frac{e^2}{\sqrt{2}\,c_W}\left(2+\frac{c_W^2}{s_W^2}\right)\sin\theta\, g_{\mu\nu}$ |
| $H^+H_2W_\mu^-Z_\nu$ | $-i\,\frac{e^2}{\sqrt{2}\,c_W}\left(2+\frac{c_W^2}{s_W^2}\right)\cos\theta\, g_{\mu\nu}$ |
| $H^+A_1W_\mu^-Z_\nu$ | $\frac{e^2}{\sqrt{2}\,c_W}\left(2+\frac{c_W^2}{s_W^2}\right)\sin\theta\, g_{\mu\nu}$ |
| $H^+A_2W_\mu^-Z_\nu$ | $-\frac{e^2}{\sqrt{2}\,c_W}\left(2+\frac{c_W^2}{s_W^2}\right)\cos\theta\, g_{\mu\nu}$ |
| $H^{++}H^{--}\gamma_\mu\gamma_\nu$ | $8i\,e^2 g_{\mu\nu}$ |
| $H^{++}H^{--}Z_\mu Z_\nu$ | $2i\,g_L^2\,\frac{(c_W^2-s_W^2)^2}{c_W^2}\,g_{\mu\nu}$ |

| | |
|---|---|
| $H^{++}H^{--}Z_\mu\gamma_\nu$ | $4i\,e^2\,\dfrac{c_W^2-s_W^2}{c_W\,s_W}g_{\mu\nu}$ |
| $H^{++}H^{--}W_\mu^+W_\nu^-$ | $i\,g_L^2\,g_{\mu\nu}$ |
| $H^{++}H_1W_\mu^-W_\nu^-$ | $\sqrt{2}ig_L^2\,\sin\theta\,g_{\mu\nu}$ |
| $H^{++}H_2W_\mu^-W_\nu^-$ | $-\sqrt{2}ig_L^2\,\cos\theta\,g_{\mu\nu}$ |
| $H^{++}A_1W_\mu^-W_\nu^-$ | $\sqrt{2}g_L^2\,\sin\theta\,g_{\mu\nu}$ |
| $H^{++}A_2W_\mu^-W_\nu^-$ | $-\sqrt{2}g_L^2\,\cos\theta\,g_{\mu\nu}$ |
| $H^{++}H^-W_\mu^-\gamma_\nu$ | $-3i\,\dfrac{e^2}{s_W}\,g_{\mu\nu}$ |
| $H^{++}H^-W_\mu^-Z_\nu$ | $i\,\dfrac{e^2}{c_W}\left(2+\dfrac{c_W^2}{s_W^2}\right)\,g_{\mu\nu}$ |

Table 16: Yukawa couplings.

| Vertices | Couplings |
|---|---|
| $H^{++}l_\alpha^-l_\beta^-$ | $2i\,Y_{\alpha\beta}\,P_L$ |
| $H^+l_\alpha^-v_\beta$ | $\sqrt{2}i\,Y_{\alpha\beta}\,P_L$ |
| $H_2\nu_\alpha\nu_\beta$ | $-\sqrt{2}i\,Y_{\alpha\beta}\,P_L\,\cos\theta$ |
| $H_1\nu_\alpha\nu_\beta$ | $-\sqrt{2}i\,Y_{\alpha\beta}\,P_L\,\sin\theta$ |
| $A_2\nu_\alpha\nu_\beta$ | $\sqrt{2}\,Y_{\alpha\beta}\,P_L\,\cos\theta$ |
| $A_1\nu_\alpha\nu_\beta$ | $\sqrt{2}\,Y_{\alpha\beta}\,P_L\,\sin\theta$ |

## Appendix B The functions $G$ and $\mathcal{F}$ in heavy Higgs decays

For the decays in Eq. (4.18), the function $G(x,y)$ is given by

$$\begin{aligned} G(x,y) &= \frac{1}{12y}\Bigg\{2(-1+x)^3 - 9(-1+x^2)y + 6(-1+x)y^2 \\ &\quad +6(1+x-y)y\sqrt{-\lambda(x,y)}\left[\arctan\left(\frac{-1+x-y}{\sqrt{-\lambda(x,y)}}\right) + \arctan\left(\frac{-1+x+y}{\sqrt{-\lambda(x,y)}}\right)\right] \\ &\quad -3y\Big[1+(x-y)^2-2y\Big]\log x\Bigg\}. \end{aligned} \tag{B.1}$$

For the decays in Eq. (4.20), the function $\mathcal{F}$ is defined as

$$\begin{aligned} F &= 4 + \frac{1}{2}(x-2)^2 \\ &\quad +\frac{1}{2(y-u)^2}\left[(y-1)^2 - 2r(y+1) + r^2\right]\left[(y-1)^2 - 2w(y+1) + w^2\right] \\ &\quad +\frac{1}{2(z-u)^2}\left[(z-1)^2 - 2r(z+1) + r^2\right]\left[(z-1)^2 - 2w(z+1) + w^2\right] \\ &\quad +\frac{1}{(y-u)(z-u)}\left[(y-r)(z-w) + (y+z+r+w-3)\right] \\ &\quad \times\left[(z-r)(y-w) + (y+z+r+w-3)\right] \\ &\quad -\frac{1}{y-u}\left[(x-2)(y-r-1)(y-w+1)\right. \\ &\quad \left.+2(y-r-1)^2 + 2(z-r-1)^2 + 2(x-2)(z-r-1) - 8r\right] \\ &\quad -\frac{1}{z-u}\left[(x-2)(z-r-1)(z-w+1)\right. \\ &\quad \left.+2(y-r-1)^2 + 2(z-r-1)^2 + 2(x-2)(y-r-1) - 8r\right], \end{aligned} \tag{B.2}$$

where we have defined

$$x \equiv \frac{m_{12}^2}{M_W^2}, \quad y \equiv \frac{m_{23}^2}{M_W^2}, \quad z \equiv \frac{m_{13}^2}{M_W^2}, \quad r \equiv \frac{m_\phi^2}{M_W^2}, \quad u \equiv \frac{M_{H^\pm}^2}{M_W^2}, \quad w \equiv \frac{M_{H^{\pm\pm}}^2}{M_W^2}. \tag{B.3}$$

## Appendix C One-loop RGEs

In this appendix, we list the $\beta$-functions for all the one-loop RGEs for the gauge couplings, quartic couplings and Yukawa couplings in our model. These were obtained using the `PyR@TE` package [212, 213]. For simplicity, we keep only the Yukawa coupling $Y_{\mu\mu}$ in the matrix $Y_{\alpha\beta}$. The gauge coupling $g_Y$ is normalized to be $g_1 = \sqrt{3/5} g_Y$ [214].

$$(4\pi)^2 \beta_{g_S} = -7 g_S^3 \,, \tag{C.1}$$

$$(4\pi)^2 \beta_{g_L} = -\frac{5}{2} g_L^3 \,, \tag{C.2}$$

$$(4\pi)^2 \beta_{g_1} = +\frac{47}{6} g_1^3 \,, \tag{C.3}$$

$$\begin{aligned}(4\pi)^2 \beta_\lambda = {} & \frac{3}{2}\left(3g_L^4 + 2g_1^2 g_L^2 + g_1^4\right) + 6\lambda^2 + 12\lambda_1^2 + 5\lambda_4^2 + 4\lambda_6^2 + 8\lambda_8^2 + 12\lambda_1\lambda_4 \\ & - 24 y_t^4 - 3\lambda\left(3g_L^2 + g_1^2\right) + 12\lambda y_t^2 \,,\end{aligned} \tag{C.4}$$

$$\begin{aligned}(4\pi)^2 \beta_{\lambda_1} = {} & 3\left(2g_L^4 - 2g_1^2 g_L^2 + g_1^4\right) + 4\lambda_1^2 + \lambda_4^2 + 3\lambda\lambda_1 + \lambda\lambda_4 + 16\lambda_1\lambda_2 + 12\lambda_1\lambda_3 \\ & + 6\lambda_2\lambda_4 + 2\lambda_3\lambda_4 + 2\lambda_6\lambda_7 - \frac{3}{2}\lambda_1\left(11g_L^2 + 5g_1^2\right) \\ & + 2\lambda_1\left(3y_t^2 + 2\left|Y_{\mu\mu}\right|^2\right) \,,\end{aligned} \tag{C.5}$$

$$\begin{aligned}(4\pi)^2 \beta_{\lambda_2} = {} & 3\left(5g_L^4 - 4g_1^2 g_L^2 + 2g_1^4\right) + 2\lambda_1^2 + 28\lambda_2^2 + 6\lambda_3^2 + \lambda_7^2 + 2\lambda_1\lambda_4 + 24\lambda_2\lambda_3 \\ & - 12\lambda_2\left(2g_L^2 + g_1^2\right) + 8\lambda_2\left|Y_{\mu\mu}\right|^2 \,,\end{aligned} \tag{C.6}$$

$$\begin{aligned}(4\pi)^2 \beta_{\lambda_3} = {} & -6g_L^2\left(g_L^2 - 4g_1^2\right) + 18\lambda_3^2 + \lambda_4^2 + 24\lambda_2\lambda_3 - 16\left|Y_{\mu\mu}\right|^4 \\ & - 12\lambda_3\left(2g_L^2 + g_1^2\right) + 8\lambda_3\left|Y_{\mu\mu}\right|^2 \,,\end{aligned} \tag{C.7}$$

$$\begin{aligned}(4\pi)^2 \beta_{\lambda_4} = {} & 12 g_1^2 g_L^2 + 4\lambda_4^2 + 8\lambda_8^2 + \lambda\lambda_4 + 8\lambda_1\lambda_4 + 4\lambda_2\lambda_4 + 8\lambda_3\lambda_4 \\ & - \frac{3}{2}\lambda_4\left(11g_L^2 + 5g_1^2\right) + 2\lambda_4\left(3y_t^2 + 2\left|Y_{\mu\mu}\right|^2\right) \,,\end{aligned} \tag{C.8}$$

$$(4\pi)^2 \beta_{\lambda_5} = 20\lambda_5^2 + 2\lambda_6^2 + 3\lambda_7^2 \,, \tag{C.9}$$

$$\begin{aligned}(4\pi)^2 \beta_{\lambda_6} = {} & 4\lambda_6^2 + 12\lambda_8^2 + 3\lambda\lambda_6 + 6\lambda_1\lambda_7 + 8\lambda_5\lambda_6 + 3\lambda_4\lambda_7 \\ & - \frac{3}{2}\lambda_6\left(3g_L^2 + g_1^2\right) + 6\lambda_6 y_t^2 \,,\end{aligned} \tag{C.10}$$

$$\begin{aligned}(4\pi)^2 \beta_{\lambda_7} = {} & 4\lambda_7^2 + 4\lambda_8^2 + 4\lambda_1\lambda_6 + 16\lambda_2\lambda_7 + 12\lambda_3\lambda_7 + 2\lambda_4\lambda_6 + 8\lambda_5\lambda_7 \\ & - 6\lambda_7\left(2g_L^2 + g_1^2\right) + 4\lambda_7\left|Y_{\mu\mu}\right|^2 \,,\end{aligned} \tag{C.11}$$

$$(4\pi)^2\beta_{\lambda_8} = \lambda\lambda_8 + 4\lambda_1\lambda_8 + 6\lambda_4\lambda_8 + 4\lambda_6\lambda_8 + 2\lambda_7\lambda_8 \\ - \frac{3}{2}\lambda_8\left(7g_L^2 + 3g_1^2\right) + 2\lambda_8\left(3y_t^2 + |Y_{\mu\mu}|^2\right) , \tag{C.12}$$

$$(4\pi)^2\beta_{y_t} = \frac{9}{2}y_t^3 - y_t\left(8g_S^2 + \frac{9}{4}g_L^2 + \frac{17}{12}g_1^2\right) , \tag{C.13}$$

$$(4\pi)^2\beta_{Y_{\mu\mu}} = 8\,|Y_{\mu\mu}|^2\,Y_{\mu\mu} - \frac{3}{2}Y_{\mu\mu}\left(3g_L^2 + g_1^2\right) . \tag{C.14}$$

## Appendix D Analytical perturbativity limits

For the gauge couplings $g_i$, it is trivial to get the analytical one-loop expressions for the couplings, which turn out to be

$$\alpha_i(\mu) = \frac{\alpha_i(v)}{1 - \frac{b_i}{2\pi}\alpha_i(v)\log(\mu/v)}\,, \tag{D.1}$$

with $\alpha_3 = g_S^2/4\pi$, $\alpha_2 = g_L^2/4\pi$, $\alpha_1 = g_1^2/4\pi$ for the $SU(3)_c$, $SU(2)_L$ and $U(1)_Y$ couplings respectively, and $b_3 = -7$, $b_2 = -5/2$, $b_1 = 47/6$ [cf. Eqs. ( C.1)-( C.3)]. For the SM top-quark Yukawa coupling $y_t$, let us first consider only the $y_t^3$ and $g_S^2 y_t$ terms on the RHS of Eq. ( C.13), *i.e.*:

$$(4\pi)^2 \frac{\mathrm{d}}{\mathrm{d}t} y_t \;=\; \frac{9}{2} y_t^3 - 8 g_S^2 y_t\,. \tag{D.2}$$

To implement the running of $g_S$, we rewrite the equation above to be in the form of

$$\begin{aligned} 8\pi^2 \left[\frac{1}{y_t^2}\frac{\mathrm{d}}{\mathrm{d}t} y_t^2 + \frac{8}{b_3}\frac{1}{\alpha_3}\frac{\mathrm{d}}{\mathrm{d}t}\alpha_3\right] &= \frac{9}{2} y_t^3\,, \\ \text{or,}\quad 8\pi^2 \frac{\mathrm{d}}{\mathrm{d}t} \log\left(y_t^2 \alpha_3^{8/b_3}\right) &= \frac{9}{2} y_t^2\,. \end{aligned} \tag{D.3}$$

Then we can obtain the analytical running of $y_t$:

$$y_t^2(\mu) \simeq y_t^2(v) \left(\frac{\alpha_3(v)}{\alpha_3(\mu)}\right)^{8/b_3} \left[1 - \frac{9}{16\pi^2} y_t^2(v) \alpha_3^{8/b_3}(v) \int_0^t \mathrm{d}t'\, \alpha_3^{-8/b_3}(t')\right]^{-1}\,. \tag{D.4}$$

If we include also the $g_L^2 y_t$ and $g_1^2 y_t$ terms in Eq. ( C.13), it is straightforward to get the full analytical one-loop solution for $y_t$:

$$y_t^2(\mu) = y_t^2(v) \left(\frac{E_\alpha(v)}{E_\alpha(\mu)}\right) \left[1 - \frac{9}{16\pi^2} y_t^2(v) E_\alpha(v) \int_0^t \mathrm{d}t'\, E_\alpha^{-1}(t')\right]^{-1}\,, \tag{D.5}$$

where the function

$$E_\alpha(\mu) = \alpha_3^{8/b_3}(\mu) \alpha_2^{9/4b_2}(\mu) \alpha_1^{17/12b_1}(\mu)\,. \tag{D.6}$$

In the one-loop RGE of $Y_{\mu\mu}$ in Eq. ( C.14), if we consider only the $Y_{\mu\mu}^3$ term on the RHS, it is trivial to obtain

$$\alpha_\mu(\mu) = \frac{\alpha_\mu(v)}{1 - \frac{4}{\pi}\alpha_\mu(v)t}\,, \tag{D.7}$$

where $\alpha_\mu \equiv Y_{\mu\mu}^2/4\pi$. It is clear that the coupling $Y_{\mu\mu}$ will blow up when the $t$ parameter approaches the value of

$$t_c = \log\left(\frac{\mu_c}{v}\right) = \frac{\pi^2}{Y_{\mu\mu}^2(v)}\,. \tag{D.8}$$

With an initial value of $Y_{\mu\mu}(v) = 1.5$, we can get the critical value of $t_c \simeq 4.39$. As in Eq. ( D.2), we can first include the gauge coupling $g_L$, then

$$Y_{\mu\mu}^2(\mu) \simeq Y_{\mu\mu}^2(v)\left(\frac{\alpha_2(v)}{\alpha_2(\mu)}\right)^{9/2b_2}\left[1 - \frac{1}{\pi^2}Y_{\mu\mu}^2(v)\alpha_2^{9/2b_2}(v)\int_0^t \mathrm{d}t'\,\alpha_2^{-9/2b_2}(t')\right]^{-1}\,. \tag{D.9}$$

In this case, the coupling $g_L$ becomes divergent when the parameter $t_c = 4.62$. If we have all the terms on the RHS of Eq. ( C.14), it turns out that

$$\begin{aligned} Y_{\mu\mu}^2(\mu) &= Y_{\mu\mu}^2(v)\left(\frac{\alpha_2(v)}{\alpha_2(\mu)}\right)^{9/2b_2}\left(\frac{\alpha_1(v)}{\alpha_1(\mu)}\right)^{3/2b_1} \\ &\times\left[1 - \frac{1}{\pi^2}Y_{\mu\mu}^2(v)\alpha_2^{9/2b_2}(v)\alpha_1^{3/2b_1}(v)\int_0^t \mathrm{d}t'\,\alpha_2^{-9/2b_2}(t')\alpha_1^{-3/2b_1}(t')\right]^{-1}\,. \end{aligned} \tag{D.10}$$

In this case, the critical value $t_c = 4.67$.

We also show the analytical solution of $\lambda_8(\mu)$ below:

$$\lambda_8(\mu) = \lambda_8(v)\exp\left\{\frac{1}{4\pi^2}\int_v^\mu E_8(\mu)d\mu\right\}\,, \tag{D.11}$$

where

$$\begin{aligned} E_8(\mu) &= 3y_t(v)^2\left(1 - \frac{\mu b_3\alpha_3(v)}{2\pi}\right)^{8/b_3} - \alpha_\mu(v)\left(1 - \frac{4\mu\alpha_\mu(v)}{\pi}\right)^{-1} \\ &- \frac{21}{2}\alpha_2(v)\left(1 - \frac{\mu b_2\alpha_2(v)}{2\pi}\right)^{-1} - \frac{9}{2}\alpha_1(v)\left(1 + \frac{\mu b_1\alpha_1(v)}{2\pi}\right)^{-1}\,. \end{aligned} \tag{D.12}$$

These results agree well with the full numerical results shown in Fig. 19.

## Appendix E Partial wave unitarity bounds

We assume all the heavy Higgs bosons in our model are of order TeV in mass. The scattering amplitudes are well-behaved at high energies. The unitarity constraints on amplitudes are only reflected on the quartic coupling strengths. Following the analysis for the Type-II seesaw model [215], the unitarity bounds in our model can be found by diagonalizing the sub-matrices $\mathcal{M}_i$ which correspond to the coefficients for $2 \leftrightarrow 2$ scalar scattering processes. Writing the scalar multiplets explicitly as

$$H = \begin{pmatrix} h^{\pm} \\ \frac{1}{\sqrt{2}}(h + iZ_1) \end{pmatrix}, \quad \Delta = \begin{pmatrix} \frac{1}{\sqrt{2}}\delta^{+} & \delta^{++} \\ \frac{1}{\sqrt{2}}(\xi + iZ_2) & -\frac{1}{\sqrt{2}}\delta^{+} \end{pmatrix}, \quad \Phi = \frac{1}{\sqrt{2}}(s + iZ_3), \tag{E.1}$$

the sub-matrices for the initial and final states ($h\xi$, $hs$, $Z_1Z_2$, $Z_1Z_3$, $hZ_2$, $hZ_3$, $\xi Z_1$, $sZ_1$, $h^+\delta^-$, $\delta^+h^-$) and ($\xi s$, $Z_2Z_3$, $\xi Z_3$, $sZ_3$) respectively are

$$\mathcal{M}_1 = \begin{pmatrix}
\lambda_{14} & -\lambda_8 & 0 & \lambda_8 & 0 & 0 & 0 & 0 & \frac{\lambda_4}{2\sqrt{2}} & \frac{\lambda_4}{2\sqrt{2}} \\
-\lambda_8 & \lambda_6 & -\lambda_8 & 0 & 0 & 0 & 0 & 0 & -\frac{\lambda_8}{\sqrt{2}} & -\frac{\lambda_8}{\sqrt{2}} \\
0 & -\lambda_8 & \lambda_{14} & \lambda_8 & 0 & 0 & 0 & 0 & \frac{\lambda_4}{2\sqrt{2}} & \frac{\lambda_4}{2\sqrt{2}} \\
\lambda_8 & 0 & \lambda_8 & \lambda_6 & 0 & 0 & 0 & 0 & \frac{\lambda_8}{\sqrt{2}} & \frac{\lambda_8}{\sqrt{2}} \\
0 & 0 & 0 & 0 & \lambda_{14} & -\lambda_8 & 0 & -\lambda_8 & -\frac{i\lambda_4}{2\sqrt{2}} & -\frac{i\lambda_4}{2\sqrt{2}} \\
0 & 0 & 0 & 0 & -\lambda_8 & \lambda_6 & \lambda_8 & 0 & \frac{i\lambda_8}{\sqrt{2}} & \frac{i\lambda_8}{\sqrt{2}} \\
0 & 0 & 0 & 0 & 0 & \lambda_8 & \lambda_{14} & \lambda_8 & \frac{i\lambda_4}{2\sqrt{2}} & \frac{i\lambda_4}{2\sqrt{2}} \\
0 & 0 & 0 & 0 & -\lambda_8 & 0 & \lambda_8 & \lambda_6 & \frac{i\lambda_8}{\sqrt{2}} & -\frac{i\lambda_8}{\sqrt{2}} \\
\frac{\lambda_4}{2\sqrt{2}} & -\frac{\lambda_8}{\sqrt{2}} & \frac{\lambda_4}{2\sqrt{2}} & \frac{\lambda_8}{\sqrt{2}} & \frac{i\lambda_4}{2\sqrt{2}} & -\frac{i\lambda_8}{\sqrt{2}} & -\frac{i\lambda_4}{2\sqrt{2}} & -\frac{i\lambda_8}{\sqrt{2}} & \lambda'_{14} & 0 \\
\frac{\lambda_4}{2\sqrt{2}} & -\frac{\lambda_8}{\sqrt{2}} & \frac{\lambda_4}{2\sqrt{2}} & \frac{\lambda_8}{\sqrt{2}} & -\frac{i\lambda_4}{2\sqrt{2}} & \frac{i\lambda_8}{\sqrt{2}} & \frac{i\lambda_4}{2\sqrt{2}} & \frac{i\lambda_8}{\sqrt{2}} & 0 & \lambda'_{14}
\end{pmatrix}, \tag{E.2}$$

$$\mathcal{M}_2 = \begin{pmatrix}
\lambda_7 & 0 & 0 & 0 \\
0 & \lambda_7 & 0 & 0 \\
0 & 0 & \lambda_7 & 0 \\
0 & 0 & 0 & \lambda_7
\end{pmatrix}, \tag{E.3}$$

where we have defined the combinations of quartic couplings:

$$\lambda_{ij} \equiv \lambda_i + \lambda_j \,, \qquad \lambda'_{ij} \equiv \lambda_i + \frac{1}{2}\lambda_j \,. \tag{E.4}$$

The eigenvalues are

$$\lambda_{1,\,6,\,7} \,, \quad \lambda_1 + \lambda_4 \,, \quad \lambda^{\pm}_{146} \,, \tag{E.5}$$

with

$$\lambda^{\pm}_{146} \equiv \frac{1}{4}\left[(2\lambda_1 + 3\lambda_4 + 2\lambda_6) \pm \sqrt{(2\lambda_1 + 3\lambda_4 - 2\lambda_6)^2 + 96\lambda_8^2}\right] . \tag{E.6}$$

For the states ($\frac{1}{\sqrt{2}}hh$, $\frac{1}{\sqrt{2}}\xi\xi$, $\frac{1}{\sqrt{2}}ss$, $\frac{1}{\sqrt{2}}Z_1Z_1$, $\frac{1}{\sqrt{2}}Z_2Z_2$, $\frac{1}{\sqrt{2}}Z_3Z_3$, $h^+h^-$, $\delta^+\delta^-$, $\delta^{++}\delta^{--}$) with factor of $1/\sqrt{2}$ accounting for the identical particles, the sub-matrix is

$$\mathcal{M}_3 = \begin{pmatrix}
\frac{3\lambda}{4} & \frac{\lambda_{14}}{2} & \frac{\lambda_6}{2} & \frac{\lambda}{4} & \frac{\lambda_{14}}{2} & \frac{\lambda_6}{2} & \frac{\lambda}{2\sqrt{2}} & \frac{\lambda'_{14}}{\sqrt{2}} & \frac{\lambda_1}{\sqrt{2}} \\
\frac{\lambda_{14}}{2} & 3\lambda_{23} & \frac{\lambda_7}{2} & \frac{\lambda_{14}}{2} & \lambda_{23} & \frac{\lambda_7}{2} & \frac{\lambda_1}{\sqrt{2}} & \sqrt{2}\lambda_{23} & \sqrt{2}\lambda_2 \\
\frac{\lambda_6}{2} & \frac{\lambda_7}{2} & 3\lambda_5 & \frac{\lambda_6}{2} & \frac{\lambda_7}{2} & \lambda_5 & \frac{\lambda_6}{\sqrt{2}} & \frac{\lambda_7}{\sqrt{2}} & \frac{\lambda_7}{\sqrt{2}} \\
\frac{\lambda}{4} & \frac{\lambda_{14}}{2} & \frac{\lambda_6}{2} & \frac{3\lambda}{4} & \frac{\lambda_{14}}{2} & \frac{\lambda_6}{2} & \frac{\lambda}{2\sqrt{2}} & \frac{\lambda'_{14}}{\sqrt{2}} & \frac{\lambda_1}{\sqrt{2}} \\
\frac{\lambda_{14}}{2} & \lambda_{23} & \frac{\lambda_7}{2} & \frac{\lambda_{14}}{2} & 3\lambda_{23} & \frac{\lambda_7}{2} & \frac{\lambda_1}{\sqrt{2}} & \sqrt{2}\lambda_{23} & \sqrt{2}\lambda_2 \\
\frac{\lambda_6}{2} & \frac{\lambda_7}{2} & \lambda_5 & \frac{\lambda_6}{2} & \frac{\lambda_7}{2} & 3\lambda_5 & \frac{\lambda_6}{\sqrt{2}} & \frac{\lambda_7}{\sqrt{2}} & \frac{\lambda_7}{\sqrt{2}} \\
\frac{\lambda}{2\sqrt{2}} & \frac{\lambda_1}{\sqrt{2}} & \frac{\lambda_6}{\sqrt{2}} & \frac{\lambda}{2\sqrt{2}} & \frac{\lambda_1}{\sqrt{2}} & \frac{\lambda_6}{\sqrt{2}} & \lambda & \lambda'_{14} & \lambda_{14} \\
\frac{\lambda'_{14}}{\sqrt{2}} & \sqrt{2}\lambda_{23} & \frac{\lambda_7}{\sqrt{2}} & \frac{\lambda'_{14}}{\sqrt{2}} & \sqrt{2}\lambda_{23} & \frac{\lambda_7}{\sqrt{2}} & \lambda'_{14} & 4\lambda'_{23} & 2\lambda_{23} \\
\frac{\lambda_1}{\sqrt{2}} & \sqrt{2}\lambda_2 & \frac{\lambda_7}{\sqrt{2}} & \frac{\lambda_1}{\sqrt{2}} & \sqrt{2}\lambda_2 & \frac{\lambda_7}{\sqrt{2}} & \lambda_{14} & 2\lambda_{23} & 4\lambda_{23}
\end{pmatrix} , \tag{E.7}$$

and the eigenvalues are

$$\frac{1}{2}\lambda \,, \quad 2\lambda_{2,\,5} \,, \quad 2(\lambda_2 + \lambda_3) \,, \quad \lambda_{023} \,, \quad x_{1,\,2,\,3} \,, \tag{E.8}$$

with

$$\lambda_{023} \equiv \frac{1}{4}\left[(\lambda + 4\lambda_2 + 8\lambda_3) \pm \sqrt{(\lambda - 4\lambda_2 - 8\lambda_3)^2 + 16\lambda_4^2}\right] \tag{E.9}$$

and $x_{1,2,3}$ are the roots of the equation

$$
\begin{aligned}
&x^3 - 2x^2\left(3\lambda + 16\lambda_2 + 12\lambda_3 + 8\lambda_5\right) \\
&+8x\left[6\lambda(4\lambda_2 + 3\lambda_3 + 2\lambda_5) - 3(2\lambda_1 + \lambda_4)^2 + 64\lambda_2\lambda_5 + 48\lambda_3\lambda_5 - 4\lambda_6^2 - 6\lambda_7^2\right] \\
&+32\left[9\lambda\lambda_7^2 + 12\lambda_5(-2\lambda(4\lambda_2 + 3\lambda_3) + (2\lambda_1 + \lambda_4)^2) + 8\lambda_6^2(4\lambda_2 + 3\lambda_3) - 12\lambda_6\lambda_7(2\lambda_1 + \lambda_4)\right] = 0\,.
\end{aligned}
\tag{E.10}
$$

The sub-matrix for the states ($hZ_1$, $\xi Z_2$, $sZ_3$) is

$$
\mathcal{M}_4 = \begin{pmatrix} \frac{1}{2}\lambda & 0 & 0 \\ 0 & 2(\lambda_2 + \lambda_3) & 0 \\ 0 & 0 & 2\lambda_5 \end{pmatrix}\,, \tag{E.11}
$$

whose eigenvalues are

$$
\frac{1}{2}\lambda\,, \quad 2(\lambda_2 + \lambda_3)\,, \quad 2\lambda_5\,. \tag{E.12}
$$

The sub-matrix for ($hh^+$, $\xi h^+$, $sh^+$, $Z_1h^+$, $Z_2h^+$, $Z_3h^+$, $h\delta^+$, $\xi\delta^+$, $s\delta^+$, $Z_1\delta^+$, $Z_2\delta^+$, $Z_3\delta^+$, $\delta^{++}h^-$, $\delta^{++}\delta^-$) is

$$
\mathcal{M}_5 = \begin{pmatrix}
\frac{\lambda}{2} & 0 & 0 & 0 & 0 & 0 & 0 & \frac{\lambda_4}{2\sqrt{2}} & -\frac{\lambda_8}{\sqrt{2}} & 0 & \frac{i\lambda_4}{2\sqrt{2}} & -\frac{i\lambda_8}{\sqrt{2}} & 0 & -\frac{\lambda_4}{2} \\
0 & \lambda_1 & 0 & 0 & 0 & 0 & 0 & 0 & 0 & 0 & 0 & 0 & -\frac{\lambda_8}{\sqrt{2}} & -\frac{\lambda_8}{\sqrt{2}} \\
0 & 0 & \lambda_6 & 0 & 0 & 0 & -\frac{\lambda_8}{\sqrt{2}} & 0 & 0 & -\frac{i\lambda_8}{\sqrt{2}} & 0 & 0 & \sqrt{2}\lambda_8 & 0 \\
0 & 0 & 0 & \frac{\lambda}{2} & 0 & 0 & 0 & -\frac{i\lambda_4}{2\sqrt{2}} & -\frac{i\lambda_8}{\sqrt{2}} & 0 & \frac{\lambda_4}{2\sqrt{2}} & \frac{\lambda_8}{\sqrt{2}} & 0 & \frac{i\lambda_4}{2} \\
0 & 0 & 0 & 0 & \lambda_1 & 0 & \frac{i\lambda_4}{2\sqrt{2}} & 0 & 0 & \frac{\lambda_4}{2\sqrt{2}} & 0 & 0 & 0 & 0 \\
0 & 0 & 0 & 0 & 0 & \lambda_6 & -\frac{i\lambda_8}{\sqrt{2}} & 0 & 0 & \frac{\lambda_8}{\sqrt{2}} & 0 & 0 & \sqrt{2}i\lambda_8 & 0 \\
0 & \frac{\lambda_4}{2\sqrt{2}} & -\frac{\lambda_8}{\sqrt{2}} & 0 & -\frac{i\lambda_4}{2\sqrt{2}} & \frac{i\lambda_8}{\sqrt{2}} & \lambda'_{14} & 0 & 0 & 0 & 0 & 0 & -\frac{\lambda_4}{2} & 0 \\
\frac{\lambda_4}{2\sqrt{2}} & 0 & 0 & \frac{i\lambda_4}{2\sqrt{2}} & 0 & 0 & 0 & 2\lambda_{23} & 0 & 0 & 0 & 0 & 0 & -\sqrt{2}\lambda_3 \\
-\frac{\lambda_8}{\sqrt{2}} & 0 & 0 & \frac{i\lambda_8}{\sqrt{2}} & 0 & 0 & 0 & 0 & \lambda_7 & 0 & 0 & 0 & 0 & 0 \\
0 & \frac{i\lambda_4}{2\sqrt{2}} & \frac{i\lambda_8}{\sqrt{2}} & 0 & \frac{\lambda_4}{2\sqrt{2}} & \frac{\lambda_8}{\sqrt{2}} & 0 & 0 & 0 & \lambda'_{14} & 0 & 0 & \frac{i\lambda_4}{2} & 0 \\
-\frac{i\lambda_4}{2\sqrt{2}} & 0 & 0 & \frac{\lambda_4}{2\sqrt{2}} & 0 & 0 & 0 & 0 & 0 & 0 & 2\lambda_{23} & 0 & 0 & \sqrt{2}i\lambda_3 \\
\frac{i\lambda_8}{\sqrt{2}} & 0 & 0 & \frac{\lambda_8}{\sqrt{2}} & 0 & 0 & 0 & 0 & 0 & 0 & 0 & \lambda_7 & 0 & 0 \\
0 & 0 & \sqrt{2}\lambda_8 & 0 & 0 & -\sqrt{2}i\lambda_8 & -\frac{\lambda_4}{2} & 0 & 0 & -\frac{i\lambda_4}{2} & 0 & 0 & \lambda_{14} & 0 \\
-\frac{\lambda_4}{2} & 0 & 0 & -\frac{i\lambda_4}{2} & 0 & 0 & 0 & -\sqrt{2}\lambda_3 & 0 & 0 & -\sqrt{2}i\lambda_3 & 0 & 0 & 2\lambda_{23}
\end{pmatrix}\,, \tag{E.13}
$$

and the eigenvalues are

$$\lambda_1\,,\quad 2\lambda_{2,5,6,7}\,,\quad \lambda_1+\lambda_4\,,\quad \lambda_1-\frac{1}{2}\lambda_4\,,\quad 2(\lambda_2+\lambda_3)\,,\quad \lambda^{\pm}_{023}\,,\quad \lambda^{\pm}_{078}\,,\quad \lambda^{\pm}_{146}\,, \tag{E.14}$$

with

$$\lambda^{\pm}_{078}\equiv\frac{1}{4}\left[(\lambda+2\lambda_7)\pm\sqrt{(\lambda-2\lambda_7)^2+32\lambda_8^2}\right]\,. \tag{E.15}$$

Finally, the sub-matrix for ($\frac{1}{\sqrt{2}}h^+h^+$, $\frac{1}{\sqrt{2}}\delta^+\delta^+$, $h^+\delta^+$, $\delta^{++}h$, $\delta^{++}\xi$, $\delta^{++}s$, $\delta^{++}Z_1$, $\delta^{++}Z_2$, $\delta^{++}Z_3$) is

$$\mathcal{M}_6=\begin{pmatrix}
\frac{\lambda}{2} & 0 & 0 & 0 & 0 & \lambda_8 & 0 & 0 & i\lambda_8\\
0 & 2\lambda'_{23} & 0 & 0 & 0 & 0 & 0 & 0 & 0\\
0 & 0 & \lambda'_{14} & -\frac{\lambda_4}{2} & 0 & 0 & \frac{i\lambda_4}{2} & 0 & 0\\
0 & 0 & -\frac{\lambda_4}{2} & \lambda_1 & 0 & 0 & 0 & 0 & 0\\
0 & 0 & 0 & 0 & 2\lambda_2 & 0 & 0 & 0 & 0\\
\lambda_8 & 0 & 0 & 0 & 0 & \lambda_7 & 0 & 0 & 0\\
0 & 0 & -\frac{i\lambda_4}{2} & 0 & 0 & 0 & \lambda_1 & 0 & 0\\
0 & 0 & 0 & 0 & 0 & 0 & 0 & 2\lambda_2 & 0\\
-i\lambda_8 & 0 & 0 & 0 & 0 & 0 & 0 & 0 & \lambda_7
\end{pmatrix}\,, \tag{E.16}$$

and the eigenvalues are

$$\lambda_{1,7}\,,\quad 2\lambda_2\,,\quad 2\lambda_2+\lambda_3\,,\quad \lambda_1+\lambda_4\,,\quad \lambda_1-\frac{1}{2}\lambda_4\,,\quad \lambda^{\pm}_{078}\,. \tag{E.17}$$

To implement the unitarity bounds, we can set all the eigenvalues in Eqs. ( E.5), ( E.8), ( E.12), ( E.14) and ( E.17) to be smaller than $8\pi$. As a comparison to the perturbativity bounds, we set the quartic couplings to be the benchmark values,

$$\lambda_1=0.1\,,\quad \lambda_4=-1\,,\quad \lambda_{2,3,5,6,7}=0\,, \tag{E.18}$$

and check the unitarity bounds on $\lambda_8$. It turns out for this specific benchmark scenario, only the following bounds are relevant to $\lambda_8$:

$$\left|\lambda^{\pm}_{146}\right|\leq 8\pi\,,\quad \left|\lambda^{\pm}_{078}\right|\leq 8\pi\,. \tag{E.19}$$

Among the four constraints, the most stringent one is from $\lambda^{-}_{146}$, which leads to

$$\lambda_8<10.0\,, \tag{E.20}$$

which is much weaker than the perturbativity bound discussed in Section 4.1.3.

## Bibliography


[1] Off-shell Higgs boson couplings measurement using $H \to ZZ \to 4l$ events at High Luminosity LHC. 2015.

[2] Sensitivity projections for Higgs boson properties measurements at the HL-LHC. 11 2018.

[3] P. A. Zyla et al. Review of Particle Physics. PTEP, 2020(8):083C01, 2020.

[4] Y. Amhis et al. Averages of $b$-hadron, $c$-hadron, and $\tau$-lepton properties as of summer 2016. Eur. Phys. J. C, 77(12):895, 2017.

[5] D. Hanneke, S. Fogwell, and G. Gabrielse. New Measurement of the Electron Magnetic Moment and the Fine Structure Constant. Phys. Rev. Lett., 100:120801, 2008.

[6] G. W. Bennett et al. Final Report of the Muon E821 Anomalous Magnetic Moment Measurement at BNL. Phys. Rev. D, 73:072003, 2006.

[7] B. Abi et al. Measurement of the Positive Muon Anomalous Magnetic Moment to 0.46 ppm. Phys. Rev. Lett., 126(14):141801, 2021.

[8] L. Willmann et al. New bounds from searching for muonium to anti-muonium conversion. Phys. Rev. Lett., 82:49–52, 1999.

[9] J. Abdallah et al. Measurement and interpretation of fermion-pair production at LEP energies above the Z resonance. Eur. Phys. J. C, 45:589–632, 2006.

[10] Georges Aad et al. Search for doubly and singly charged Higgs bosons decaying into vector bosons in multi-lepton final states with the ATLAS detector using proton-proton collisions at $\sqrt{s} = 13$ TeV. 1 2021.

[11] Morad Aaboud et al. Search for doubly charged Higgs boson production in multi-lepton final states with the ATLAS detector using proton–proton collisions at $\sqrt{s} =$ 13 TeV. Eur. Phys. J. C, 78(3):199, 2018.

[12] David Curtin. Mixing It Up With MT2: Unbiased Mass Measurements at Hadron Colliders. Phys. Rev. D, 85:075004, 2012.

[13] Georges Aad et al. Observation of a new particle in the search for the Standard Model Higgs boson with the ATLAS detector at the LHC. Phys. Lett. B, 716:1–29, 2012.

[14] Serguei Chatrchyan et al. Observation of a New Boson at a Mass of 125 GeV with the CMS Experiment at the LHC. Phys. Lett. B, 716:30–61, 2012.

[15] Peter W. Higgs. Broken symmetries, massless particles and gauge fields. Phys. Lett., 12:132–133, 1964.

[16] Peter W. Higgs. Broken Symmetries and the Masses of Gauge Bosons. Phys. Rev. Lett., 13:508–509, 1964.

[17] F. Englert and R. Brout. Broken Symmetry and the Mass of Gauge Vector Mesons. Phys. Rev. Lett., 13:321–323, 1964.

[18] G. Arnison et al. Experimental Observation of Isolated Large Transverse Energy Electrons with Associated Missing Energy at $\sqrt{s} = 540$ GeV. Phys. Lett. B, 122:103–116, 1983.

[19] M. Banner et al. Observation of Single Isolated Electrons of High Transverse Momentum in Events with Missing Transverse Energy at the CERN anti-p p Collider. Phys. Lett. B, 122:476–485, 1983.

[20] G. Arnison et al. Experimental Observation of Lepton Pairs of Invariant Mass Around 95-GeV/c**2 at the CERN SPS Collider. Phys. Lett. B, 126:398–410, 1983.

[21] P. Bagnaia et al. Evidence for $Z^0 \to e^+e^-$ at the CERN $\bar{p}p$ Collider. Phys. Lett. B, 129:130–140, 1983.

[22] Y. Fukuda et al. Evidence for oscillation of atmospheric neutrinos. Phys. Rev. Lett., 81:1562–1567, 1998.

[23] Q. R. Ahmad et al. Measurement of the rate of $\nu_e + d \to p + p + e^-$ interactions produced by $^8$B solar neutrinos at the Sudbury Neutrino Observatory. Phys. Rev. Lett., 87:071301, 2001.

[24] Adam G. Riess et al. A 2.4% Determination of the Local Value of the Hubble Constant. Astrophys. J., 826(1):56, 2016.

[25] Tom Shanks, Lucy Hogarth, and Nigel Metcalfe. Gaia Cepheid parallaxes and 'Local Hole' relieve $H_0$ tension. Mon. Not. Roy. Astron. Soc., 484(1):L64–L68, 2019.

[26] Adam G. Riess, Stefano Casertano, D'Arcy Kenworthy, Dan Scolnic, and Lucas Macri. Seven Problems with the Claims Related to the Hubble Tension in arXiv:1810.02595. 10 2018.

[27] N. Aghanim et al. Planck 2018 results. VI. Cosmological parameters. Astron. Astrophys., 641:A6, 2020. [Erratum: Astron.Astrophys. 652, C4 (2021)].

[28] Adam G. Riess, Stefano Casertano, Wenlong Yuan, Lucas M. Macri, and Dan Scolnic. Large Magellanic Cloud Cepheid Standards Provide a 1% Foundation for the Determination of the Hubble Constant and Stronger Evidence for Physics beyond ΛCDM. Astrophys. J., 876(1):85, 2019.

[29] Peter W. Higgs. Broken symmetries and the masses of gauge bosons. Phys. Rev. Lett., 13:508–509, Oct 1964.

[30] F. Englert and R. Brout. Broken symmetry and the mass of gauge vector mesons. Phys. Rev. Lett., 13:321–323, Aug 1964.

[31] G. Aad, T. Abajyan, B. Abbott, J. Abdallah, S. Abdel Khalek, A.A. Abdelalim, O. Abdinov, R. Aben, B. Abi, M. Abolins, and et al. Observation of a new particle in the search for the standard model higgs boson with the atlas detector at the lhc. Physics Letters B, 716(1):1–29, Sep 2012.

[32] S. Chatrchyan, V. Khachatryan, A.M. Sirunyan, A. Tumasyan, W. Adam, E. Aguilo, T. Bergauer, M. Dragicevic, J. Erö, C. Fabjan, and et al. Observation of a new boson at a mass of 125 gev with the cms experiment at the lhc. Physics Letters B, 716(1):30–61, Sep 2012.

[33] Nikolas Kauer and Giampiero Passarino. Inadequacy of zero-width approximation for a light Higgs boson signal. JHEP, 08:116, 2012.

[34] Fabrizio Caola and Kirill Melnikov. Constraining the Higgs boson width with ZZ production at the LHC. Phys. Rev., D88:054024, 2013.

[35] John M. Campbell, R. Keith Ellis, and Ciaran Williams. Bounding the Higgs width at the LHC using full analytic results for $gg- > e^-e^+\mu^-\mu^+$. JHEP, 04:060, 2014.

[36] Morad Aaboud et al. Constraints on off-shell Higgs boson production and the Higgs boson total width in $ZZ \to 4\ell$ and $ZZ \to 2\ell 2\nu$ final states with the ATLAS detector. Phys. Lett. B, 786:223–244, 2018.

[37] Albert M Sirunyan et al. Measurements of the Higgs boson width and anomalous $HVV$ couplings from on-shell and off-shell production in the four-lepton final state. Phys. Rev. D, 99(11):112003, 2019.

[38] James S. Gainer, Joseph Lykken, Konstantin T. Matchev, Stephen Mrenna, and Myeonghun Park. Beyond Geolocating: Constraining Higher Dimensional Operators in $H \to 4\ell$ with Off-Shell Production and More. Phys. Rev. D, 91(3):035011, 2015.

[39] Giacomo Cacciapaglia, Aldo Deandrea, Guillaume Drieu La Rochelle, and Jean-Baptiste Flament. Higgs couplings: disentangling New Physics with off-shell measurements. Phys. Rev. Lett., 113(20):201802, 2014.

[40] Aleksandr Azatov, Christophe Grojean, Ayan Paul, and Ennio Salvioni. Taming the off-shell Higgs boson. Zh. Eksp. Teor. Fiz., 147:410–425, 2015.

[41] Christoph Englert and Michael Spannowsky. Limitations and Opportunities of Off-Shell Coupling Measurements. Phys. Rev. D, 90:053003, 2014.

[42] Malte Buschmann, Dorival Goncalves, Silvan Kuttimalai, Marek Schonherr, Frank Krauss, and Tilman Plehn. Mass Effects in the Higgs-Gluon Coupling: Boosted vs Off-Shell Production. JHEP, 02:038, 2015.

[43] Tyler Corbett, Oscar J. P. Eboli, Dorival Goncalves, J. Gonzalez-Fraile, Tilman Plehn, and Michael Rauch. The Higgs Legacy of the LHC Run I. JHEP, 08:156, 2015.

[44] Dorival Goncalves, Tao Han, and Satyanarayan Mukhopadhyay. Off-Shell Higgs Probe of Naturalness. Phys. Rev. Lett., 120(11):111801, 2018. [Erratum: Phys.Rev.Lett. 121, 079902 (2018)].

[45] Dorival Gonçalves, Tao Han, and Satyanarayan Mukhopadhyay. Higgs Couplings at High Scales. Phys. Rev., D98(1):015023, 2018.

[46] Christoph Englert, Yotam Soreq, and Michael Spannowsky. Off-Shell Higgs Coupling Measurements in BSM scenarios. JHEP, 05:145, 2015.

[47] J. Alwall, R. Frederix, S. Frixione, V. Hirschi, F. Maltoni, O. Mattelaer, H. S. Shao, T. Stelzer, P. Torrielli, and M. Zaro. The automated computation of tree-level and next-to-leading order differential cross sections, and their matching to parton shower simulations. JHEP, 07:079, 2014.

[48] Valentin Hirschi and Olivier Mattelaer. Automated event generation for loop-induced processes. JHEP, 10:146, 2015.

[49] Stefano Frixione and Bryan R. Webber. Matching NLO QCD computations and parton shower simulations. JHEP, 06:029, 2002.

[50] Marco Bonvini, Fabrizio Caola, Stefano Forte, Kirill Melnikov, and Giovanni Ridolfi. Signal-background interference effects for $gg \to H \to W^+W^-$ beyond leading order. Phys. Rev., D88(3):034032, 2013.

[51] Pierre Artoisenet, Rikkert Frederix, Olivier Mattelaer, and Robbert Rietkerk. Automatic spin-entangled decays of heavy resonances in Monte Carlo simulations. JHEP, 03:015, 2013.

[52] Richard D. Ball, Valerio Bertone, Stefano Carrazza, Luigi Del Debbio, Stefano Forte, Alberto Guffanti, Nathan P. Hartland, and Juan Rojo. Parton distributions with QED corrections. Nucl. Phys., B877:290–320, 2013.

[53] Torbjörn Sjöstrand, Stefan Ask, Jesper R. Christiansen, Richard Corke, Nishita Desai, Philip Ilten, Stephen Mrenna, Stefan Prestel, Christine O. Rasmussen, and Peter Z. Skands. An Introduction to PYTHIA 8.2. Comput. Phys. Commun., 191:159–177, 2015.

[54] S. Ovyn, X. Rouby, and V. Lemaitre. DELPHES, a framework for fast simulation of a generic collider experiment. 2009.

[55] Andreas Hoecker, Peter Speckmayer, Joerg Stelzer, Jan Therhaag, Eckhard von Toerne, and Helge Voss. TMVA: Toolkit for Multivariate Data Analysis. PoS, ACAT:040, 2007.

[56] Dorival Goncalves and Junya Nakamura. Role of the $Z$ polarization in the $H \to b\bar{b}$ measurement. Phys. Rev., D98(9):093005, 2018.

[57] Dorival Goncalves and Junya Nakamura. Boosting the $H \to$ invisibles searches with $Z$ boson polarization. Phys. Rev., D99(5):055021, 2019.

[58] John C. Collins and Davison E. Soper. Angular Distribution of Dileptons in High-Energy Hadron Collisions. Phys. Rev., D16:2219, 1977.

[59] Dorival Goncalves, Tilman Plehn, and Jennifer M. Thompson. Weak boson fusion at 100 TeV. Phys. Rev., D95(9):095011, 2017.

[60] Thomas Appelquist and J. Carazzone. Infrared Singularities and Massive Fields. Phys. Rev. D, 11:2856, 1975.

[61] W. Buchmuller and D. Wyler. Effective Lagrangian Analysis of New Interactions and Flavor Conservation. Nucl. Phys. B, 268:621–653, 1986.

[62] B. Grzadkowski, M. Iskrzynski, M. Misiak, and J. Rosiek. Dimension-Six Terms in the Standard Model Lagrangian. JHEP, 10:085, 2010.

[63] Mikhail A. Shifman, A.I. Vainshtein, M.B. Voloshin, and Valentin I. Zakharov. Low-Energy Theorems for Higgs Boson Couplings to Photons. Sov. J. Nucl. Phys., 30:711–716, 1979.

[64] Bernd A. Kniehl and Michael Spira. Low-energy theorems in Higgs physics. Z. Phys. C, 69:77–88, 1995.

[65] U. Baur and E.W.Nigel Glover. Higgs Boson Production at Large Transverse Momentum in Hadronic Collisions. Nucl. Phys. B, 339:38–66, 1990.

[66] Robert V. Harlander and Tobias Neumann. Probing the nature of the Higgs-gluon coupling. Phys. Rev. D, 88:074015, 2013.

[67] Andrea Banfi, Adam Martin, and Veronica Sanz. Probing top-partners in Higgs+jets. JHEP, 08:053, 2014.

[68] Aleksandr Azatov and Ayan Paul. Probing Higgs couplings with high $p_T$ Higgs production. JHEP, 01:014, 2014.

[69] Christophe Grojean, Ennio Salvioni, Matthias Schlaffer, and Andreas Weiler. Very boosted Higgs in gluon fusion. JHEP, 05:022, 2014.

[70] Malte Buschmann, Christoph Englert, Dorival Goncalves, Tilman Plehn, and Michael Spannowsky. Resolving the Higgs-Gluon Coupling with Jets. Phys. Rev. D, 90(1):013010, 2014.

[71] Aleksandr Azatov, Christophe Grojean, Ayan Paul, and Ennio Salvioni. Resolving gluon fusion loops at current and future hadron colliders. JHEP, 09:123, 2016.

[72] Michelangelo L. Mangano, Tilman Plehn, Peter Reimitz, Torben Schell, and Hua-Sheng Shao. Measuring the Top Yukawa Coupling at 100 TeV. J. Phys. G, 43(3):035001, 2016.

[73] E.W.Nigel Glover and J.J. van der Bij. Z BOSON PAIR PRODUCTION VIA GLUON FUSION. Nucl. Phys. B, 321:561–590, 1989.

[74] Adam Alloul, Neil D. Christensen, Céline Degrande, Claude Duhr, and Benjamin Fuks. FeynRules 2.0 - A complete toolbox for tree-level phenomenology. Comput. Phys. Commun., 185:2250–2300, 2014.

[75] Celine Degrande. Automatic evaluation of UV and R2 terms for beyond the Standard Model Lagrangians: a proof-of-principle. Comput. Phys. Commun., 197:239–262, 2015.

[76] Céline Degrande, Claude Duhr, Benjamin Fuks, David Grellscheid, Olivier Mattelaer, and Thomas Reiter. Ufo – the universal feynrules output. Computer Physics Communications, 183(6):1201–1214, Jun 2012.

[77] M. Cepeda et al. Report from Working Group 2: Higgs Physics at the HL-LHC and HE-LHC. CERN Yellow Rep. Monogr., 7:221–584, 2019.

[78] Alex Pomarol and Francesco Riva. The Composite Higgs and Light Resonance Connection. JHEP, 08:135, 2012.

[79] Giuliano Panico and Andrea Wulzer. The Discrete Composite Higgs Model. JHEP, 09:135, 2011.

[80] Giuliano Panico and Andrea Wulzer. The Composite Nambu-Goldstone Higgs. Lect. Notes Phys., 913:pp.1–316, 2016.

[81] Da Liu, Ian Low, and Carlos E. M. Wagner. Modification of Higgs Couplings in Minimal Composite Models. Phys. Rev., D96(3):035013, 2017.

[82] V. Punjabi, C. F. Perdrisat, M. K. Jones, E. J. Brash, and C. E. Carlson. The Structure of the Nucleon: Elastic Electromagnetic Form Factors. Eur. Phys. J., A51:79, 2015.

[83] Christopher T. Hill and Elizabeth H. Simmons. Strong Dynamics and Electroweak Symmetry Breaking. Phys. Rept., 381:235–402, 2003. [Erratum: Phys.Rept. 390, 553–554 (2004)].

[84] Dario Buttazzo, Giuseppe Degrassi, Pier Paolo Giardino, Gian F. Giudice, Filippo Sala, Alberto Salvio, and Alessandro Strumia. Investigating the near-criticality of the Higgs boson. JHEP, 12:089, 2013.

[85] Fedor Bezrukov and Mikhail Shaposhnikov. Why should we care about the top quark Yukawa coupling? J. Exp. Theor. Phys., 120:335–343, 2015.

[86] Marcela Carena, M. Olechowski, S. Pokorski, and C. E. M. Wagner. Radiative electroweak symmetry breaking and the infrared fixed point of the top quark mass. Nucl. Phys. B, 419:213–239, 1994.

[87] Oleksii Matsedonskyi, Giuliano Panico, and Andrea Wulzer. Light Top Partners for a Light Composite Higgs. JHEP, 01:164, 2013.

[88] Brando Bellazzini, Csaba Csáki, and Javi Serra. Composite Higgses. Eur. Phys. J. C, 74(5):2766, 2014.

[89] Georges Aad et al. Combined measurements of Higgs boson production and decay using up to 80 fb$^{-1}$ of proton-proton collision data at $\sqrt{s} = 13$ TeV collected with the ATLAS experiment. Phys. Rev. D, 101(1):012002, 2020.

[90] M. Aaboud et al. Observation of Higgs boson production in association with a top quark pair at the LHC with the ATLAS detector. Phys. Lett. B, 784:173–191, 2018.

[91] Albert M Sirunyan et al. Observation of $t\bar{t}H$ production. Phys. Rev. Lett., 120(23):231801, 2018.

[92] Dorival Gonçalves, Tao Han, Sze Ching Iris Leung, and Han Qin. Off-shell Higgs couplings in $H^* \to ZZ \to \ell\ell\nu\nu$. Phys. Lett. B, 817:136329, 2021.

[93] John Ellis, Maeve Madigan, Ken Mimasu, Veronica Sanz, and Tevong You. Top, Higgs, Diboson and Electroweak Fit to the Standard Model Effective Field Theory. 12 2020.

[94] Jacob J. Ethier, Fabio Maltoni, Luca Mantani, Emanuele R. Nocera, Juan Rojo, Emma Slade, Eleni Vryonidou, and Cen Zhang. Combined SMEFT interpretation of Higgs, diboson, and top quark data from the LHC. 4 2021.

[95] Ilaria Brivio, Sebastian Bruggisser, Fabio Maltoni, Rhea Moutafis, Tilman Plehn, Eleni Vryonidou, Susanne Westhoff, and C. Zhang. O new physics, where art thou? A global search in the top sector. JHEP, 02:131, 2020.

[96] Anke Biekötter, Dorival Gonçalves, Tilman Plehn, Michihisa Takeuchi, and Dirk Zerwas. The global Higgs picture at 27 TeV. SciPost Phys., 6(2):024, 2019.

[97] Fabio Maltoni, Eleni Vryonidou, and Cen Zhang. Higgs production in association with a top-antitop pair in the Standard Model Effective Field Theory at NLO in QCD. JHEP, 10:123, 2016.

[98] A combination of measurements of Higgs boson production and decay using up to 139 fb$^{-1}$ of proton–proton collision data at $\sqrt{s} = 13$ TeV collected with the ATLAS experiment. Technical report, CERN, Geneva, Aug 2020.

[99] Albert M Sirunyan et al. Measurement of the top quark polarization and $t\bar{t}$ spin correlations using dilepton final states in proton-proton collisions at $\sqrt{s} = 13$ TeV. Phys. Rev. D, 100(7):072002, 2019.

[100] Avik Banerjee, Sayan Dasgupta, and Tirtha Sankar Ray. Chasing the Higgs shape at HL-LHC. 5 2021.

[101] Céline Degrande, Gauthier Durieux, Fabio Maltoni, Ken Mimasu, Eleni Vryonidou, and Cen Zhang. Automated one-loop computations in the SMEFT. 8 2020.

[102] Reza Goldouzian, Jeong Han Kim, Kevin Lannon, Adam Martin, Kelci Mohrman, and Andrew Wightman. Matching in $pp \to t\bar{t}W/Z/h+$ jet SMEFT studies. 12 2020.

[103] Peter Skands, Stefano Carrazza, and Juan Rojo. Tuning PYTHIA 8.1: the Monash 2013 Tune. Eur. Phys. J. C, 74(8):3024, 2014.

[104] L. A. Harland-Lang, A. D. Martin, P. Motylinski, and R. S. Thorne. Parton distributions in the LHC era: MMHT 2014 PDFs. Eur. Phys. J. C, 75(5):204, 2015.

[105] Matthew R. Buckley and Dorival Goncalves. Boosting the Direct CP Measurement of the Higgs-Top Coupling. Phys. Rev. Lett., 116(9):091801, 2016.

[106] Matteo Cacciari, Gavin P. Salam, and Gregory Soyez. FastJet User Manual. Eur. Phys. J. C, 72:1896, 2012.

[107] Jonathan M. Butterworth, Adam R. Davison, Mathieu Rubin, and Gavin P. Salam. Jet substructure as a new Higgs search channel at the LHC. Phys. Rev. Lett., 100:242001, 2008.

[108] Tilman Plehn, Gavin P. Salam, and Michael Spannowsky. Fat Jets for a Light Higgs. Phys. Rev. Lett., 104:111801, 2010.

[109] Technical Design Report for the ATLAS Inner Tracker Pixel Detector. Technical Report CERN-LHCC-2017-021. ATLAS-TDR-030, CERN, Geneva, Sep 2017.

[110] Using associated top quark production to probe for new physics within the framework of effective field theory. Technical report, CERN, Geneva, 2020.

[111] Samoil M. Bilenky. Neutrinos: Majorana or Dirac? Universe, 6(9):134, 2020.

[112] P. S. Bhupal Dev et al. Neutrino Non-Standard Interactions: A Status Report. SciPost Phys. Proc., 2:001, 2019.

[113] Massimiliano Lattanzi, Roberto A. Lineros, and Marco Taoso. Connecting neutrino physics with dark matter. New J. Phys., 16(12):125012, 2014.

[114] Ernest Ma. Verifiable radiative seesaw mechanism of neutrino mass and dark matter. Phys. Rev. D, 73:077301, 2006.

[115] Jackson D. Clarke and Raymond R. Volkas. Technically natural nonsupersymmetric model of neutrino masses, baryogenesis, the strong CP problem, and dark matter. Phys. Rev. D, 93(3):035001, 2016.

[116] C. Hagedorn, R. N. Mohapatra, E. Molinaro, C. C. Nishi, and S. T. Petcov. CP Violation in the Lepton Sector and Implications for Leptogenesis. Int. J. Mod. Phys. A, 33(05n06):1842006, 2018.

[117] Jeffrey M. Berryman, André de Gouvêa, Kevin J. Kelly, and Yue Zhang. Lepton-Number-Charged Scalars and Neutrino Beamstrahlung. Phys. Rev. D, 97(7):075030, 2018.

[118] André de Gouvêa, P. S. Bhupal Dev, Bhaskar Dutta, Tathagata Ghosh, Tao Han, and Yongchao Zhang. Leptonic Scalars at the LHC. JHEP, 07:142, 2020.

[119] Christina D. Kreisch, Francis-Yan Cyr-Racine, and Olivier Doré. Neutrino puzzle: Anomalies, interactions, and cosmological tensions. Phys. Rev. D, 101(12):123505, 2020.

[120] Nikita Blinov, Kevin James Kelly, Gordan Z Krnjaic, and Samuel D McDermott. Constraining the Self-Interacting Neutrino Interpretation of the Hubble Tension. Phys. Rev. Lett., 123(19):191102, 2019.

[121] André De Gouvêa, Manibrata Sen, Walter Tangarife, and Yue Zhang. Dodelson-Widrow Mechanism in the Presence of Self-Interacting Neutrinos. Phys. Rev. Lett., 124(8):081802, 2020.

[122] Kun-Feng Lyu, Emmanuel Stamou, and Lian-Tao Wang. Self-interacting neutrinos: Solution to Hubble tension versus experimental constraints. Phys. Rev. D, 103(1):015004, 2021.

[123] Kevin J. Kelly, Manibrata Sen, and Yue Zhang. Intimate Relationship between Sterile Neutrino Dark Matter and $\Delta$Neff. Phys. Rev. Lett., 127(4):041101, 2021.

[124] Anirban Das and Subhajit Ghosh. Flavor-specific interaction favors strong neutrino self-coupling in the early universe. JCAP, 07:038, 2021.

[125] A. Abada et al. FCC-hh: The Hadron Collider: Future Circular Collider Conceptual Design Report Volume 3. Eur. Phys. J. ST, 228(4):755–1107, 2019.

[126] Jingyu Tang et al. Concept for a Future Super Proton-Proton Collider. 7 2015.

[127] W. Konetschny and W. Kummer. Nonconservation of Total Lepton Number with Scalar Bosons. Phys. Lett. B, 70:433–435, 1977.

[128] M. Magg and C. Wetterich. Neutrino Mass Problem and Gauge Hierarchy. Phys. Lett. B, 94:61–64, 1980.

[129] J. Schechter and J. W. F. Valle. Neutrino Masses in SU(2) x U(1) Theories. Phys. Rev. D, 22:2227, 1980.

[130] T. P. Cheng and Ling-Fong Li. Neutrino Masses, Mixings and Oscillations in SU(2) x U(1) Models of Electroweak Interactions. Phys. Rev. D, 22:2860, 1980.

[131] Rabindra N. Mohapatra and Goran Senjanovic. Neutrino Masses and Mixings in Gauge Models with Spontaneous Parity Violation. Phys. Rev. D, 23:165, 1981.

[132] George Lazarides, Q. Shafi, and C. Wetterich. Proton Lifetime and Fermion Masses in an SO(10) Model. Nucl. Phys. B, 181:287–300, 1981.

[133] Neil D. Barrie, Chengcheng Han, and Hitoshi Murayama. Affleck-Dine Leptogenesis from Higgs Inflation. 6 2021.

[134] Maxim Pospelov, Adam Ritz, and Mikhail B. Voloshin. Secluded WIMP Dark Matter. Phys. Lett. B, 662:53–61, 2008.

[135] Kevin J. Kelly and Yue Zhang. Mononeutrino at DUNE: New Signals from Neutrinophilic Thermal Dark Matter. Phys. Rev. D, 99(5):055034, 2019.

[136] Yong Du, Fei Huang, Hao-Lin Li, and Jiang-Hao Yu. Freeze-in Dark Matter from Secret Neutrino Interactions. JHEP, 12:207, 2020.

[137] Byron P. Roe, Hai-Jun Yang, Ji Zhu, Yong Liu, Ion Stancu, and Gordon McGregor. Boosted decision trees, an alternative to artificial neural networks. Nucl. Instrum. Meth. A, 543(2-3):577–584, 2005.

[138] M. Aker et al. Improved Upper Limit on the Neutrino Mass from a Direct Kinematic Method by KATRIN. Phys. Rev. Lett., 123(22):221802, 2019.

[139] Surajit Chakrabarti, Debajyoti Choudhury, Rohini M. Godbole, and Biswarup Mukhopadhyaya. Observing doubly charged Higgs bosons in photon-photon collisions. Phys. Lett. B, 434:347–353, 1998.

[140] Eung Jin Chun, Kang Young Lee, and Seong Chan Park. Testing Higgs triplet model and neutrino mass patterns. Phys. Lett. B, 566:142–151, 2003.

[141] A. G. Akeroyd and Mayumi Aoki. Single and pair production of doubly charged Higgs bosons at hadron colliders. Phys. Rev. D, 72:035011, 2005.

[142] Pavel Fileviez Perez, Tao Han, Gui-yu Huang, Tong Li, and Kai Wang. Neutrino Masses and the CERN LHC: Testing Type II Seesaw. Phys. Rev. D, 78:015018, 2008.

[143] F. del Aguila and J. A. Aguilar-Saavedra. Distinguishing seesaw models at LHC with multi-lepton signals. Nucl. Phys. B, 813:22–90, 2009.

[144] A. G. Akeroyd and Hiroaki Sugiyama. Production of doubly charged scalars from the decay of singly charged scalars in the Higgs Triplet Model. Phys. Rev. D, 84:035010, 2011.

[145] Alejandra Melfo, Miha Nemevsek, Fabrizio Nesti, Goran Senjanovic, and Yue Zhang. Type II Seesaw at LHC: The Roadmap. Phys. Rev. D, 85:055018, 2012.

[146] Mayumi Aoki, Shinya Kanemura, and Kei Yagyu. Testing the Higgs triplet model with the mass difference at the LHC. Phys. Rev. D, 85:055007, 2012.

[147] Cheng-Wei Chiang, Takaaki Nomura, and Koji Tsumura. Search for doubly charged Higgs bosons using the same-sign diboson mode at the LHC. Phys. Rev. D, 85:095023, 2012.

[148] Zhi-Long Han, Ran Ding, and Yi Liao. LHC Phenomenology of Type II Seesaw: Nondegenerate Case. Phys. Rev. D, 91:093006, 2015.

[149] K. S. Babu and Sudip Jana. Probing Doubly Charged Higgs Bosons at the LHC through Photon Initiated Processes. Phys. Rev. D, 95(5):055020, 2017.

[150] Dilip Kumar Ghosh, Nivedita Ghosh, Ipsita Saha, and Avirup Shaw. Revisiting the high-scale validity of the type II seesaw model with novel LHC signature. Phys. Rev. D, 97(11):115022, 2018.

[151] P. S. Bhupal Dev and Yongchao Zhang. Displaced vertex signatures of doubly charged scalars in the type-II seesaw and its left-right extensions. JHEP, 10:199, 2018.

[152] Yong Du, Aaron Dunbrack, Michael J. Ramsey-Musolf, and Jiang-Hao Yu. Type-II Seesaw Scalar Triplet Model at a 100 TeV *pp* Collider: Discovery and Higgs Portal Coupling Determination. JHEP, 01:101, 2019.

[153] Stefan Antusch, Oliver Fischer, A. Hammad, and Christiane Scherb. Low scale type II seesaw: Present constraints and prospects for displaced vertex searches. JHEP, 02:157, 2019.

[154] R. Primulando, J. Julio, and P. Uttayarat. Scalar phenomenology in type-II seesaw model. JHEP, 08:024, 2019.

[155] Tessio B. de Melo, Farinaldo S. Queiroz, and Yoxara Villamizar. Doubly Charged Scalar at the High-Luminosity and High-Energy LHC. Int. J. Mod. Phys. A, 34(27):1950157, 2019.

[156] Rojalin Padhan, Debottam Das, Manimala Mitra, and Aruna Kumar Nayak. Probing doubly and singly charged Higgs bosons at the $pp$ collider HE-LHC. Phys. Rev. D, 101(7):075050, 2020.

[157] Saiyad Ashanujjaman and Kirtiman Ghosh. Revisiting Type-II see-saw: Present Limits and Future Prospects at LHC. 8 2021.

[158] Michael E. Peskin and Tatsu Takeuchi. A New constraint on a strongly interacting Higgs sector. Phys. Rev. Lett., 65:964–967, 1990.

[159] Michael E. Peskin and Tatsu Takeuchi. Estimation of oblique electroweak corrections. Phys. Rev. D, 46:381–409, 1992.

[160] Shinya Kanemura and Kei Yagyu. Radiative corrections to electroweak parameters in the Higgs triplet model and implication with the recent Higgs boson searches. Phys. Rev. D, 85:115009, 2012.

[161] Eung Jin Chun, Hyun Min Lee, and Pankaj Sharma. Vacuum Stability, Perturbativity, EWPD and Higgs-to-diphoton rate in Type II Seesaw Models. JHEP, 11:106, 2012.

[162] A search for doubly-charged Higgs boson production in three and four lepton final states at $\sqrt{s} = 13$ TeV. 2017.

[163] Morad Aaboud et al. Search for doubly charged scalar bosons decaying into same-sign $W$ boson pairs with the ATLAS detector. Eur. Phys. J. C, 79(1):58, 2019.

[164] Manfred Lindner, Moritz Platscher, and Farinaldo S. Queiroz. A Call for New Physics : The Muon Anomalous Magnetic Moment and Lepton Flavor Violation. Phys. Rept., 731:1–82, 2018.

[165] T. Aoyama et al. The anomalous magnetic moment of the muon in the Standard Model. Phys. Rept., 887:1–166, 2020.

[166] P. S. Bhupal Dev, Rabindra N. Mohapatra, and Yongchao Zhang. Lepton Flavor Violation Induced by a Neutral Scalar at Future Lepton Colliders. Phys. Rev. Lett., 120(22):221804, 2018.

[167] P. S. Bhupal Dev, Rabindra N. Mohapatra, and Yongchao Zhang. Probing TeV scale origin of neutrino mass at future lepton colliders via neutral and doubly-charged scalars. Phys. Rev. D, 98(7):075028, 2018.

[168] Tong Li and Michael A. Schmidt. Sensitivity of future lepton colliders to the search for charged lepton flavor violation. Phys. Rev. D, 99(5):055038, 2019.

[169] Jared A. Evans, Philip Tanedo, and Mohammadreza Zakeri. Exotic Lepton-Flavor Violating Higgs Decays. JHEP, 01:028, 2020.

[170] Syuhei Iguro, Yuji Omura, and Michihisa Takeuchi. Probing $\mu\tau$ flavor-violating solutions for the muon $g-2$ anomaly at Belle II. JHEP, 09:144, 2020.

[171] Tong Li, Michael A. Schmidt, Chang-Yuan Yao, and Man Yuan. Charged lepton flavor violation in light of the muon magnetic moment anomaly and colliders. 4 2021.

[172] Wei-Shu Hou and Girish Kumar. Charged lepton flavor violation in light of Muon $g-2$. 7 2021.

[173] Rodolfo Capdevilla, David Curtin, Yonatan Kahn, and Gordan Krnjaic. Discovering the physics of $(g-2)_\mu$ at future muon colliders. Phys. Rev. D, 103(7):075028, 2021.

[174] Dario Buttazzo and Paride Paradisi. Probing the muon g-2 anomaly at a Muon Collider. 12 2020.

[175] Wen Yin and Masahiro Yamaguchi. Muon $g-2$ at multi-TeV muon collider. 12 2020.

[176] Rodolfo Capdevilla, David Curtin, Yonatan Kahn, and Gordan Krnjaic. A No-Lose Theorem for Discovering the New Physics of $(g-2)_\mu$ at Muon Colliders. 1 2021.

[177] Gholamhossein Haghighat and Mojtaba Mohammadi Najafabadi. Search for lepton-flavor-violating ALPs at a future muon collider and utilization of polarization-induced effects. 6 2021.

[178] M. A. Perez and M. A. Soriano. Flavor changing decays of the Z and Z-prime gauge bosons in left-right symmetric models. Phys. Rev. D, 46:284–289, 1992.

[179] Miha Nemevšek, Fabrizio Nesti, and Juan Carlos Vasquez. Majorana Higgses at colliders. JHEP, 04:114, 2017.

[180] Hideo Fusaoka and Yoshio Koide. Updated estimate of running quark masses. Phys. Rev. D, 57:3986–4001, 1998.

[181] Zhi-zhong Xing, He Zhang, and Shun Zhou. Updated Values of Running Quark and Lepton Masses. Phys. Rev. D, 77:113016, 2008.

[182] Zhi-zhong Xing, He Zhang, and Shun Zhou. Impacts of the Higgs mass on vacuum stability, running fermion masses and two-body Higgs decays. Phys. Rev. D, 86:013013, 2012.

[183] Stefan Antusch and Vinzenz Maurer. Running quark and lepton parameters at various scales. JHEP, 11:115, 2013.

[184] Guo-yuan Huang and Shun Zhou. Precise Values of Running Quark and Lepton Masses in the Standard Model. Phys. Rev. D, 103(1):016010, 2021.

[185] Nima Arkani-Hamed, Tao Han, Michelangelo Mangano, and Lian-Tao Wang. Physics opportunities of a 100 TeV proton–proton collider. Phys. Rept., 652:1–49, 2016.

[186] Margarete Muhlleitner and Michael Spira. A Note on doubly charged Higgs pair production at hadron colliders. Phys. Rev. D, 68:117701, 2003.

[187] Torbjorn Sjostrand, Stephen Mrenna, and Peter Z. Skands. A Brief Introduction to PYTHIA 8.1. Comput. Phys. Commun., 178:852–867, 2008.

[188] Matteo Cacciari, Gavin P. Salam, and Gregory Soyez. The anti-$k_t$ jet clustering algorithm. JHEP, 04:063, 2008.

[189] J. de Favereau, C. Delaere, P. Demin, A. Giammanco, V. Lemaître, A. Mertens, and M. Selvaggi. DELPHES 3, A modular framework for fast simulation of a generic collider experiment. JHEP, 02:057, 2014.

[190] Vernon D. Barger, Tao Han, and J. Ohnemus. HEAVY LEPTONS AT HADRON SUPERCOLLIDERS. Phys. Rev. D, 37:1174, 1988.

[191] Search for squarks and gluinos in final states with an isolated lepton, jets, and missing transverse momentum at $\sqrt{s} = 13$ TeV with the ATLAS detector. 8 2020.

[192] Search for new phenomena in final states with large jet multiplicities and missing transverse momentum using $\sqrt{s} = 13$ TeV proton-proton collisions recorded by ATLAS in Run 2 of the LHC. 2 2020.

[193] Tianqi Chen and Carlos Guestrin. XGBoost: A Scalable Tree Boosting System. 3 2016.

[194] G. Abbiendi et al. Search for doubly charged Higgs bosons with the OPAL detector at LEP. Phys. Lett. B, 526:221–232, 2002.

[195] J. Abdallah et al. Search for doubly charged Higgs bosons at LEP-2. Phys. Lett. B, 552:127–137, 2003.

[196] P. Achard et al. Search for doubly charged Higgs bosons at LEP. Phys. Lett. B, 576:18–28, 2003.

[197] D. Acosta et al. Search for doubly-charged Higgs bosons decaying to dileptons in $p\bar{p}$ collisions at $\sqrt{s} = 1.96$ TeV. Phys. Rev. Lett., 93:221802, 2004.

[198] T. Aaltonen et al. Search for Doubly Charged Higgs Bosons with Lepton-Flavor-Violating Decays involving Tau Leptons. Phys. Rev. Lett., 101:121801, 2008.

[199] V. M. Abazov et al. Search for pair production of doubly-charged Higgs bosons in the $H^{++}H^{--} \to \mu^+\mu^+\mu^-\mu^-$ final state at D0. Phys. Rev. Lett., 101:071803, 2008.

[200] Victor Mukhamedovich Abazov et al. Search for doubly-charged Higgs boson pair production in $p\bar{p}$ collisions at $\sqrt{s} = 1.96$ TeV. Phys. Rev. Lett., 108:021801, 2012.

[201] Search for Doubly Charged Higgs Boson Production in Like-sign Muon Pairs in pp Collisions at $\sqrt{}$s=7 TeV. 9 2011.

[202] Inclusive search for doubly charged higgs in leptonic final states at sqrt s=7 TeV. 2011.

[203] Georges Aad et al. Search for anomalous production of prompt same-sign lepton pairs and pair-produced doubly charged Higgs bosons with $\sqrt{s} = 8$ TeV $pp$ collisions using the ATLAS detector. JHEP, 03:041, 2015.

[204] Search for a doubly-charged Higgs boson with $\sqrt{s} = 8$ TeV $pp$ collisions at the CMS experiment. 2016.

[205] Ben Gripaios. Transverse observables and mass determination at hadron colliders. JHEP, 02:053, 2008.

[206] Alan J. Barr, Ben Gripaios, and Christopher G. Lester. Weighing Wimps with Kinks at Colliders: Invisible Particle Mass Measurements from Endpoints. JHEP, 02:014, 2008.

[207] Johann Brehmer, Felix Kling, Irina Espejo, and Kyle Cranmer. MadMiner: Machine learning-based inference for particle physics. Comput. Softw. Big Sci., 4(1):3, 2020.

[208] Morad Aaboud et al. Search for the standard model Higgs boson produced in association with top quarks and decaying into a $b\bar{b}$ pair in $pp$ collisions at $\sqrt{s} = 13$ TeV with the ATLAS detector. Phys. Rev. D, 97(7):072016, 2018.

[209] Tomáš Ježo, Jonas M. Lindert, Niccolo Moretti, and Stefano Pozzorini. New NLOPS predictions for $t\bar{t} + b$ -jet production at the LHC. Eur. Phys. J. C, 78(6):502, 2018.

[210] Ansgar Denner, Jean-Nicolas Lang, and Mathieu Pellen. Full NLO QCD corrections to off-shell tt¯bb¯ production. Phys. Rev. D, 104(5):056018, 2021.

[211] Giuseppe Bevilacqua, Huan-Yu Bi, Heribertus Bayu Hartanto, Manfred Kraus, Michele Lupattelli, and Malgorzata Worek. $t\bar{t}b\bar{b}$ at the LHC: on the size of corrections and b-jet definitions. JHEP, 08:008, 2021.

[212] F. Lyonnet, I. Schienbein, F. Staub, and A. Wingerter. PyR@TE: Renormalization Group Equations for General Gauge Theories. Comput. Phys. Commun., 185:1130–1152, 2014.

[213] Lohan Sartore and Ingo Schienbein. PyR@TE 3. Comput. Phys. Commun., 261:107819, 2021.

[214] H. Arason, D. J. Castano, B. Keszthelyi, S. Mikaelian, E. J. Piard, Pierre Ramond, and B. D. Wright. Renormalization group study of the standard model and its extensions. 1. The Standard model. Phys. Rev. D, 46:3945–3965, 1992.

[215] A. Arhrib, R. Benbrik, M. Chabab, G. Moultaka, M. C. Peyranere, L. Rahili, and J. Ramadan. The Higgs Potential in the Type II Seesaw Model. Phys. Rev., D84:095005, 2011.